UNIVERSITÀ DEGLI STUDI DI MILANO

UNIVERSITÀ DEGLI STUDI DI MILANO

Dipartimento di Fisica

Corso di Dottorato in Fisica, Astrofisica e Fisica Applicata

Ciclo XXXI

Design, simulation and performances study of the FOOT experiment

Settore Scientifico Disciplinare FIS/04

Coordinatore: Professor Matteo PARIS

Supervisore: Dottor Giuseppe BATTISTONI

Tesi di Dottorato di:

Serena Marta VALLE

Anno Accademico 2018/2019

Commission of the final examination:

External Referee:
Alessandra Fantoni, Concettina Sfienti

External Member:
Giuseppina Bisogni, Chiara Guazzoni

Internal Member:
Angela Bracco

Final examination:

Date 18/01/2019

Università degli Studi di Milano, Dipartimento di Fisica, Milano, Italy

Contents

List of Acronyms

ALM	Augmented Lagrangian Method
BGO	bismuth germanate
BME	*Boltzmann-Master Equation*
BMN	Beam Monitor
BP	*Bragg peak*
CAL	Calorimeter
CERN	European Organization for Nuclear Research
CNAO	Centro Nazionale di Adroterapia Oncologica
CSDA	*Continuous-Slowing-Down Approximation*
CT	Computed Tomography
DAQ	Data Acquisition
DNA	*deoxyribonucleic acid*
DPM	*Dual Parton Model*
DPMJET-III	*Dual Parton Model and JETs*
DSB	Double Strand Breaks
DSSD	*Double-Sided Strip Detector*
ECC	Emulsion Cloud Chamber
FIRST	Fragmentation of Ions Relevant for Space and Therapy
FLUKA	FLUktuierende KAskade
FOOT	FragmentatiOn Of Target
FPC	Flexible Printed Cable
GCR	*Galactic Cosmic Rays*
GINC	*Generalized Intra-Nuclear cascade*
GPU	*Graphics Processing Unit*
GSI	Gesellschaft für Schwerionenforschung
HIT	Heidelberg Ion-Beam Therapy Center
ID	identification
IMRT	*Intensity Modulated Radiation Therapy*
INC	*Intra-Nuclear Cascade*
INCL	*Liège Intra-Nuclear Cascade*
INFN	Italian National Institute for Nuclear Physics
ISS	International Space Station
ITR	Inner Tracker
LEM	*Local Effect Model*
LET	*Linear Energy Transfer*
LINAC	*linear accelerator*
LNS	Laboratori Nazionali del Sud
M28	MIMOSA28
MAPS	Monolithic Active Pixel Sensors
MC	Monte Carlo
MCS	*Multiple Coulomb Scattering*
MKM	*Microdosimetric Kinetic Model*
MSD	Microstrip Silicon Detector
NTCP	*Normal Tissue Complication Probability*

OAR	*Organs at Risk*
OER	*Oxygen Enhancement Ratio*
PEANUT	PreEquilibrium Approach to NUclear Thermalization
PET	*Positron Emission Tomography*
PM	Permanent Magnet
PMMA	polymethyl methacrylate
PT	Particle Therapy
QMD	*Quantum Molecular Dynamics*
RBE	*Relative Biological Effectiveness*
RMS	Root Mean Square
rQMD	*Relativistic Quantum Molecular Dynamics*
SCN	Scintillator detector
SHOE	Software for Hadrontherapy Optimization Experiment
SiPM	Silicon Photomultiplier
SOBP	*Spread Out Bragg Peak*
SPE	*Solar Particles Events*
SSB	Single Strand Breaks
SSSD	*Single-Sided Strip Detector*
STC	Start Counter
TCP	*Tumor Control Probability*
TDC	time to digital converter
TPS	*Treatment Planning System*
VTX	Vertex detector

Introduction

Nuclear fragmentation processes induced by the interaction of hadrons and nuclei with matter are of great interest not only in fundamental physics research but also in applied physics, as for example in particle therapy and space radioprotection. In both cases, nuclear fragmentation can highly affect the particle yields and the energy spectrum, which are fundamental for the calculation of the particle transport and the estimation of the dose. Therefore, accurate measurements of fragmentation cross sections are required to correctly develop treatment plans and assess the health risk in space missions.

The goal of particle therapy is to treat deep-seated tumors with high spatial selectivity exploiting the ions characteristic distribution of energy deposition and their high biological effectiveness. Nuclear fragmentation represents a potential risk, since it affects the planned dose map. When the therapeutic beam undergoes fragmentation (in case of $Z > 1$ beams), in fact, the produced lighter secondary particles have a higher penetration depth with respect to the beam, and their contribution must be considered in treatment planning. On the contrary, at the energies of interest, target fragments are characterized by a few tens of $\mu\mathrm{m}$ range. However, due to their high ionization power, they can relevantly contribute to the induced biological damage, especially in protontherapy, because the produced fragments have a significantly higher biological effectiveness with respect to protons.

Space radioprotection, instead, aims to develop effective shields to preserve astronauts from the harmful effects of ionizing space radiation. In particular, in long duration and far form Earth space missions, the integral dose received by the spacecraft crew members may represent a serious hazard to their health. Shields are therefore developed to protect them from the highly energetic space radiation. Nuclear fragmentation processes occurring within shield materials induce the production of lighter and highly penetrating radiation that should be taken into account in designing shielding systems.

At present, there is a lack of experimental fragmentation cross section measurements in the energy range of interest for particle therapy and space radioprotection applications. In particular, experimental data of nuclear interactions with the most abundant tissues nuclei are required. The energy range of interest for particle therapy extends from few tens of $\mathrm{MeV/u}$ up to about $400\,\mathrm{MeV/u}$. Instead, for space radioprotection,

higher energies have to be considered. In both cases the scientific community makes extensive use of Monte Carlo calculations. However, the available transport codes suffer from relevant uncertainties, since there is no exact calculable theory for nuclear interactions. The existing models need to be continuously improved and benchmarked with reliable experimental data. Additional data are therefore necessary also to allow the improvement and development of Monte Carlo models, which in any case remain essential tools in physics research. The use of Monte Carlo in particle therapy is, for example, an increasing necessity.

The FOOT (FragmentatiOn Of Target) experiment aims to experimentally measure fragments production cross sections for energies, beams and targets of interest for therapy and radioprotection in space. Notwithstanding the existing uncertainties, Monte Carlo calculations allowed to drive the design and the construction of two different experimental setups: an emulsion cloud chamber, dedicated to the measurement of lighter ($Z \leq 3$) fragments, and an electronic setup, that will measure heavier ($Z \geq 3$) fragments.

The main purpose of this work has been the construction and the maintenance of an accurate and reliable Monte Carlo simulation of the entire apparatus, on basis of the FLUKA code, focusing in particular on the study of design and expected performances of the electronic setup. The experiment, at present, is still in a development phase, and several parts of the detector are not built yet. At this stage, Monte Carlo simulations proved to be valuable tools to support the development process of detectors. Actually, in the past three years, in order to improve its performances, the FOOT setup layout underwent many changes, often driven by results obtained from Monte Carlo simulations.

In addition, in this work the fragment reconstruction capabilities of the FOOT setup are investigated. An analysis software has been developed to test the setup performances, in order to estimate the accuracy achievable with the expected detectors resolutions. The fragments charge and mass are therefore calculated from the combination of the measured quantities (time of flight, momentum, kinetic energy and energy loss in thin detectors), in order to provide the energy and angular yields required to estimate the production cross sections.

In Chap. 1, an overview of the most relevant aspects of ion interactions with matter is provided, as well as their biological effects. The role of nuclear fragmentation in particle therapy and space radioprotection is then investigated and the models implemented in Monte Carlo codes are presented. Finally a review of the existing cross section experimental data is reported.

In Chap. 2 the FOOT experiment is presented: aims, methods and strategies are explained. Both the electronic and the emulsion cloud chamber are described in details.

In Chap. 3, the simulation setup and framework is presented. A brief overview of the FLUKA Monte Carlo codes capabilities, physics models and technical aspects is firstly given, followed by the detailed building process of the FOOT simulations, with some considerations about time and memory usage.

Finally, in Chap. 4, a preliminary Monte Carlo based study on the detector performances is reported. After introducing the FOOT reconstruction software, fragment analysis and identification strategies and results are presented, as well as a first illustrative attempt of cross sections estimation.

CHAPTER 1

Nuclear interactions and radiobiology of charged particles

1.1 Introduction and general remarks

The scenario for ion beams cancer treatment is considerably different from that for ion radioprotection in space, but the overlap between the two situations is not negligible. Along with few heavy ions, such as silicon and iron, the particles of greatest interest in space radioprotection are mostly light ions, such as protons, helium, carbon and oxygen ions, which are exactly the same used in Particle Therapy (PT). Also the energy ranges of interest partly overlap (from tens of MeV to few GeV).

In both cases, a fundamental quantity, strictly related to the induced radiation damage, is the *dose* (D), or *physical dose,* which is defined as the ratio of the mean energy $\mathrm{d}\epsilon$ imparted by ionizing radiation in a volume element and the mass $\mathrm{d}m$ of the matter in that volume,

$$D = \frac{\mathrm{d}\epsilon}{\mathrm{d}m} \tag{1.1}$$

It is expressed in units of Gray (Gy), where $1\,\mathrm{Gy} = 1\,\mathrm{J\,kg^{-1}}$.

In the clinical use of ion beams, dose localization is one of the most relevant advantages compared to conventional photon-radiotherapy: the aim is to optimize the dose distribution in order to maximize the dose release in the tumor region and minimize it in the surrounding healthy tissues or *Organs at Risk* (OAR). In space radioprotection, instead, the dose must be minimized to the spacecraft crew members in order to reduce as much as possible any biological damage. In addition, for vessels electronic components the risk of failure due to radiation effects has to be evaluated.

Nuclear interactions, and particularly nuclear fragmentation, influence and modify both the dose delivered to a patient and the dose to which astronauts are exposed. Today, Monte Carlo (MC) transport codes are used to predict and simulate these interactions. However, experimental fragmentation cross sections are mandatory to validate MC nuclear models and improve the quality of treatment planning and radiation shielding. In all the subsequent considerations on the nuclear interactions, the quarks degrees of freedom will not be considered due to the negligible probability of these processes at the energies relevant in clinical use and in space radioprotection.

In this chapter, the role of charged particles (protons and ions) and nuclear interactions in medical physics is investigated. In Sec. 1.2, the physical interactions in matter in the energy range between tens of $\mathrm{MeV/u}$ to hundreds of $\mathrm{MeV/u}$ are presented. In

Sec. 1.3, the biological effect of ions compared to photons are outlined. In Sec. 1.4 the fundamental basis of PT ad radioprotection in space are presented, focusing on the role played by nuclear fragmentation. In Sec. 1.5 an overview of the nuclear models implemented in MC codes is reported. Finally, a summary of the cross sections relevant in these fields and available in literature is given in Sec. 1.6.

1.2 Interactions of charged particles with matter

1.2.1 Energy loss

As they pass through matter, protons and ions lose energy, and the average energy $\mathrm{d}E$ lost by a particle per path unit $\mathrm{d}x$ is called *stopping power*, and is defined as follows:

$$S = \frac{\mathrm{d}E}{\mathrm{d}x} \tag{1.2}$$

The unit of measure is $\mathrm{keV/\mu m}$.The *mass stopping power* for a given target material, instead, is obtained by dividing the stopping power by the density ρ.

The energy loss mechanisms of charged particles are:
- excitation or ionization of the electrons in the target
- elastic collisions with the nuclei of target atoms
- radiative emission of energy (*i.e.* Bremsstrahlung)

According to that, the total stopping power can be divided into three independent parts, each one corresponding to one of the three energy loss mechanisms:

$$S = S_e + S_n + S_r \tag{1.3}$$

where S_e is the *electronic stopping power*, S_n the *nuclear stopping power* (see Sec. 1.2.3) and S_r the *radiative stopping power*. At energies corresponding to velocities well below the

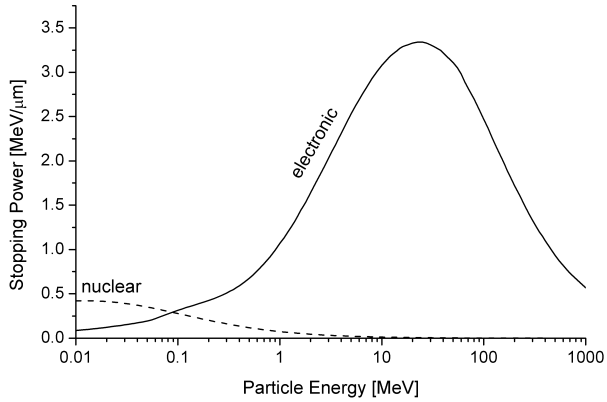

Fig. 1.1: Electronic and nuclear stopping power for Al ions in Al target as a function of particle energy per nucleon.

speed of light, the radiative contribution is negligible, while nuclear stopping power is relevant only at very low energies (Fig. 1.1). At intermediate energies, ions mainly lose energy through inelastic electromagnetic interactions with atomic electrons, *i.e.* they lose energy by ionizing and exciting of the absorbing medium atoms. Ionizations cause the production of secondary electrons, usually referred to as *δ-rays*, while the medium excited atoms decay by emitting photons.

The stopping power is strictly related to the *Linear Energy Transfer* (LET), a quantity frequently used in radiodosimetry and radiobiology. It is defined as the amount of energy released by a radiation in the traversed material per unit length and, differently from stopping power, it does not take into account radiative energy loss (*i.e.* the radiative stopping power or Bremsstrahlung) or delta-rays. In fact LET is defined as follows:

$$\mathrm{LET}_{\Delta} = \left(\frac{\mathrm{d}E}{\mathrm{d}x}\right)_{\Delta} \tag{1.4}$$

where $\mathrm{d}E$ is the mean energy loss due to collisions with atomic electrons with energy transfers less than a cut-off value Δ. Therefore, the cut-off value Δ excludes secondary electrons with energies greater than Δ (the symbol Δ is usually omitted). The reason for this cut-off is to have a quantity that measures only the energy deposited close to the trajectory of the incident particle. Instead the unrestricted LET (LET_{∞}) takes into account all possible energy transfers. LET is usually measured in $\mathrm{keV}/\mu\mathrm{m}$.

The ion energy loss per length traveled was firstly described by Bohr in a classical approach and then improved by Bethe and Bloch, who introduced quantum mechanics corrections. The *Bethe-Bloch formula*, that describes this process, is the following:

$$-\frac{\mathrm{d}E}{\mathrm{d}x} = 2\pi N_A\, r_e^2\, m_\mathrm{e}\, c^2\, \rho_m\, \frac{Z_m}{A_m}\, \frac{Z^2}{\beta^2} \left[\ln\left(\frac{2\, m_e, \gamma^2\, v^2\, W_{max}}{I^2}\right) - 2\beta^2 - \delta - 2\,\frac{C}{Z_m}\right] \tag{1.5}$$

where

- N_A is the Avogardo's number
- r_e and m_e are respectively the classical radius and mass of the electron
- ρ_m, A_m and Z_m are the density, the mass number and the charge of the medium respectively
- Z and $\beta = v/c$ are respectively the incident particle charge and velocity relative to the speed of light c, and $\gamma = 1/\sqrt{1-\beta^2}$
- I is the mean excitation potential
- W_{max} is the maximum energy transfer in a single collision which is kinematically limited to the value

$$W_{max} = \frac{2m_\mathrm{e}\, c^2 \beta^2 \gamma^2}{1 + 2\frac{m_\mathrm{e}}{m}\sqrt{1+\beta^2\gamma^2} + \frac{m_\mathrm{e}}{m}} \tag{1.6}$$

  where m is the particle mass
- δ is the *density effect*, which takes into account that the particle can polarize the atoms along its path, thus shielding from the full electric field intensity the electrons far from the its path

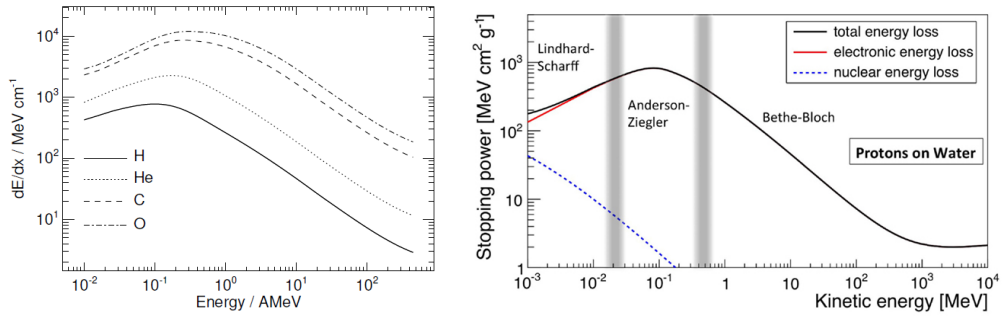

(a) (b)

Fig. 1.2: (a) Electronic stopping power of different ions calculated in water as a function of the energy (Parodi 2004) (b) Mass stopping power for a proton in water as a function of its energy: the nuclear contribution is relevant only at lower energies (Kraan 2015).

– and C is the *shell correction*, that considers the effects arising when particle and atomic electrons velocities are comparable.

This formula describes the mean rate of energy loss in the region $0.05 \lesssim \beta\gamma \lesssim 10^3$ for intermediate-Z materials with an accuracy of a few %. According to this formula, the energy loss per unit path length increases with the square of the particle charge (Fig. 1.2a).

The stopping power presents a dependence on the particles energy. Its trend for a proton as a function of its energy is depicted in Fig. 1.2b, where the contribution of both the electronic and the nuclear part are represented and can be described in terms of the relativistic parameter $\beta\gamma$. At $\beta\gamma \simeq 3$ it reaches a minimum of ionization, $\mathrm{d}E/\mathrm{d}x \simeq 2\,\mathrm{MeV\,g^{-1}\,cm^2}$, followed at higher energies by a *relativistic rise*, with a logarithmic dependence on $\beta\gamma$. At even higher energies ($\beta\gamma > 10^3$) the radiative effects become relevant and the Bethe-Bloch equation is not valid any more. On the contrary, as the particle energy decreases below the minimum of ionization region, the stopping power increases, according to the β^{-2} dependence in Eq. 1.5. Hence, a greater amount of energy per unit length is deposited toward the end of the particle path rather than at the beginning. When the particle velocity becomes comparable to the velocity of the atomic electrons of the material, shell corrections C/Z_m correct for atomic binding. As the particle further slows down, the rate of energy loss reaches a maximum and then drops again. At even lower velocities the particle captures electrons, and so its effective charge is reduced. Therefore, in Eq. 1.5 the particle charge Z has to be replaced by the *effective charge* Z_{eff}, which can be described by the following empirical expression:

$$Z_{eff} = Z\left(1 - \mathrm{e}^{-125\,\beta\,Z^{2/3}}\right) \tag{1.7}$$

Since $Z_{eff} < Z$, the rate of energy loss per unit track length decreases and the $\mathrm{d}E/\mathrm{d}x$ drops, causing in the depth-dose profile a distal falloff that is sharper for heavier ion than for the lighter ones. The maximum in the depth-dose profile is called *Bragg peak* (BP) (Fig. 1.3).

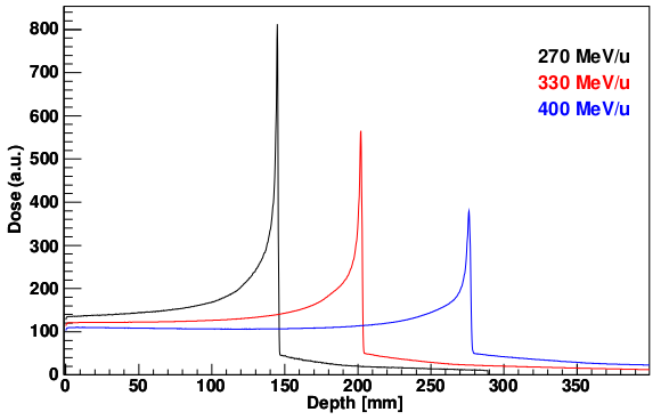

Fig. 1.3: Depth-dose distributions in water calculated by means of the FLUKA code (Ferrari et al. 2005; Böhlen et al. 2014) for the same number of primary carbon ions at increasing energies (Mairani 2007)

The Bethe-Bloch equation describes the average energy loss per unit length. In fact, traversing a material charged particles undergo a large number of interactions and transfer only a small fraction of their initial kinetic energy in each of these collisions, therefore the energy of the incident particle decreases slowly. Due to the stochastic nature of these processes, the energy loss of a monochromatic beam in an homogeneous target is not a delta function. If the target can be considered as thick, the total energy lost by the particle is the sum of a lot of independent small energy releases, which can be considered gaussian distributed. Therefore, in this case the energy loss distribution is well approximated by a gaussian function. If the absorber is thin, instead, fewer energy depositions occur, and the possibility of large energy transfer in single collisions cause a tail in the high energy region of the distribution. Theoretical calculations of this distribution have been firstly carried out by Landau (Landau 1944) and Vavilov (Vavilov 1957). These solutions have a different region of applicability and the discriminating parameter is the ratio

$$\kappa = \frac{\overline{\Delta}}{W_{max}} \tag{1.8}$$

where $\overline{\Delta}$ is the mean energy loss. The parameter κ evaluate the contribution for collisions characterized by an energy transfer value close to W_{max}:

$$\kappa \gg 1 \qquad \text{if the thickness material is large and/or } \beta \ll 1$$
$$\kappa \ll 1 \qquad \text{if the thickness material is small and/or } \beta \sim 1$$

Landau obtained the mathematical definition of the distribution for $\kappa \leq 0.01$:

$$f(x, \Delta E) = \frac{\phi(\lambda)}{\xi} \tag{1.9}$$

where x is the particle path length in the material (target thickness), ΔE the energy loss in this path length and ξ is the mean energy loss calculated from the first term of Eq. 1.5

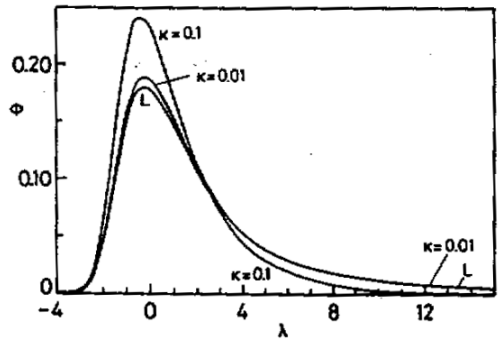

Fig. 1.4: Vavilov energy loss distributions for various κ, compared to the Landau distribution ("L" in the figure) for $\kappa = 0$ (Leo 2012).

and $\phi(\lambda)$ is the Landau function:

$$\phi(\lambda) = \frac{1}{2\pi \mathrm{i}} \int_{r-\mathrm{i}\infty}^{r+\mathrm{i}\infty} \mathrm{e}^{-u \ \ln u - u \, \lambda} \, \mathrm{d}u \tag{1.10}$$

where λ is a dimensionless number proportional to the energy loss, and r is any real positive number. This formalism, however, was obtained making some relevant approximations:

i) the mean energy loss is much lower than the maximum energy transfer W_{max}, which was considered not upper-bounded
ii) the mean energy loss is much higher than the electrons binding energy, which can be treated as free, and therefore any effect of atomic structure is neglected

Due to the approximation $W_{max} \longrightarrow 0$, the Landau distribution is characterized by an infinite Root Mean Square (RMS), hence the energy loss is not calculable and this theory is not adopted in nuclear models. A kinematic limit for the maximum energy transferable in a single collision was introduced by Vavilov, who therefore improved the Landau description of energy loss (Fig. 1.4). Landau's theory, however, played a crucial role in understanding the nature of the energy loss phenomenon.

1.2.2 Range

Given an homogeneous material, the depth at which the BP occurs depends on the beam energy. Since interactions are subject to statistical fluctuations, there are fluctuations also in the path length of individual particles. For a fixed particle type, beam energy and material the mean distance that an ion travels before coming to rest is called *mean range*. Fluctuations produce a *range straggling* which can be approximately described by gaussian range distribution. A similar but not identical quantity is the *CSDA range*: it is a close approximation to the average path length, calculated in the *Continuous-Slowing-Down Approximation*. In this approximation, the rate of energy loss at every point along the track is assumed to be equal to the total stopping power, disregarding energy-loss

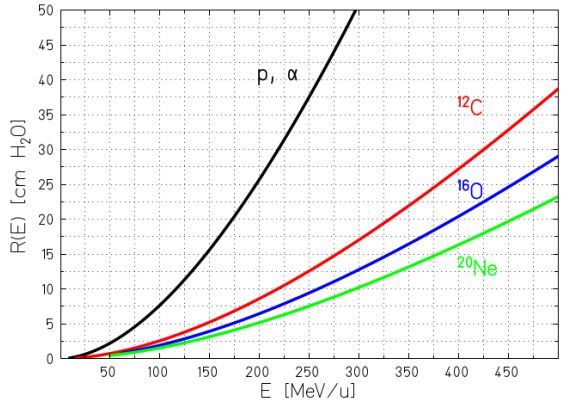

Fig. 1.5: Mean ranges of heavy ions in water (Schardt et al. 2010).

fluctuations. The CSDA range is related to the particle initial kinetic energy E_0 and its energy loss:

$$R(E_0) = \int_0^{E_0} \left(\frac{\mathrm{d}E}{\mathrm{d}x}\right)^{-1} \mathrm{d}E \tag{1.11}$$

Accordingly to Eq. 1.11, as the kinetic energy of the primary particle increases also the range becomes longer (Fig. 1.3).

The ranges of different ion with equal initial kinetic energy E per atomic mass unit and crossing the same absorber are related as follows:

$$R_1(E)\,\frac{{Z_1}^2}{m_1} = R_2(E)\,\frac{{Z_2}^2}{m_2} \tag{1.12}$$

where 1 (2) is for the first (second) ion. This means that, given a certain energy per unit mass, heavier ions show a shorter range than lighter ones (Fig. 1.5). In fact, according to Eq. 1.5 the energy loss is proportional to Z^2, so they loose a greater amount of energy per path length. For instance, being equal the energy per nucleon, the proton range is approximately three times the range of $^{12}\mathrm{C}$, while protons and $^{4}\mathrm{He}$ ions have the same range.

1.2.3 Multiple scattering

While the longitudinal profile of a proton or ion beam is dominated by electromagnetic interactions with atomic electrons, the traversal profile is due to elastic scattering on the nuclei of the medium. The scattering is both due to the cumulative effect of many small deflections and to single large deflections of few particles. The first type of process is called *Multiple Coulomb Scattering* (MCS), while the second is referred to as *Single Coulomb Scattering* and is usually negligible. Individual collisions are described by the *Rutherford formula*:

$$\frac{\mathrm{d}\sigma}{\mathrm{d}\Omega} = Z_m^2\, Z^2\, r_e \frac{(m_\mathrm{e}\, c/\beta p)^2}{4\sin^4(\theta/2)} \tag{1.13}$$

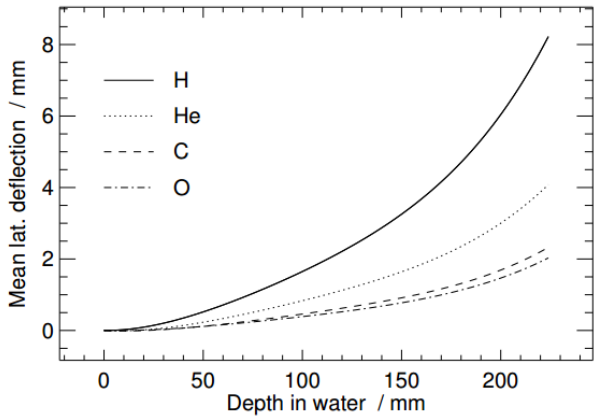

Fig. 1.6: Lateral deflection in water of some ion beams of clinical interest (Parodi 2004).

where $\mathrm{d}\sigma\,/\,\mathrm{d}\Omega$ is the angular differential cross section for scattering, p is the incident particle momentum and θ the scattering angle. Due to the $\sin^{-4}(\theta/2)$ dependence, the most of the particles are scattered at small angles. However, the cumulative effect of these small deflections is a change from the original particle direction, since statistically the probability of relevant deviations increases event by event.

The statistical distribution function $F(\theta, d)$ for the resulting scattering angle θ at penetration depth x is described in the theory of Molière (1948). For small angles ($\theta \simeq 0$) the higher order terms in Molière's solution can be neglected and the angular distribution can be approximated by a Gaussian function:

$$F(\theta, x) = \frac{1}{2\pi\sigma_\theta}\,\mathrm{e}^{-\left(\frac{\theta^2}{2\sigma_\theta{}^2}\right)} \tag{1.14}$$

The standard deviation σ_θ was calculated by Highland (Highland 1975):

$$\sigma_\theta = \frac{13.6\,\mathrm{MeV}}{p\,v}\,Z\sqrt{\frac{x}{X_0}}\left[1 + 0.038\,\log_{10}\left(\frac{x}{X_0}\right)\right] \tag{1.15}$$

where X_0 its radiation length, whose values can be found in tables. Targets made of heavy elements cause a larger angular spread than targets composed of light elements with the same thickness.

Eq. 1.15 shows that the angular distribution decreases as the particle momentum rises and therefore, for different ions at the same velocity, as the mass increases (Fig. 1.6). Hence, heavier charged particle beams exhibit a lower lateral spread and a sharper lateral dose falloff.

However, besides the electromagnetic part of the scattering process, also nuclear interactions contribute to the final net deflection suffered by the particle. These processes are not taken into account in the Molière theory, and their effect is the production of tails in the gaussian distribution of the scattering angle.

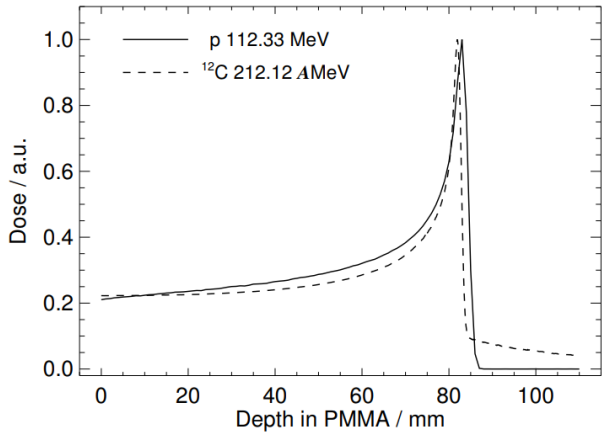

Fig. 1.7: BPs for proton and carbon ion beams with same range but different energies. For carbon ions, secondary particles produced in nuclear interactions cause the tail beyond the peak, while for protons the dose tail is absent.

1.2.4 Nuclear interactions

Charged particles can suffer nuclear interactions with the material nuclei. Nuclear interactions contribution to energy loss is much lower compared to electromagnetic interactions. However, while electromagnetic interactions are a well known and calculable process, although it can be quite complicated, a model that allows for a general calculation of nuclear interactions is still missing.

Nuclear reactions can be classified in:

- *Elastic collisions*. The involved nuclei are preserved and kinetic energy is conserved. These interactions contribute to spreading the beam (see Sec. 1.2.3).

- *Inelastic collisions*. In these reactions target nuclei may be broken, causing the release of secondary particles (neutrons, protons, heavier ions). The projectile itself may break into fragments if it is heavier than a proton. In this case total kinetic energy is not conserved.

In the following, only inelastic interactions will be investigated without taking into account the quarks degree of freedom, which can be neglected at the energies of interest for this work.

Projectile fragmentation leads to an attenuation of the primary particles: due to nuclear inelastic processes, a monochromatic incoming beam turns in fact into a mixed beam containing neutrons and lower-Z fragments, which may have a broad energy distribution and increased penetration depth according to Eq. 1.12. These fragments are responsible for a further energy deposition which results in a dose tail beyond the BP (Fig. 1.7).

At energies of hundreds of $\mathrm{MeV/u}$, nuclear spallation reactions may result in a complete disintegration of both projectile and target nuclei (*e.g.* in central head-on collisions),

or in partial fragmentations. However, the most frequent nuclear reactions are peripheral collisions, in which primary particles lose one or more nucleons. This process can be described with the *abrasion-ablation model* (Serber 1947): in the fist step, the *abrasion*, nucleons in the overlapping zone of the primary particle and target nucleus are abraded and form the hot reaction zone, named "fireball", while the other nucleons are almost unaffected by the process; in the second step, the *ablation*, the residual projectile, target fragments and the fireball de-excite by evaporating nucleons and light fragments (further details in Sec. 1.5). Fragments originated from the primary particles are forward peaked in the laboratory frame due to the high velocity of the projectile, and they have approximately the same velocity and direction of the beam. Fragments originating from the target nuclei at rest, instead, are emitted almost isotropically and with much lower velocities, so their stopping power is high, according to Eq. 1.5.

Nowadays, different models have been proposed to describe nuclear interaction processes, however a model valid at very low energies (eV-keV) as well as at high energies (GeV-TeV) is still missing. A summary of the theoretical models implemented in MC code is given in Sec. 1.5.

A fundamental quantity that characterizes nuclear interaction is the *nuclear cross section*, since it links the probability that a nuclear reaction will occur with beam and target properties. The cross section for a particular process can be defined as:

$$\sigma = \frac{N}{N_i} \frac{A}{\rho\, x\, N_A} \tag{1.16}$$

where N is the number of interactions and N_i the number of incoming particles, while ρ, A and x are the target density, mass number and thickness. The conventional unit is the barn (b), where $1\,\mathrm{b} = 10^{-28}\,\mathrm{m}^2 = 100\,\mathrm{fm}^2$. If N refers to any kind of interaction of the beam with the target, σ is called *total cross section*. N can be further restricted to select only the produced particles that are emitted in a certain solid angle portion $\mathrm{d}\Omega$ or in a certain energy range $\mathrm{d}E$. In this case *differential* ($\frac{\mathrm{d}\sigma}{\mathrm{d}\Omega}$ and $\frac{\mathrm{d}\sigma}{\mathrm{d}E}$) or *double-differential cross sections* ($\frac{\partial^2\sigma}{\partial\Omega\partial E}$) can be defined. If N is restricted to events of a certain type, it is possible to define define *partial cross sections*, as for example $\sigma_{elastic}$ and $\sigma_{inelastic}$. *Fragment production* or *elemental cross sections* quantify the probability of the production of fragments with a given charge, while *isotopic cross sections* describe the production of a fragment with a given charge and mass.

Experimental data about nuclear cross sections are abundant in literature, but for light fragments ($A < 20$) the energy range between tens and few hundreds of $\mathrm{MeV/u}$ has not been completely covered by experimental measurements (see Sec. 1.6).

1.3 Biological effects of charged particles

1.3.1 DNA damages and cell survival

When ionizing radiations traverse a cell, they lose energy due to physical interactions, in particular they can ionize and excite atoms of the *deoxyribonucleic acid* (DNA) molecule or of other surrounding molecules, which may convert into *free radicals*. Free radicals are

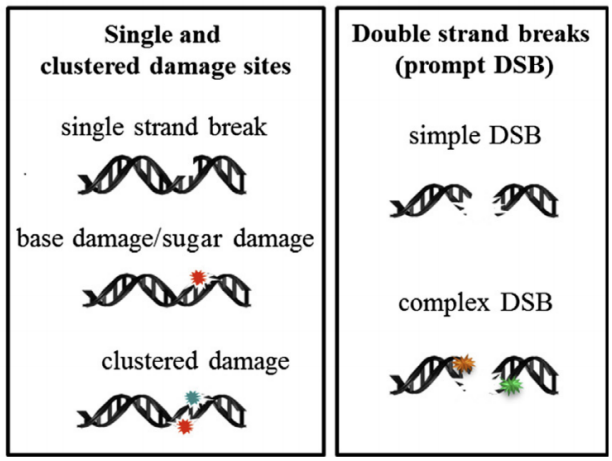

Fig. 1.8: Summary of the DNA damages (Lomax et al. 2013). The colored stars represent lesions induced to a DNA base or sugar, which are constituents of the DNA double helix.

atoms or molecules having unpaired electrons, and so they are highly reactive and their probability of interaction with DNA molecule is high.

DNA damages are typically classified as follows:

- *direct damages*, when the radiation breaks directly the DNA molecule;
- *indirect damages*, which are generated by radiation-induced free radicals.

DNA damages can disable the cell reproduction capability or even lead to cell death. The main structural type of DNA damage (Fig. 1.8) are:

- Single Strand Breaks (SSB), namely the damages involving only one of the two strands of the DNA double helix. They are of little biologic consequence, because they can be easily repaired by the cell by using the opposite strand as a template;
- Double Strand Breaks (DSB), which occur when two strands opposite one another or separated by only a few base pairs are damaged;
- clustered lesions, that occur when two or more lesions are formed within a few tens of DNA base pairs.

The probability of inducing a certain type of damage, is mostly related to particle LET. In fact, the induced damage severity can be explained in terms of the different energy deposition distributions of X-rays and ions. X-rays mostly deposit energy into the cell by photoelectric effect or by Compton effect. Since the cross sections for these processes are low, the number of ionizations per incident photon within a cell volume is also small, so many photons are required to deposit a significant dose, and the ionization density can be assumed to be homogeneous over the entire cell volume. The spatial distribution of energy is completely different for heavy ions: charged particles have higher LET because of their higher energy deposition along their track (Fig. 1.9), which results in a greater probability of causing DNA damages. The LET varies along

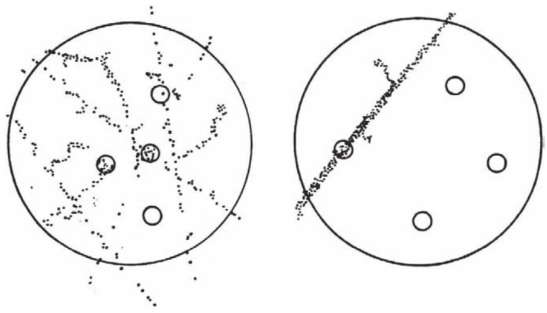

(a) (b)

Fig. 1.9: Ionization density in a medium irradiated by X rays (a) and high LET particles (b). The small circles represent biological targets and the dots represent ionizations produced along the tracks (Barendsen 1994).

their track because, as they deposit energy in tissue, they slow down and thus the rate of delivered energy increases. In medical physics, radiations are categorized into *low* and *high LET radiations* (or *sparsely* and *densely ionizing radiations* respectively): ions are considered to be high LET radiations (typical values range from tens of $\mathrm{keV/\mu m}$ to hundreds of $\mathrm{keV/\mu m}$) whereas X- and -rays are low LET radiations (typical values are of the order of few $\mathrm{keV/\mu m}$) due to their sparse ionizations.

For low LET radiations the contribution of indirect DNA damages (about 65%) is larger than the direct ones (about 30%), and only $\sim 30\%$ of DSB are clustered, while for high LET ions, the contribution of direct hits is higher and the clustered damages rise to about 70% (Friedland et al. 1999; Nikjoo et al. 1999).

The different behaviour in response to photons and heavy ions can be represented by cell survival curves (Fig. 1.10a): cell proliferation is analysed after irradiation and the percentage of surviving colonies is plotted as a function of the delivered dose. The surviving fraction is the ratio between the number of surviving cells and the number of the seeded ones, and it is conventionally plotted versus the dose on a log-linear scale.

The shape of cell survival curves depends on the type of radiation. For low-LET radiation, the curve is characterized by a shoulder region over the low dose range, while for higher doses it tends to be linear. This behavior is well described by the "linear-quadratic model":

$$S(D) = \mathrm{e}^{-\alpha D - \beta D^2} \tag{1.17}$$

where S is the surviving fraction, D is the absorbed dose and α and β are experimentally determined parameters that characterize the behaviour of cells when irradiated. The shoulder of the survival curve is determined by the α/β ratio.

The α/β ratio related to photon irradiation is used to characterize the cell type in terms of radiosensitivity: a low α/β ratio is associated with late responsive cells, whereas a high ratio is linked to early responding cells. Radiosensitivity differs from cell line (*i.e.* the particular type of cell) to cell line and it is also influenced by the cell cycle phase.

The response to densely ionizing radiation shows a lower dependence on cell type

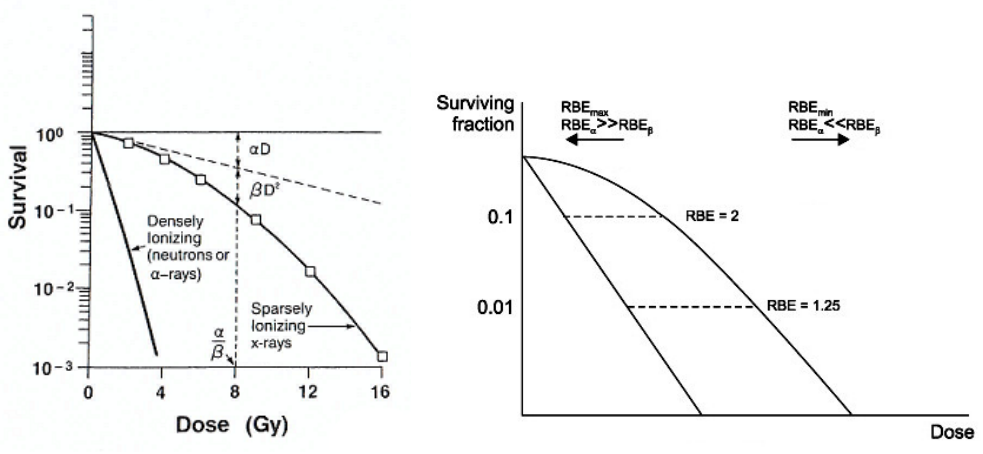

(a) (b)

Fig. 1.10: (a) Cell survival as a function of dose for densely and sparsely ionizing radiation (Hall et al. 2006). (b) Representation of the RBE as the ratio between D_X and D (Choi & Kang 2012).

and presents a less remarkable shoulder region: as the radiation LET increases, in fact, the slope becomes steeper because of the more severe damages produced by high LET radiation. Therefore, the survival curve shows a purely exponential behaviour, as described by the "linear model":

$$S(D) = e^{-\alpha D} \tag{1.18}$$

which differs from Eq. 1.17 since the quadratic term of the exponential has been neglected.

1.3.2 Relative biological effectiveness

Since cells response to irradiation is highly dependent on the radiation type, equal doses of different LET radiations may not produce the same biological response. This effect is quantified by the *Relative Biological Effectiveness* (RBE), which is defined as the ratio of the dose D_X of a reference radiation, typically photons (γ-rays from ^{60}Co or X-rays), to the dose D of the radiation of interest that produces the same biological effect:

$$\mathrm{RBE} = \frac{D_X}{D} \tag{1.19}$$

It can be defined for many biological endpoints such as cell killing at various survival levels, DNA strand breaks, mutations, and others.

The RBE is a quite complex quantity, since it depends on many physical and biological parameters (LET, dose, dose rate, fractionation, particle mass, cell radiosensitivity, biological endpoint, oxygen concentration, cell cycle phase, proliferation rate, etc.).

Due to the different shapes of the dose-response curves, the RBE is strongly dependent on dose and survival level (Fig. 1.10b): at high doses it is low and increases at lower doses up to a maximum, that represents the initial slopes of the dose effect curves.

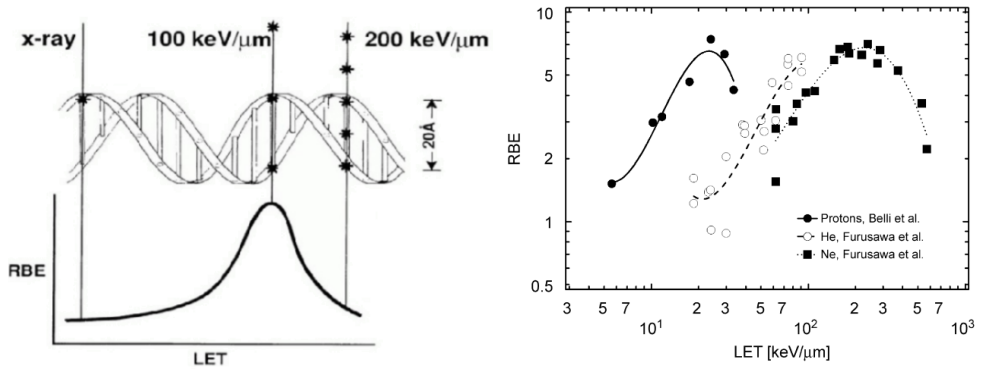

(a) (b)

Fig. 1.11: (a) The RBE as a function of LET (Hall & Hei 2003). (b) Comparison between different particles RBE curves as functions of LET (Jäkel 2008). Data for protons are taken from Belli et al. (1998), data for helium and neon ions from Furusawa et al. (2000).

Since due to the high energy deposition density the radiation damage is severe, in case of high LET particles the RBE is high. In clinical practice, proton RBE is considered constant and equal to 1.1 according to ICRU (ICRU 2007) recommendations. Protons are therefore considered 10% more effective that photons, despite of the experimental findings. This choice is due to the fact that proton LET along the track does not increase as much as for heavier ions. Other ions RBE, instead varies significantly, *e.g.* up to values > 3 in case of carbon ions. In fact, the RBE increases with LET up to an ion dependent maximum value (ranging from about 100 to $200\,\mathrm{keV/\mu m}$ for $Z > 1$ ions), reached when the distance between two subsequent interactions is comparable to the transversal dimension of DNA ($\sim 2\,\mathrm{nm}$) and decreases as LET increases further (Fig. 1.11a). This fall is due to the overkilling effect: the energy deposited in a cell by a single particle traversal is higher than the amount required to kill the cell. Thus, the further dose deposited by ions with an even higher LET is "wasted" and the RBE falls.

The particle type influences the position of the RBE maximum. For heavy particles, the maximum is typically shifted to a higher LET (Fig. 1.11b). In fact, at the LET corresponding to the protons RBE maximum, heavier ions are faster than protons, thus resulting in broader tracks with reduced ionization density. Therefore, light particles are generally more effective than heavy particles at the same LET.

To predict the RBE of ions other than protons different models have been developed in recent years. The most used in clinics are:

- the *Local Effect Model* (LEM), which is mostly diffused in Europe, since it is used at Heidelberg Ion-Beam Therapy Center (HIT) in Germany and at Centro Nazionale di Adroterapia Oncologica (CNAO) in Italy, and was developed at Gesellschaft für Schwerionenforschung (GSI) by Scholz & Kraft (1996). It relates the response of biological tissues after ion irradiation to the corresponding response after X-ray irradiation, assuming that the radiation biological effect is entirely determined by

the spatial local dose distribution within the cell nucleus. For a given cell, the differences in the biological action of charged particles are attributed to the different spatial energy deposition pattern, *i.e.* track structure.

- the *Microdosimetric Kinetic Model* (MKM), that is mostly spread in Japan and was proposed by Kanai et al. (1999). In this model the RBE trend is described as due to the variation of the energy deposited in microscopic sub-cellular volume.

The RBE is one of the most important quantities in heavy ion treatment planning, since it determines the photon equivalent dose, usually named *biological dose* or *RBE weighted dose*, obtained by multiplying the absorbed *physical dose* (see Sec. 1.1) by RBE. The biological dose quantifies the dose of conventional radiation that would produce the same biological effect as the radiation of interest. In the past, the most used biological dose units were the Gray-Equivalent (GyE) or Gy(RBE), which is obtained by weighing the physical dose with the RBE measured in the BP.

1.3.3 Oxygen enhancement ratio

When a tumour grows in volume, the phenomenon of *angiogenesis* takes place: new blood vessels are created in order to supply oxygen to the cells in the tumour center, which are too far from the original vessels to be sufficiently oxygenated. However, often these new vessels are not generated fastly enough or they might also be defective, therefore hypoxic regions are frequent, especially in the core of large tumours. It has been proved that hypoxic cells are more radioresistant, and thus a successful treatment of hypoxic tumours poses a specific challenge in radiation therapy.

The oxygen effect is quantified by the *Oxygen Enhancement Ratio* (OER),

$$\mathrm{OER} = \frac{D_{hypoxic}}{D_{oxic}} \tag{1.20}$$

where $D_{hypoxic}$ and D_{oxic} are the doses resulting in the same biological or clinical effect with hypoxic and normoxic cells respectively. Typically, the OER is about 3 for photons, whereas it is greatly reduced to about 1 in the case of higher LET particles (Furusawa et al. 2000). This means that high LET radiation is particularly suited to treat radioresistant tumors, since they are more effective than photons at the same dose level.

The oxygen effect is probably related to indirect damage, which is significant for low LET radiations: it has been postulated that molecular oxygen contribute to "fix" (*i.e.* make permanent) the damage induced by free radicals, so that the cell can not repair it. Since the role of indirect damages is not predominant for high LET radiation, the presence of oxygen is not crucial to produce severe lesions, and a lower dose is sufficient to impair cell replication capability.

1.4 Two relevant cases: particle therapy and radioprotection

During the last century, physics, and in particular nuclear and particle physics, has greatly contributed to the development of instrumentation for medical research, diag-

nosis and therapy. In particular, the curative capability of ionizing radiation in the treatment of tumors has been exploited since the beginning of 20^{th} century. Nevertheless, ionizing radiations also represent a potential risk to human health. Radioprotection is a medical physics branch that studies and regulates methods and devices meant to protect people from detrimental effects of radiations in a various spectrum of situations, from radiology rooms to a space travels.

Charged particles plays a key and opposite role both in PT and space radioprotection: thanks to their favorable dose deposition profile they are extremely suited to treat deep-seated tumors, while in space they can cause severe DNA damage to astronauts and increase secondary cancer risk. In this section, the effects of charged particles and nuclear fragmentation in these two environments will be compared and contrasted.

1.4.1 Particle therapy for cancer treatment

In 2012, 14.1 million new cases of cancer occurred worldwide (Torre et al. 2015). Nowadays, about 50% of oncological patients undergoes a radiotherapy treatment, together with surgery or chemotherapy or both. Radiation therapy is a cancer treatment that involves the use of ionizing radiation to damage the DNA of tumor cells, and is one of the most established and world-spread tumor therapy techniques. In an ideal radiotherapy treatment, only the tumor volume is irradiated, while the surrounding healthy tissues are completely spared, so that only cancerous cells are damaged and destroyed. However, in practice this is not feasible because of the unavoidable irradiation of the tissues placed upstream and downstream the tumor, which receive a certain amount of dose that depends on different factors, such as particle type, energy and many others.

The aim of radiotherapy is therefore to give sufficient dose to the tumor region to achieve local control without inducing severe complications in the surrounding healthy tissues. As the dose delivered to the tumor increases, the *Tumor Control Probability* (TCP), which is the probability of killing the tumor, increases. However, TCP is limited by the *Normal Tissue Complication Probability* (NTCP), *i.e.* the probability of induce side effects to healthy tissues, which also increases with dose (Fig. 1.12). The rationale of radiotherapy lies in the region between TCP and NTCP curves, that is called *therapeutic window*: the farther the curves are, the higher the probability of tumor control without normal tissue complications is.

At the beginning of radiotherapy history, many hospitals used γ-rays from radioactive isotopes, such as ^{60}Co. Radioactive sources were progressively replaced by compact *linear accelerator*s (LINACs), which provide high energy photons ($\sim\text{MeV}$), usually referred to as X-rays (although X-rays are conventionally defined as photons with energy ranging from $100\,\text{eV}$ to $100\,\text{keV}$). This kind of radiotherapy is usually referred to as *conventional radiotherapy*.

When traversing a medium, photons lose their energy, and consequently deliver dose to the material, principally by three well known processes, according to their initial energy and the atomic number of the target atoms:

- *Photoelectric effect*. The photon interacts with a bound electron of an atom and releases all its energy to the electron, which gains sufficient energy to be emitted.

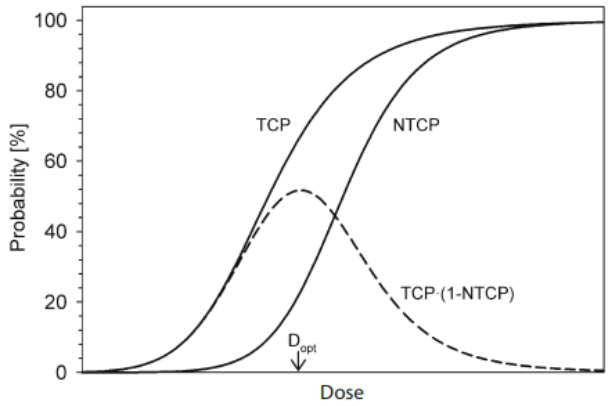

Fig. 1.12: Dependence of TCP and NTCP on dose. In the region between these curves, the so-called therapeutic window (dashed line), the probability of tumor control without normal tissue complications reaches a maximum at the optimum dose D_{opt} (Karger 2006).

- *Compton scattering*. The photon interacts with an outer orbital electron and releases part of its energy to the emitting electron, so that the photon is scattered with decreased energy.
- *Pair production*. The photon energy is converted into the mass and kinetic energy of an electron and a positron.

Typical photons depth-dose distributions at therapeutic energies are represented in Fig. 1.13: after an increasing dose region caused by escaping secondary electrons, the curve reaches a maximum and then it is exponentially attenuated, according to the well known exponential formula:

$$I(x) = I_0 \, \mathrm{e}^{-\mu x} \tag{1.21}$$

where I_0 is the incident beam intensity, x the traversed thickness and μ the *attenuation coefficient*, which is dependent on the material and the total interaction cross section.

The maximum depth depends mainly on the beam energy: the higher the initial energy is, the deeper the maximum is sited. For example, in case of typical radiotherapy with $6\,\mathrm{MeV}$ X-rays the maximum occurs at a few centimeters depth, while in case of diagnostic $100\,\mathrm{keV}$ photons the build-up region is not even observable.

Due to the typical longitudinal profile with a long exponential tail, the most of the energy is therefore deposited superficially rather than deeply. The proximal dose in the normal tissue is higher than the dose delivered to the tumor, and also tissues beyond the tumor region receive a non-negligible dose. Because of the non optimal dose distribution, in conventional radiotherapy the unavoidable dose delivered to the healthy tissues is a limiting factor to achieve the best tumor local control. This is why usually more photon beams from different directions are combined: the beams intersection corresponds to the target volume, hence the maximum of the dose is delivered to the tumor and minimized in the surrounding healthy tissues. The most advanced type of high-precision

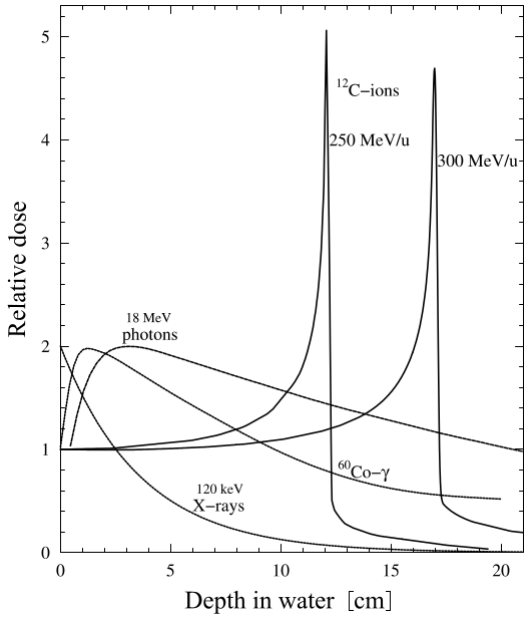

Fig. 1.13: Comparison of depth-dose distribution for different radiation types (Kraft 2000).

photon radiation therapy is the *Intensity Modulated Radiation Therapy* (IMRT), in which the beam is divided into many "fields" (*i.e.* space regions traversed by radiation), and the intensity of each field is adjusted individually (Fig. 1.14 top). This technique allows to further reduce the amount of radiation absorbed by healthy tissues surrounding the tumor.

In the last few decades, other types of radiations, especially nuclear particles, have been clinically evaluated. The particle radiation of major interest are accelerated ionized nuclei, in particular hydrogen and carbon. This therapy is commonly known as *Hadrontherapy* or Particle Therapy, and the interest in this new kind of radiotherapy arises from ions physical and radiobiological properties (see Sec. 1.2 and 1.3) and from the encouraging and successful clinical outcomes.

At present, more than 80% of patients receiving a radiotherapy treatment are treated with X-rays, while the others are irradiated with other special techniques, as *gamma knife* (*i.e.* an extremely precise form of radiotherapy which focuses intense beams of γ-rays with pinpoint accuracy to treat brain tumors) and *brachitherapy* (*i.e.* a radiotherapy technique involving the implant of a sealed radiation source near or within the tumor volume). Less than 1% of the radiotherapy patients receive a hadrontherapy treatment (Durante & Paganetti 2016) and, between 1954 and 2016, the patients treated with protons or heavier ions were about 175 thousand [1]. This therapy requires high level technologies and expertise, which are demanding in terms of cost. However, this kind of therapy is quickly spreading due to the encouraging clinical results.

While therapeutic photon beams can be produced by means of a LINAC, charged

[1] www.ptcog.ch

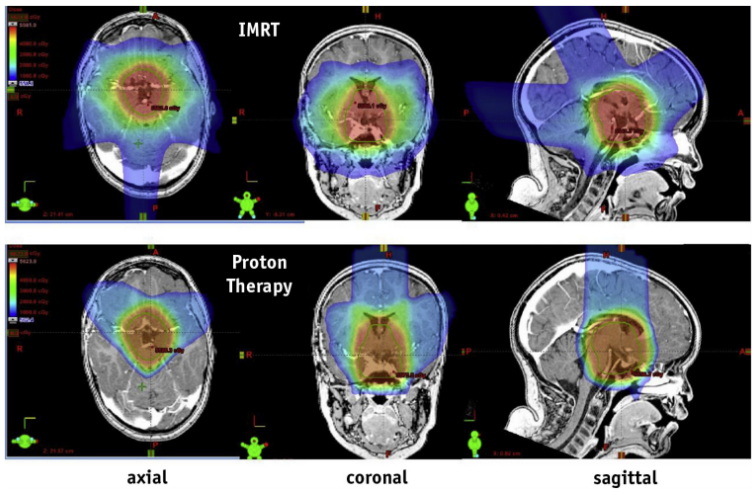

Fig. 1.14: Brain tumor photon IMRT (top) and proton (bottom) comparison plans in three planes (axial, coronal and sagittal) (Indelicato et al. 2016).

particles require more sophisticated accelerators. The accelerators used today in PT are:

- *cyclotrons*, which operate with constant magnetic field and radiofrequency, producing fixed energy beams. The particles are kept in a spiral trajectory and their final energy depends on the radius, and therefore on the size, of the machines. Cyclotrons are commonly used to accelerate protons, while heavier ions would require a higher magnetic field to maintain the beam trajectory and greater dimensions of the machine to achieve therapy energies. This restriction could be at least partly overcome by the use of superconducting cyclotrons.
- *synchrotrons*, which accelerate the beam by means of a radiofrequency, holding it in a constant radius trajectory by means of a variable magnetic field (Fig. 1.15). Both the radiofrequency and the magnetic field are synchronized with the rising energy of the particles. The final energy can therefore be varied according to the needs. Synchrotrons are the preferred solution to accelerate ions like ^{12}C and ^{16}O.

Contrary to conventional radiotherapy, in case of charged particles only few beams are needed to deliver the prescribed dose to the tumor region (Fig. 1.14 bottom). Therefore, comparing photons and ions, the same dose can be delivered to the tumor with lower integral dose to the normal tissues in case of charged particles beams. In particular, PT allows for a higher degree of dose conformation to the tumor volume compared to photons thanks to charged particles dose distribution with a pronounced dose maximum and sharp dose fall-off (see Sec. 1.2.1): taking into account the body composition and adjusting the beam energy, the BP can be longitudinally moved inside the patient to precisely reach the tumor depth. The favorable peak-to-plateau ratio compared to photons is the main reason why PT is especially suited to treat deep-seated tumors.

However, a single monoenergetic beam produces a BP which is too narrow to irradiate the entire cancer volume, therefore several BP with different energies are combined

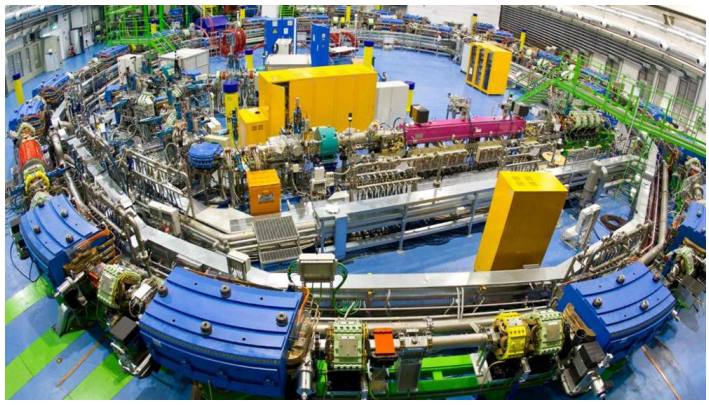

Fig. 1.15: The CNAO synchrotron (`www.fondazionecnao.it`).

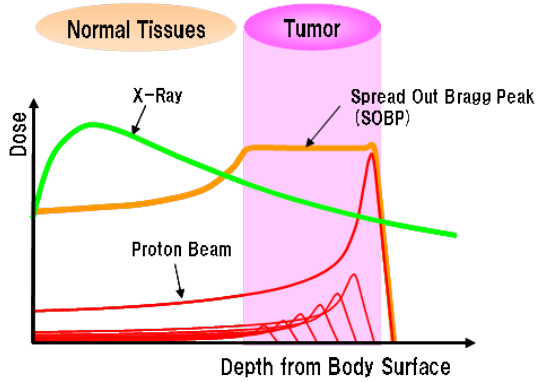

Fig. 1.16: Comparison between dose (Gy) distribution of X-rays and of a SOBP obtained by superimposing several BPs as a function of penetration depth (cm) inside the patient.

to create the so called *Spread Out Bragg Peak* (SOBP), so that a uniform dose is delivered in the longitudinal profile across the tumor volume (Fig. 1.16). This can be done by *passive modulation* of the beam, *i.e.* by interposing passive layers that tailor the beam energy distribution, or by *active modulation*, *i.e.* by varying the energy during the treatment delivering, thus scanning subsequent tumor "slices" with a pencil beam. The active beam delivery provides more accurate dose distribution and reduce the production of secondary particles and neutrons inside the passive thicknesses, that can cause radioinduced secondary cancer.

Due to the high spatial precision of charged particle dose deposition, PT treatments are more sensitive to beam range uncertainties than conventional photon treatments. A wrong estimation of the range produces a shift of the Bragg peak position, leading to an under-dosage of the tumor volume and an over-dosage of healthy tissue placed before or beyond the tumor. Common error sources are patient motion (*e.g.* breathing), anatomical changes (for example tumor regression or patient weight loss) occurred during the duration of the treatment (which ranges between two and eight weeks, according

to the tumor size, the prescribed total dose and the particle used) and others. Currently, systems capable of checking the target volume dose conformity during or right after the treatment are under investigation (see below in this Sec.).

Thanks to the high LET and therefore high RBE (see Sec. 1.3), the use of charged particles is especially advisable to treat radioresistant and hypoxic tumors: in this case the biological potential of ions can be fully exploited to improve the TCP with minimum NTCP. Moreover, as the particle charge and mass increase, the lateral scattering diminishes, therefore the lateral beam profile is narrower. This is particularly advantageous since it allows to better spare the healthy tissues placed beside the tumor. This might seem to suggest that the highest possible Z should be used, in order to maximize the peak-to-plateau ratio and the LET and to minimize the lateral broadening. However, the dose tail beyond the BP produced by nuclear interactions increases with the primary charge, thus worsening the distal fall-off of the dose profile. At present, protons and $^{12}\mathrm{C}$ ions are the most widely used: proton beams have the advantage of having no fragmentation tail and their radiobiology is simpler to be handled in clinical treatments, while carbon ions present a higher peak-to-plateau ratio and a higher RBE. Recently, a new interest in $^{4}\mathrm{He}$ ions is also growing: in this case nucleons are especially tightly bound, making them relatively less likely to fragment. Moreover, when they undergo fragmentation they mostly produce hydrogen isotopes which, for a given kinetic energy per nucleon, have approximately the same range as the primary helium ion, according to Eq. 1.12, thus considerably reducing the distal edge problem.

Protons used in therapy are accelerated to energies ranging between 60 and $250\,\mathrm{MeV}$ ($\beta \simeq 0.6 - 0.7$, corresponding to $\beta\gamma \simeq 0.75 - 1$), that corresponds to a $15 - 35\ \mathrm{cm}$ range in water. At these energies, proton LET is around $1\,\mathrm{keV/\mu m}$, while on the SOBP it increases with depth in a range of $2 - 6\ \mathrm{keV/\mu m}$ (Paganetti 2014). To reach the same penetration depths, carbon ions must have an energy of about $120 - 400\ \mathrm{MeV/u}$, with corresponding LET in the entrance entrance channel between 11 and $13\,\mathrm{keV/\mu m}$, and a higher LET on the SOBP in the range $40 - 90\ \mathrm{keV/\mu m}$.

Nuclear interactions play a non negligible role in PT: they influence the dose map due to differing fragment ranges and angular distributions and they alter the LET spectra which results in a difference of RBE for the same delivered dose. These interactions are mostly undesirable when they occur in the entrance region before the BP, since they can undermine one of the primary advantages of PT, the favorable peak-to-plateau dose ratio. Hence, a good knowledge of these processes is essential for the calculation of the beam transport and the evaluation of fragments contribution in a treatment to optimize both proton and heavy ion irradiation.

Beam models adopted in *Treatment Planning System* (TPS), which are computer based system used to calculate and optimize the treatment, must take into account the effects of nuclear fragments and their validation against experimental data is mandatory. In fact, the impact of how the nuclear interactions are modeled can be significant: an inelastic nuclear cross sections uncertainty of 20% can lead to a change of a carbon physical dose distribution of more than 10% in the SOBP region for a large and deep-seated tumor (Lühr et al. 2012).

In the therapeutic energy range, nuclear fragmentation interactions have not been

fully explored by experimental measurements, therefore MC simulations are the only available tool to predict fragments spectra. These suffer from many uncertainties since, as explained in Sec. 1.2.4, no calculable model is available to describe these processes. Recently, some experiments have been performed to investigate fragmentation interactions for a carbon beam (Dudouet et al. 2013), but only few energies in the lower part on the therapeutic energy range have been explored. Experimental data about target fragmentation for proton beams are lacking, since fragments have a very short range, approximately tens of $\mu\mathrm{m}$, therefore their detection and identification is not a trivial task. Moreover, nowadays a great interest in new ion species is growing: oxygen ions have a very high LET, which makes them especially attractive for the treatment of hypoxic tumors, and helium ions present an improved lateral dose distribution and a higher RBE with respect to protons, bus also a reduced fragmentation tail compared to heavier ions. Nuclear fragmentation channels for these new ions have still to be investigated.

Since the biological response depends on the composition of particle field, *i.e.* the produced fragments, and on LET and energy distributions, differential cross sections for the production of different fragments have to be experimentally studied for the ions species of interest at different energies in the therapeutic range.

As seen in Sec. 1.2.4, fragmentation products can be divided in *target fragments* and, in case of $Z > 1$ beams, *projectile fragments*.

Target fragments

They are produced at a very low velocity and therefore their range is very small, of the order of tens of $\mu\mathrm{m}$ (Fig. 1.17a). They are characterized by a higher LET with respect to the protons, hence their biological effectiveness can be high. This is due to the high amount of their local energy deposition in a very short range.

Target fragments are mostly relevant in protontherapy, where no beam fragmentation can occur: in fact, the production of heavy, slow and thus densely ionizing fragments can seriously affect the biological effectiveness of the primary beam. In clinical practice proton RBE is, as explained in Sec. 1.3.2, considered constant and equal to 1.1, independently of the tissue irradiated, dose per fraction, total dose and beam energy, even if the experiments show a significant increase in RBE above this value (Tang et al. 1997). The value of 1.1 was deduced as an average value of RBE values mostly measured in the early days of proton therapy and averaged on various endpoints at $2\,\mathrm{Gy}$. Proton RBE variability is a hot topic in the radiobiology community, and target fragments may be one of the factors playing a role in this phenomenon.

Since the ratio between fragmentation and electromagnetic cross sections is higher for high energy beams, the fragments contribution is more likely higher in the entrance channel, and therefore in correspondence to healthy tissues preceding the tumor region. In a recent work by Tommasino & Durante (2015), it has been suggested that about 10% of the biological effect induced in the entrance channel might be associated with target fragments, while it decreases to 2% in correspondence to the BP (Fig. 1.17b). Hence, even though the production cross sections are low, they must be considered during the treatment planning stage since they can affect NTCP outcomes.

Fragment	E (MeV)	LET (keV/µm)	Range (µm)
^{15}O	1.0	983	2.3
^{15}N	1.0	925	2.5
^{14}N	2.0	1137	3.6
^{13}C	3.0	951	5.4
^{12}C	3.8	912	6.2
^{11}C	4.6	878	7.0
^{10}B	5.4	643	9.9
^{8}Be	6.4	400	15.7
^{6}Li	6.8	215	26.7
^{4}He	6.0	77	48.5
^{3}He	4.7	89	38.8
^{2}H	2.5	14	68.9

(a)

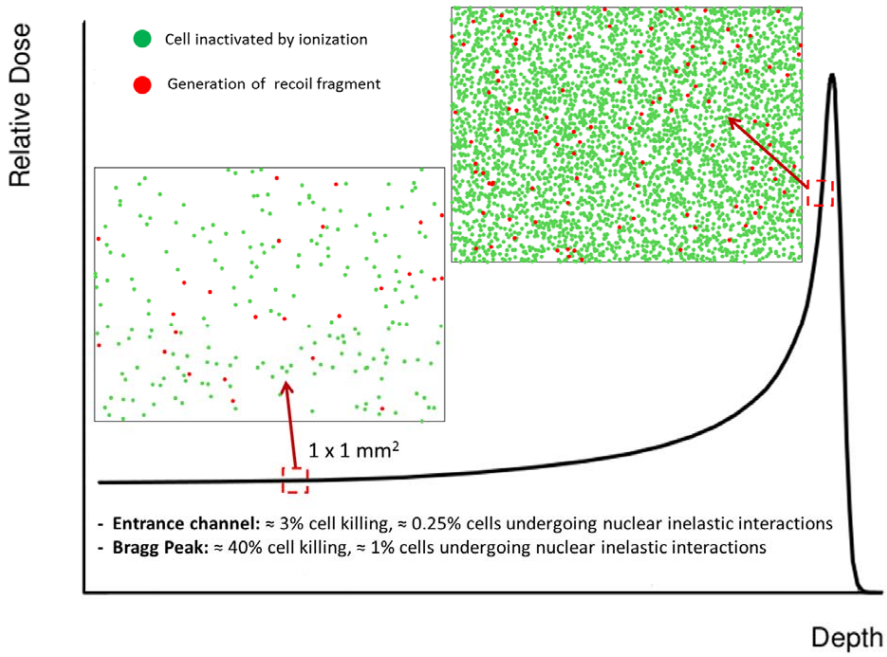

(b)

Fig. 1.17: (a) Expected average energy, LET and range for target fragments produced in water by a 180 MeV proton beam (Tommasino & Durante 2015). These results have been retrived by means of an analytical model. (b) Representation of the impact of ionization and target fragmentation in tissues (Tommasino & Durante 2015) at different positions along the Bragg curve (dose in arbitrary units and depth of the order of cm).

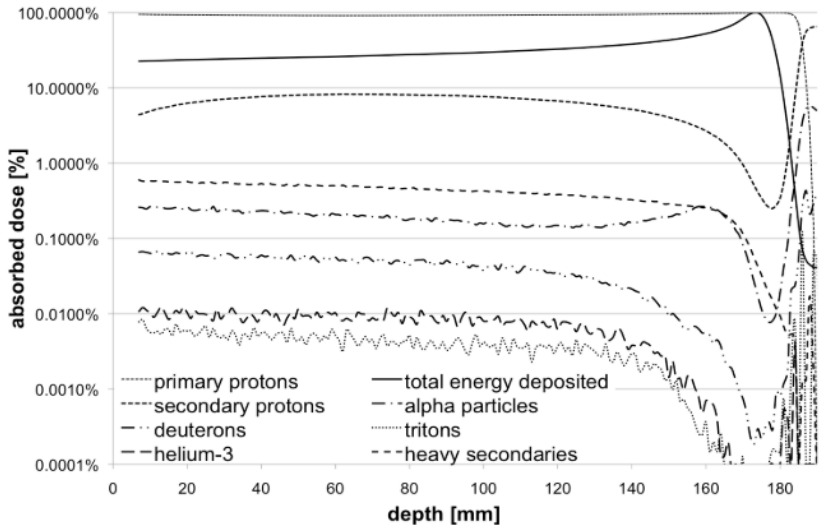

Fig. 1.18: Dose released by different secondary particles originated from a $160\,\mathrm{MeV}$ proton beam in a water phantom (Grassberger & Paganetti 2011).

In a study by Grassberger & Paganetti (2011) the particle yield from different nuclear interaction channels as a function of proton penetration depth was studied by means of MC simulations for proton beams. The study highlighted that contributions to the physical dose of secondary protons, deuterons, tritons, $^3\mathrm{He}$, α-particles and heavier ions differ by orders of magnitude (Fig. 1.18), however biological effectiveness was not considered. The dose from secondary protons showed a build-up effect, caused by their significant range, while other secondaries ranges are much shorter.

Projectile fragmentation

These processes cause a reduction of the primaries flux, which is defined as the number of particles traversing a certain area. The produced fragments are fast, with a mean velocity similar to the primary ion velocity and, since they have lower charge and mass, their range is longer compared to the beam particles (see Sec. 1.2.1). Therefore they generate a longitudinal tail in the dose deposition curve (Fig. 1.7), delivering an unwanted dose beyond the BP. They are distributed in a small angle in the forward direction, but the spread of the lighter fragments (protons and helium ions) enhance the lateral broadening of the beam.

However, target and projectile fragments are produced in the same process and differ only by the choice of the reference frame.

Nuclear fragmentations generate not only charged fragments but also neutrons, which can play a relevant role. In fact, they represent a potential hazard in terms of NTCP: since their mean free path is quite long, they can deposit a considerable dose far away from the tumor region, thus increasing the probability of developing secondary radioinduced

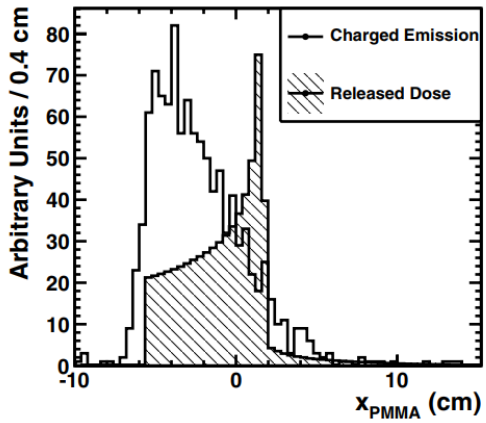

Fig. 1.19: Simulated depth-dose distribution (hatched) superimposed on the longitudinal profile, measured at $90°$ with respect to the beam direction (solid line), of charged secondary particles as a function of the penetration depth for a $220\,\mathrm{MeV/u}$ $^{12}\mathrm{C}$ impinging on a polymethyl methacrylate (PMMA) target (Piersanti et al. 2014).

malignacies.

In PT the interest in nuclear interactions is not only related to the study of the radiobiological effects of target fragments, but it is also prompted by the chance to exploit secondary particles to monitor the beam range inside the patient. These particles kinetic energy and emission angle spectra has been widely studied in the last years, in order to explore the possibility to develop beam range verification methods. The existing range monitoring techniques make use of different kinds of radiation:

- *Prompt-γ radiation*. Prompt photons are emitted in in the de-excitation processes associated to inelastic nuclear interactions. Prompt-γs are produced in an energy range between $1\,\mathrm{MeV}$ and $10\,\mathrm{MeV}$ and in a time of the order of $1\,\mathrm{ns}$. The delivered dose and the prompt-γs emission profile are in fact correlated: the ion range and the photon emission shape distal fall-off can be measured by means of Compton cameras and can be exploited for the range verification, via a comparison between measured and predicted distributions (Krimmer et al. 2015).

- *Annihilation-γs*. Nuclear processes can induce the production of β^+ emitters, which decay emitting a positron e^+ and an electronic neutrino ν_e. The positron has usually sufficient energy to travel few mm inside the patient body until it interacts with an atomic electron and annihilates, thus producing characteristic $511\,\mathrm{keV}$ back-to-back photons. These photons can be detected by *Positron Emission Tomography* (PET) scanners, which are usually ring-shaped detectors that can discriminate coincidence events occurring in the patient placed inside the ring. The emission profile of the detected photons can be correlated with the range (Enghardt et al. 2004).

- *Secondary charged particles*. Only particles from projectile fragmentation can travel

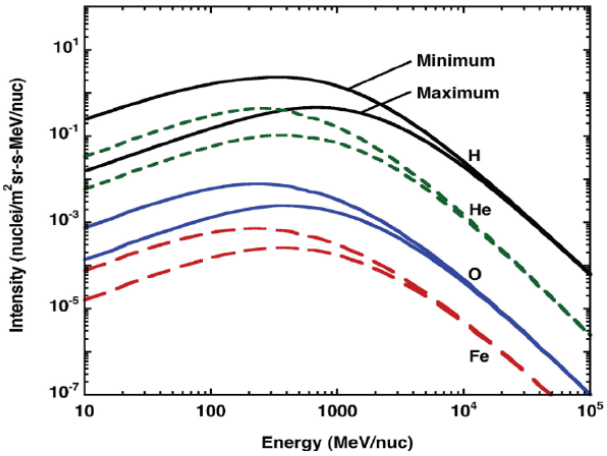

Fig. 1.20: Energy spectrum of common ions in the GCR during solar minimum and solar maximum.

further enough in the patient body and escape it to be finally revealed. They are mostly proton and, to a lesser extent, deuterons (5-10%). Also in this case the distal fall-off of secondaries emission profile is correlated with the BP position (Fig. 1.19). At present, an innovative detector based on scintillating fibers has been developed within the INSIDE (INnovative Solutions for In-beam DosimEtry in hadron therapy) collaboration and is now being tested in pre-clinical studies (Traini et al. 2017).

These techniques, would profit from experimental measurements of nuclear cross sections for the production of β-decaying nuclei and charged fragments, sine they would allow for accurate evaluation of the expected abundancy of particles that can be exploited to monitor the range.

1.4.2 Radioprotection in far from Earth space missions

Spacecrafts are exposed to a broad spectrum of high-energy and penetrating ionizing radiations, which can have harmful effects on vehicle electronic materials and astronauts. Especially, in future deep-space missions to near-Earth asteroids, the Moon and Mars the exposure time would be quite long and adequate shielding is therefore mandatory.

The main component of space radiation environment are:

1. *Solar Particles Events* (SPE), consisting mainly of protons and α-particles ejected from the Sun during solar flares events. The energy associated to solar cosmic rays can be very high, up to the order of GeV, and the radiation dose to astronauts can be potentially lethal. However, huge events are rare, and usually particles have much lower energy.

2. *Galactic Cosmic Rays* (GCR), consisting of protons and heavier nuclei emitted from supernovae within our galaxy. The energy spectrum is peaked in the MeV-GeV region, however the energy can reach very high values, up to ZeV (*i.e.* $10^{21}\,\mathrm{eV}$). GCR

fluxes are modulated by the interplanetary magnetic field and are anticorrelated with solar activity: the minimum fluxes occur when solar activity is highest and vice versa (Fig. 1.20).

3. *Geomagnetically trapped particles*, consisting of protons and electrons confined by the magnetic field of Earth. High-energy electrons ($\sim 100\,\mathrm{keV}$) are contained in the inner and outer belts, while high-energy ($\sim 100\,\mathrm{MeV}$) protons are restricted to the inner belt.

Earth is protected from the most energetic of these particles by the magnetosphere, which deflects the majority of them, and by the atmosphere, which absorbs the majority of particles that penetrate the Earth magnetic field. The latter shields also the International Space Station (ISS), which is in low-Earth orbit within the magnetosphere.

In long duration missions to far from Earth sites, as for example Mars, astronauts would remain into interplanetary space for a minimum of a year, unprotected by the Earth magnetosphere and atmosphere from space radiation. Moreover, Mars has no global magnetic field and its atmosphere is thinner than Earth's. In this scenario, the predominant radiation health hazard will come from GCRs, including a considerable component of heavy ions. Since GCRs are usually highly energetic, they can pass through the moderate shielding and reach the inside of the spacecraft. Even if heavy ions constitute only $\sim$1% of the GCR flux, in unshielded space they largely contribute to dose (up to $30-40\%$) due to their high LET and RBE values. While on Earth the mean equivalent dose[2] is approximately $0.1\,\mu\mathrm{Sv/d}$, it has been estimated that on the Mars surface the astronauts would be exposed to an average GCR dose-equivalent rate of $0.64\pm0.12\,\mathrm{mSv/d}$, that means a total of $320\pm50\,\mathrm{mSv}$ in a 500 days mission (Hassler et al. 2013).

The exposure to GCRs is unavoidable, however the heavy ion flux can be attenuated by shielding: the cosmic ray spectrum is modified when particles impinge on a medium, for example a spacecraft wall, due to the atomic and nuclear reactions that can induce fragmentation of heavier ions into lighter ions. Usually, since GCR are highly energetic, the multiplicity of the produced fragments can be large. As a result, the net physical dose inside the spaceship does not change significantly, however the biological dose is highly reduced, since secondary fragments have a lower LET and biological effectiveness. Furthermore, also the yield and energy distribution of secondary particles are needed for the risk assessment for space explorers: since they are more penetrating than heavy ion, they may constitute a serious hazard for the crew members. Hence, it is fundamental to know accurately the particle spectrum at which a space mission will be subject during its travel in the Solar System and the relative cross sections on the spaceship components, in order to design and optimize a suited shielding.

A semiempirical model describing the hadronic total reaction cross section σ_r is the Bradt–Peters law (Bradt & Peters 1950):

$$\sigma_r = \pi r_0^2 \left(A_P^{1/3} + A_T^{1/3} - b_0 \right)^2 \tag{1.22}$$

[2] The *equivalent dose*, measured in sievert (Sv), is derived from the absorbed dose, but also takes into account the biological effectiveness of the radiation depending on the radiation type and energy.

where A_P and A_T are the mass number of the projectile and the target nuclei respectively, b_0 is the overlap transparency parameter and $r_0 = 1.25\,\mathrm{fm}$ is the proportionality constant in the geometrical nuclear radius formula $r = r_0 A^{1/3}$. From this law, it is possible to retrieve that the cross section per unit target mass increases with decreasing A_T:

$$\frac{\sigma_r}{A_T} \propto A_T^{-1/3} \tag{1.23}$$

This means that light materials are more effective for shielding and liquid hydrogen has the maximum performance as shield material. However, hydrogen is not a practical choice because it should be a liquid kept at very low temperature. A more convenient choice would be an hydrogenated material, such as polyethylene.

Nowadays shielding studies are mostly conducted via MC transport codes. The prediction of the codes have some substantial differences, due to the different physics models used and to the lack of reliable cross sections for the fragmentation of several high energy ions on different materials (Durante & Cucinotta 2011). At present, in fact, there are gaps in the available cross section data relevant for space exploration which must be filled, therefore experimental campaigns aiming to retrieve the cross sections of p, He, C, O, Si and Fe ions on light targets ($Z \leq 13$) are needed. In particular, cross section on aluminum ($Z = 13$) target are of great interest to cosmic ray transport and space radiation shielding, since it is the typical material used for spacecraft structure.

1.5 Monte Carlo models for nuclear interactions

Calculation of inelastic scattering of protons and ions on atomic nuclei is, at present, a problem with no conclusive solution. Even though experimental data are abundant, they do not cover every possible energy, projectile and target combination. In this scenario, theoretical models are useful to interpret and interpolate the existing experimental data. However, there is no theory that does provide a general phenomenological model capable of calculating cross sections for nuclear reactions in any situation, but several models having different limitations and validity have been proposed.

MC codes make use of these models in simulating interactions and transport of particles. They are theory driven and data benchmarked, and allow for event-by-event description, with full correlations and exact energy conservation. Nuclear interactions are modeled starting from a sampling of the occurrence probability of a certain kind of interaction, which depends on the primary particle energy and is commonly based on experimental cross sections from nuclear database and parameterized physics models.

They are widely used in nuclear and particle physics to study and design new detectors, and also their employment in medical physics is quickly spreading: they are used for dose calculations, simulations of fluences and dose distributions in patient or patient-like geometries, shielding design, radioprotection studies and many other tasks. Usually, in PT they are not used for routine treatment planning calculations since they are quite time-consuming, but they are often employed for many applications in ion beam therapy, such as treatment plans check for a restricted number of particularly complicated cases. In fact, MC codes are more effective than analytical models used

Full MC	Analytical TPS	Fast MC (GPU based)
70 h/CPU	1 h/CPU	20 s/GPU

Tab. 1.1: Typical average CPU or GPU times for dose calculation by means of different simulation toolkits.

by TPS since they embed physics models validated and based on experimental data. In particular, they provide more accurate prediction of nuclear processes, which are commonly neglected or highly approximated by analytical models. To overcome the long time calculation required by MC codes, in the last years several *fast* MC codes have been developed. They are based on semi-analytical algorithms which often runs on *Graphics Processing Unit*s (GPUs) and allow to perform accurate dose calculation in a reasonable time for clinical use. Typical times for a treatment plan dose calculations are reported in Tab. 1.1.

MC codes are also used in the commissioning of the TPS in a certain facility: this procedure aims to check the ability of the TPS dose calculation algorithms to reproduce measured dose calculations. They are also fundamental to interpret the data in range monitoring applications.

Generally, MC codes used in PT were developed within scientific communities which have different needs in terms of interaction energy ranges and accuracy (high energy physics, radioprotection, *etc*.). Hence, the physics models implemented in MC codes have to be tested, in order to meet the accuracy requirements required for clinics application. It is essential to note that the uncertainties related to the nuclear models require constant benchmarking and validation work and upgrades.

.

1.5.1 Proton-nucleus interactions

The interaction of a proton on a target nucleus includes a series of nucleon-nucleon collisions, which result in the emission of secondary particles (protons, neutrons, light fragments), each of them originating from target fragmentation, and to equilibration of the remnant nucleus (Fig. 1.21 top). In MC codes, interactions are usually described in a three stage sequence (Battistoni et al. 2016a): generalized intra-nuclear cascade, *pre-equilibrium* and *de-excitation*. The time scale of the first two step is the one of strong interactions, $10^{-22} - 10^{-23}$ s, while for the last step the time of the process is $10^{-16} - 10^{-18}$ s.

Generalised *Intra-Nuclear Cascade* (INC). This model was first proposed by Serber (1947) and then implemented by Bertini (1963). Thanks to more recent developments, it can describe nuclear interactions in case of nucleons with energy ranging from above $50\,\mathrm{MeV}$ to about hundreds of GeV, and is successfully used in the MC simulations at intermediate energy region. In this model nuclear reactions of incident particles are described in terms of two-bodies collisions within the nucleus.

The condition of validity of this model is that De Broglie wavelength λ_B of the primary particle is much smaller than the average distance $\langle d \rangle$ between the nucleons in a

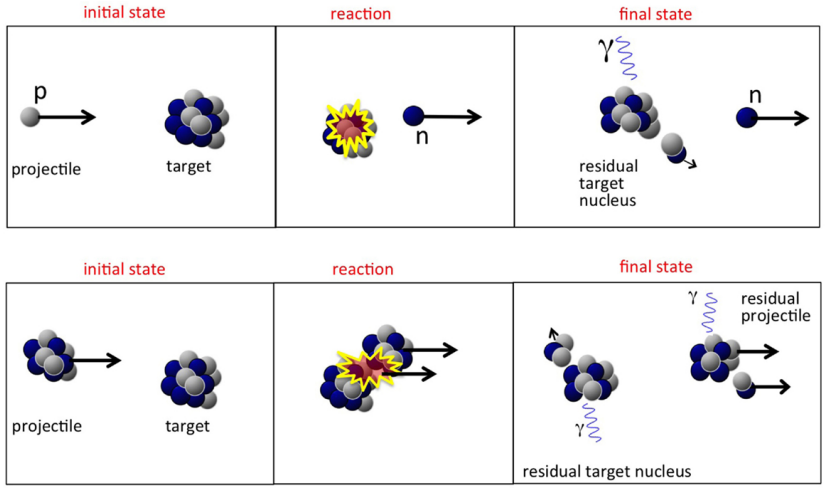

Fig. 1.21: Representation of a proton-nucleus interaction with production of a neutron (top) and of a nucleus-nucleus collision with emission of light fragments (Kraan 2015).

target nucleus:

$$\lambda_B = \frac{2\pi\hbar}{p} \ll \langle d \rangle = \sqrt[3]{\frac{3}{4\pi\rho_N}} \simeq 1\,\mathrm{fm} \tag{1.24}$$

where p is the particle momentum and ρ_N the intranuclear density ($\sim$0.17 nucleons/fm^3 at nucleus center). Therefore the interacting nucleon can be considered as a "quasi free" nucleon. For therapeutic energies, the validity of this model is not obvious, since the De Broglie wavelength of a $250\,\mathrm{MeV}$ proton is about $1\,\mathrm{fm}$, which is approximately of the same order of magnitude of $\langle d \rangle$. However, Bertini's model have been improved by introducing quantistic effects, like Pauli blocking, formation time, coherence length, nucleon antisymmetrization and hard core nucleon correlation. This modern version of INC works well also at intermediate energies. (Kraan 2015).

Another requirement is that the time between two subsequent collisions is longer than the time in which a single interaction takes place, so that each interaction can be considered independent of the others.

The reaction with the nucleus is calculated by determining the life history of each particle involved in the two-bodies collisions occurring within the nucleus. The point of collision, the type of collision, the momentum of the hit nucleon, and the scattering angles are obtained by statistical sampling techniques, and experimental data are used whenever cross-sections are required.

During the cascade, proton, neutrons and also light ions can be emitted. The latter, are produced through the *coalescence* mechanism: emitted nucleons which are close in phase space are grouped together.

Pre-equilibrium. This second stage starts when the energy of all the produced particles becomes lower than a certain threshold (generally $\sim$tens of MeV) but the residual

nucleus is not yet at thermal equilibrium. In MC codes it is usually modeled according to the *exciton model* (Griffin 1966; Blann 1983), a semi-classical model which explains the emission of high-energy particles in nuclear reactions. After the emission of protons, neutrons, and light fragments, the latter through coalescence process, the remnant nucleus reaches the equilibrium, with a certain excitation energy shared among the remaining nucleons.

De-excitation. Depending on the mass of the remnant nucleus and its excitation energy, the de-excitation step can follow different paths:

- *Nuclear evaporation*. Light fragments ($Z \leq 2$) escape from the excited residual nucleus, in a process that resembles the evaporation of a hot system.
- *Fission*. In this case the residual nucleus breaks into two separate fragments. However, since this process is relevant only for very heavy nuclei (usually $Z \geq 65$) that are not present in the human body (apart from medical implants or infinitesimal traces), fission is negligible to the purposes of this study.
- *Fermi break-up*. This process is relevant in radiotherapy since it concerns lighter ions ($A \leq 16$) which represent the majority of human body atoms. In this nuclei the excitation energy can exceed the binding energy of some fragmentation channels. This cause the break of the nucleus into lighter fragments.
- γ*-emission*. The excited nucleus can dissipate its residual energy by emitting photons.

1.5.2 Nucleus-nucleus interactions

Differently from proton-nucleus interaction, in nucleus-nucleus the projectile is not a "free" nucleon. Most models that describe these processes are variants of the abrasion-ablation model (Fig. 1.21 bottom). Also in this case the interaction can be subdivided in a fast stage ($10^{-22} - 10^{-23}$ s), the abrasion, and a slow stage ($10^{-16} - 10^{-18}$ s), the ablation. During the abrasion, target and projectile nuclei overlap in a reaction zone. In this stage a "quasi-projectile" and a "quasi-target" fragments are formed, together with other excited light fragments. The "quasi-projectile" and the "quasi-target" fragments have very different velocities, the first being similar to the velocity of the primary particle, while the other being almost at rest. Finally, during the ablation, the excited residual target, projectile and other fragments emit again light fragments via isotropic evaporation and reach equilibrium.

The fast stage is described by different models, differing mainly in the description of the nuclear field influencing the propagation of the particles in the nucleus. The most used models, which are valid in a wide range of situations, are:

INC. This model is used for ions with energy up to about $100\,\mathrm{MeV/u}$, and it is similar to the model described for protons. The highly excited nuclei loose energy through a series of two-body reactions and scattering off "quasi-free" nucleons. Several nucleon-nucleus interaction can take place in a single nucleus-nucleus collision.

Element	Mass fraction (%)	Atomic fraction (%)
Oxygen	65	24
Carbon	18	12
Hydrogen	10	62
Nitrogen	3	1.1
Calcium	1.4	0.2
Phosphorus	1.1	0.2
Others	1.5	0.5

Tab. 1.2: Human body elemental composition in percentage.

***Quantum Molecular Dynamics* (QMD).** This model is valid for energies ranging from $\sim$50 to $\sim 400\,\mathrm{MeV/u}$. Each nucleon is represented by a gaussian wave packet, and the collision involves every nucleon belonging to the projectile or target nuclei. To describe the emission of secondary particles, this model minimizes the Hamiltonian representing nucleon-nucleon collisions.

***Boltzmann-Master Equation* (BME).** For energies below $100\,\mathrm{MeV/u}$, this model simulates the pre-equilibrium stage, describing the thermalization of composite nuclei down to the evaporation/fission/breakup stage through a series of two- body interactions and the release of neutrons and protons.

The slow stage, instead, can be described by the same models discussed for proton-nucleus interactions: evaporation, fission, Fermi-breakup, and gamma emission.

1.6 Experimental cross sections

Experimental cross sections of PT and space radioprotection interest can be found in several works in literature. However, as explained is Sec. 1.5, the spectrum of possible combination of targets, beam particles and energies in quite large, and the experimental measurements do not adequately and fully cover it. This is why nuclear models are used when experimental data are not available.

In Sec. 1.4 the beam ion species of interest have been presented: H, He, C, O at energies up to $400\,\mathrm{MeV/u}$ for PT, the same but also at higher energies for radioprotection in space plus Si and Fe beams. For what concerns the targets, the most important nuclei for medical applications are the most abundant in the human body. A list of these elements is reported in Tab. 1.2. Considering the mass fraction, carbon, oxygen and hydrogen are the most common nuclei that can be found in body tissues. Also calcium can be relevant when bones are concerned.

1.6.1 Proton-nucleus interactions

A review of the available interaction cross sections of protons on carbon, oxygen and calcium can be found in a work by Braunn et al. (2015), where the authors compared the experimental data drawn from the EXFOR[3] and Landolt-Börnstein databases (Iljinov

[3] https://www-nds.iaea.org/exfor/exfor.htm

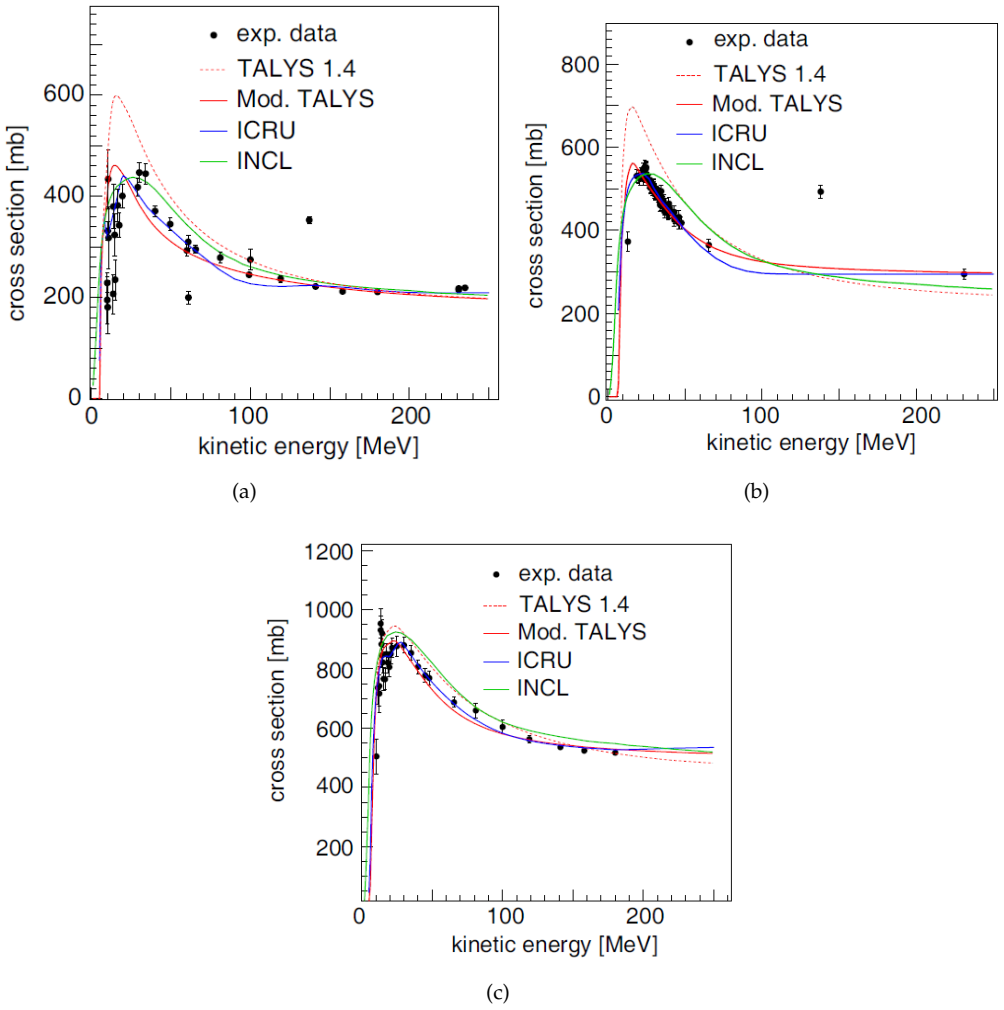

Fig. 1.22: Reaction cross sections for the p+^{12}C (a), p+^{16}O (b) and p+^{40}Ca (c). Experimental data (black dots) are compared to the prediction of different models: two different versions of the TALYS code (Koning et al. 2007), the ICRU63 evaluation (ICRU 2000) and the INCL coupled to the ABLA07 de-excitation code (Boudard et al. 2013; Kelic et al. 2009)

et al. 1991), to the prediction of different models. These data include measurements of reaction cross sections (Fig. 1.22) and isotopic production cross sections (Fig. 1.23-1.24). As depicted in the figures, the prediction differences between the models confirm that they are not able to reproduce the experimental data with the accuracy required for space and therapy applications. In particular, the discrepancies for isotopic production cross sections are more pronounced at high energies, where the databases are less populated.

It is important to note that the energy-differential cross sections for each produced fragment are missing. The knowledge of fragments energy, however, is of paramount importance since it affects the range inside the tissues.

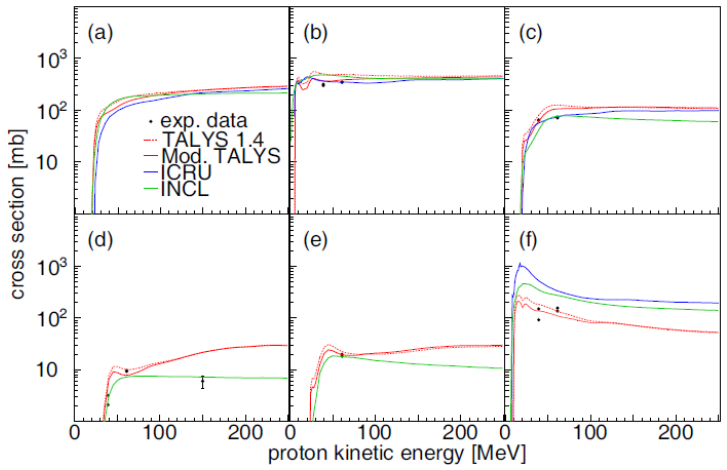

Fig. 1.23: Production cross sections of (a) neutrons, (b) protons, (c) deuterons, (d) tritons, (e) ^{3}He and (f) ^{4}He from the p+^{12}C reaction. Line colors and symbols have the same meaning as in Fig. 1.22.

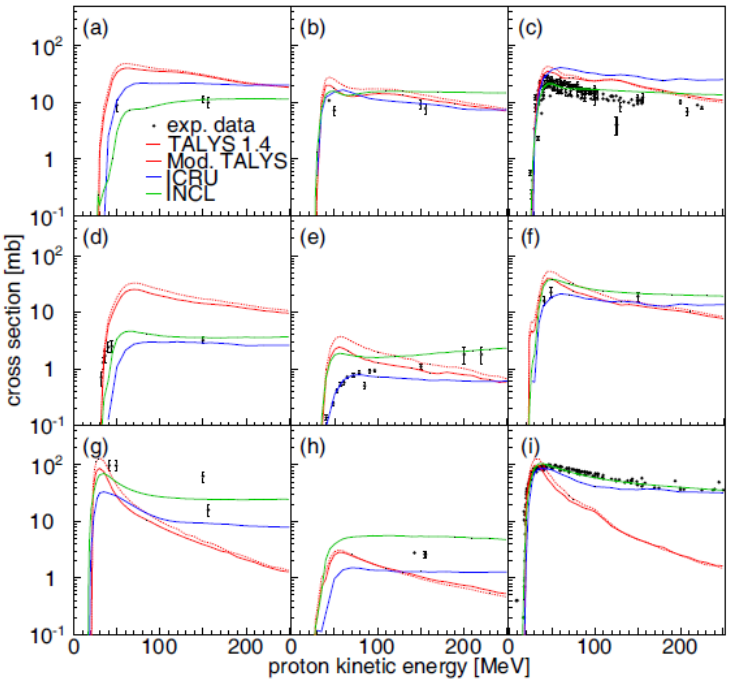

Fig. 1.24: Production cross sections of (a) ^{6}Li, (b) ^{7}Li, (c) ^{7}Be, (d) ^{9}Be, (e) ^{10}Be, (f) ^{10}B, (g) ^{11}B, (h) ^{10}C and (i) ^{11}C from the p+^{12}C reaction. Line colors and symbols have the same meaning as in Fig. 1.22.

1.6.2 Helium-, carbon- and oxygen-nucleus interactions

In the last years, due to the growing interest on ion beams for cancer treatments several experiments have been carried out to study helium, carbon and oxygen ion beam fragmentation. However, only few beam energies have been explored.

In a work by Gunzert-Marx et al. (2008), the production yields, energy spectra and angular distributions of H and He isotopes from $^{12}\mathrm{C}$ have been studied for a $200\,\mathrm{MeV/u}$ on a water target at the GSI. At GANIL, France, the double differential cross sections and the angular distributions of secondary fragments produced by a $95\,\mathrm{MeV/u}$ $^{12}\mathrm{C}$ beam on thin targets (C, CH_2, Al, Al_2O_3, Ti and PMMA) have been measured by Dudouet et al. (2013) (Fig. 1.25). The Fragmentation of Ions Relevant for Space and Therapy (FIRST) experiment (Toppi et al. 2015) at GSI studied the nuclear interactions of a $400\,\mathrm{MeV/u}$ $^{12}\mathrm{C}$ ion beam on C and Au thin targets by measuring the differential cross sections.

Recent experiments have provided some initial data about $^{4}\mathrm{He}$ fragmentation in PMMA targets. In a work by Marafini et al. (2017), the fluxes and energy spectra of H and He isotopes were measured at HIT for $102\,\mathrm{MeV/u}$, $125\,\mathrm{MeV/u}$ and $145\,\mathrm{MeV/u}$ He beams (Fig. 1.26). A similar work by Rovituso et al. (2017) measured the angular distribution and kinetic energy spectra of $^{4}\mathrm{He}$ secondary fragments, with primary energies of $120\,\mathrm{MeV/u}$ and $200\,\mathrm{MeV/u}$.

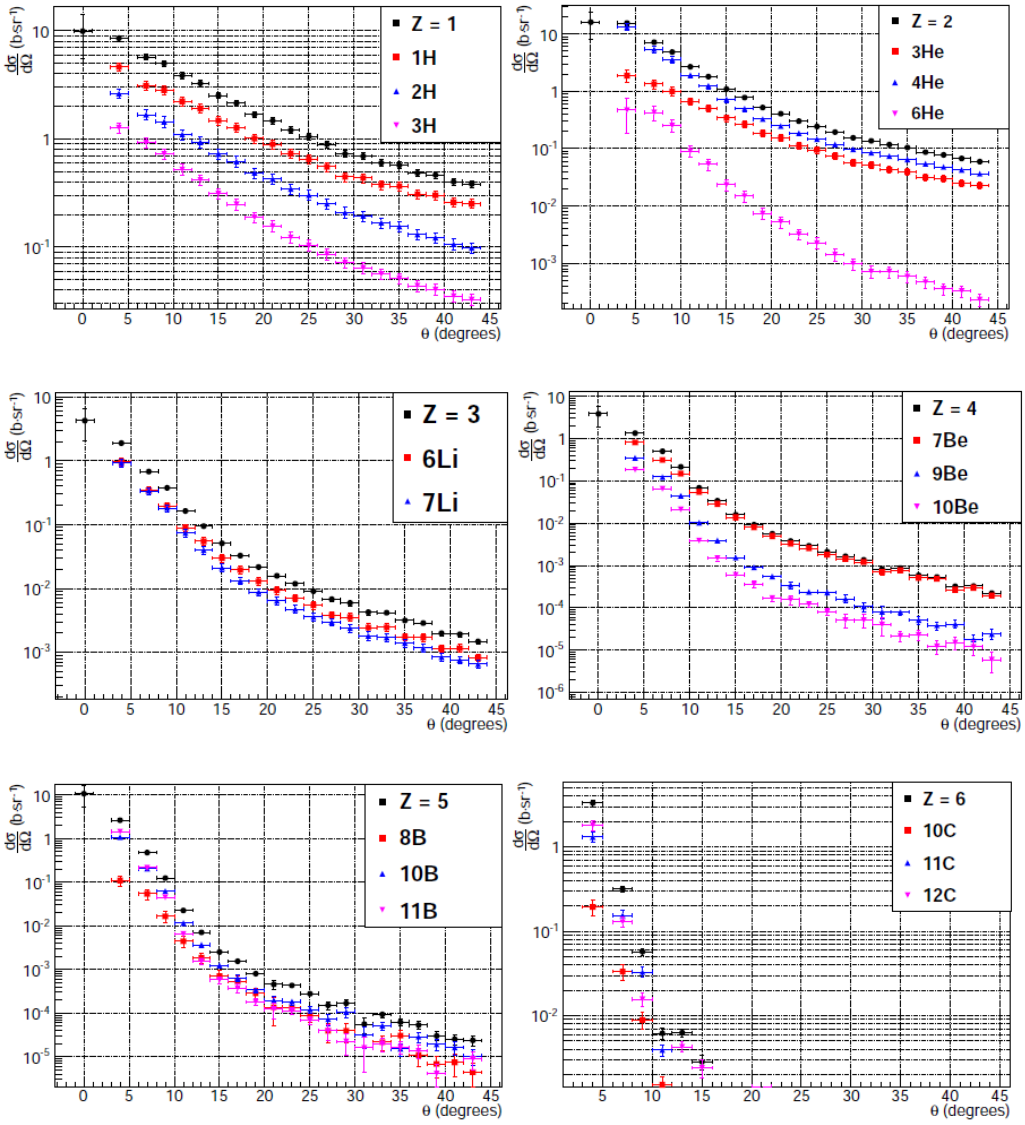

Fig. 1.25: Angular distributions for different fragments resulting from the ^{12}C fragmentation on carbon target (Dudouet et al. 2013).

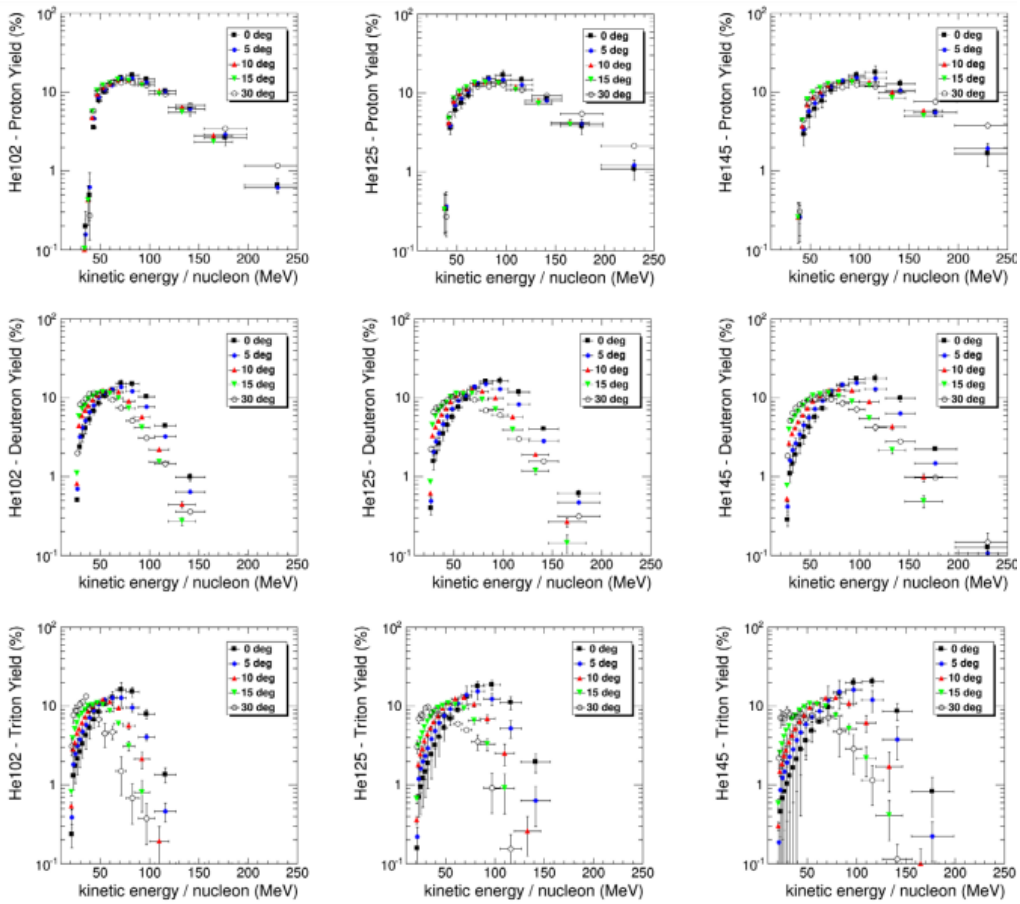

Fig. 1.26: Relative yield of ^{1}H (top), ^{2}H (center), and ^{3}H (bottom) as a function of nucleon kinetic energy measured at different angles for $102\,\mathrm{MeV/u}$ (left), $125\,\mathrm{MeV/u}$ (center) and $145\,\mathrm{MeV/u}$ (right) ^{4}He beams (Marafini et al. 2017).

CHAPTER 2

The FOOT experiment

The FragmentatiOn Of Target (FOOT) project is an applied nuclear physics experiment aiming to measure the fragmentation cross sections of relevance for PT and radioprotection in space. These cross sections are fundamental to improve the PT treatment plans quality, to study the shielding material performances and to benchmark nuclear interaction models. The experiment has been approved and funded by Italian National Institute for Nuclear Physics (INFN) and, today it counts more than 90 members in its collaboration. The involved institutions include eleven INFN sections and laboratories, ten Italian universities, three foreign universities and three other research institutions.

The experiment project includes the development of two different experimental setups: an electronic detector setup to measure heavier fragments and an emulsion spectrometer for the lighter ones. The first data taking is scheduled for April 2019 with the emulsions and in the next years with the other setup, since the research and development of its components are still ongoing.

In this chapter, a comprehensive overview of the FOOT experiment is given. In Sec 2.1 motivations and goals of the experiment are presented, as well as the research program. In Sec. 2.2 the strategy conceived to overcome some experimental issues in proton-nucleus interaction study is reported. The preliminary studies that drove the development of two experimental setups are then introduced in Sec. 2.3. Particular attention is devoted in Sec. 2.4 to the electronic detector setup, since its simulations and performances analysis are the main subject of this thesis (see Chap. 3 and Chap. 4 respectively). Finally, the emulsion cloud chamber setup is described in Sec. 2.5.

2.1 Motivations, aims and research program

As seen in Sec. 1.4, accurate measurements of fragments spectra are of great importance both to improve the treatment planning quality in PT and to estimate the astronauts dose exposure in far from Earth missions in order to design proper shielding systems. Since in the energy range of interest the fragmentation processes have not been completely covered by experimental measurements, at present the only possibility is to rely on nuclear models (see Sec. 1.5), which however are not exact calculable theories and therefore suffer from many uncertainties.

The FOOT purpose is to experimentally measure nuclear fragmentation cross sections relevant in PT and space radioprotection. Since the most strict requirements come

from the PT, the accuracy of these measurements is dictated by the needs of PT radiobiologists, who will implement the cross sections in the kernel of the codes used in treatment planning to achieve sound NTCP models. The FOOT main goal is to measure the fragment production cross sections with maximum uncertainty of 5%. Since fragments charge and energy are the quantities that mostly affect fragments biological efficacy, FOOT aims to perform the charge identification (ID) with an accuracy of 2-3% and measure the fragments energy spectra with an energy resolution of about 1-2 $\mathrm{MeV/u}$. Also the mass has a significant role since it influences the fragments range, therefore the isotopic ID accuracy have to reach the level of about 5%. The angular emission spectrum, instead, is not essential at least for what concerns p→X interactions, because target fragments have a very short range and would approximately deposit all their energy locally.

FOOT aims to measure the production yield and energy of fragments generated by $^{12}\mathrm{C}$ beams in the therapeutic energy range, in order to fill the gaps in experimental measurements data and provide a wider set of experimental data to benchmark nuclear models and improve the PT treatments quality. Nuclear fragmentation channels will also be explored for $^{16}\mathrm{O}$ and $^{4}\mathrm{He}$ beams, which are increasingly considered in PT as promising alternatives to protons and carbon ions. Once the nuclear cross sections database will be sufficiently populated, it will be possible to benchmark and match the MC nuclear models to the experimental data. In this way, the cross sections at beam energy not explored by experimental measurements can be predicted and extrapolated by means of this new data-tuned version of MC.

The most challenging goal of the FOOT experiment is the characterization of target fragmentation processes induced by proton beams, which are particularly relevant in protontherapy. Since target fragments produced by a few hundreds of MeV proton beam have a very short range (see Sec. 1.4.1), their detection is extremely tough. In Sec. 2.2 the procedure that will be adopted to overcome this difficulty is described in details.

Along with the investigation of nuclear fragmentation of therapeutic beams, another FOOT purpose is to measure fragmentation cross sections for beams at higher energies. FOOT will explore helium, carbon and oxygen beams fragmentation processes at $700\,\mathrm{MeV/u}$, since these high energy nuclei are commonly present in the GCR spectrum (see Sec. 1.4.2).

FOOT has been designed to be a fixed target experiment: the beams of interest, in the energy range previous reported, will impinge on a target representative of the human tissue and the fragments will be detected and measured. The targets composition has been set according to the human body composition: carbon, oxygen and hydrogen have been selected as the main target of interest.

The choice of a pure gaseous hydrogen target have been discarded, since it would imply many technical difficulties, from the low interaction rate due to the low density, to the impossibility, due to safety reasons, of handling such a target in the therapy centers where the experiment will be run. To avoid all this kind of issues, a different approach has been proposed: the measurements will be performed with two different targets, one made of carbon, whose cross sections are also of interest, and the other made of an hydrogen enriched compound, such as polyethylene (C_2H_4). The cross sections on

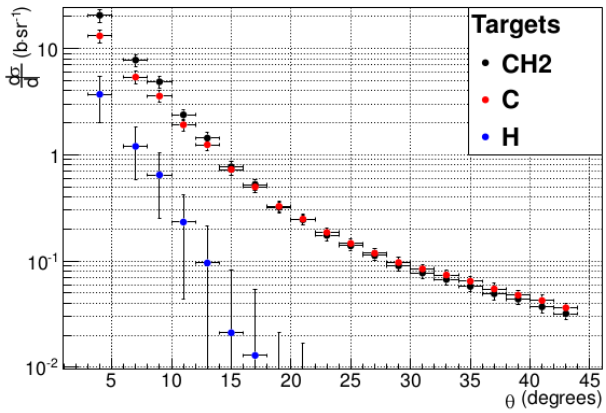

Fig. 2.1: Combination of the carbon and polyethylene angular distribution to determine the hydrogen angular distribution for alpha fragments (Dudouet et al. 2013).

hydrogen will be retrieved by subtracting the data obtained with the two targets:

$$\sigma(\mathrm{H}) = \frac{1}{4}\left(\sigma(\mathrm{C_2H_4}) - 2\,\sigma(\mathrm{C})\right) \tag{2.1}$$

The same procedure is also valid for differential cross sections:

$$\frac{\mathrm{d}\sigma}{\mathrm{d}E}(\mathrm{H}) = \frac{1}{4}\left(\frac{\mathrm{d}\sigma}{\mathrm{d}E}(\mathrm{C_2H_4}) - 2\,\frac{\mathrm{d}\sigma}{\mathrm{d}E}(\mathrm{C})\right) \tag{2.2}$$

$$\frac{\mathrm{d}\sigma}{\mathrm{d}\Omega}(\mathrm{H}) = \frac{1}{4}\left(\frac{\mathrm{d}\sigma}{\mathrm{d}\Omega}(\mathrm{C_2H_4}) - 2\,\frac{\mathrm{d}\sigma}{\mathrm{d}\Omega}(\mathrm{C})\right) \tag{2.3}$$

This method has been successfully adopted in a cross sections study by Dudouet et al. (2013), as reported in Fig 2.1. A disadvantage of this strategy, however, is that the resulting cross section uncertainties are the quadratic sum of the uncertainties of the two single targets, therefore the cross sections on hydrogen have a larger error.

The same approach can be adopted to study the cross sections on oxygen target. In this case, a PMMA target have been selected, since PMMA is composed of carbon, hydrogen and oxygen.

A complete overview of the FOOT research program, including beams, targets and energies that will be investigated, is listed in Tab. 2.1.

The European facilities that can provide the cited beam particles and energies are:

- the CNAO, in Pavia, Italy, where ^{12}C beams at therapeutic energies are available. An experimental hall dedicated to research studies is under construction and helium and oxygen sources may be available in the future.

- the HIT center, in Heidelberg, Germany, where ^{4}He, ^{12}C and ^{16}O beams at therapeutic energies are available. The experimental room is routinely used for several research studies.

Physics	Beam	Target	Energy (MeV/u)	Kinematic approach	Facilities
Target fragm. in PT	^{12}C	C, C_2H_4	200	inverse	CNAO, HIT, GSI
Target fragm. in PT	^{16}O	C, C_2H_4	200	inverse	HIT, GSI
Beam fragm. in PT	^{4}He	C, C_2H_4, PMMA	250	direct	HIT, GSI
Beam fragm. in PT	^{12}C	C, C_2H_4, PMMA	350	direct	CNAO, HIT, GSI
Beam fragm. in PT	^{16}O	C, C_2H_4, PMMA	400	direct	HIT, GSI
Space Radioprotection	^{4}He	C, C_2H_4, PMMA	700	direct	GSI
Space Radioprotection	^{12}C	C, C_2H_4, PMMA	700	direct	GSI
Space Radioprotection	^{16}O	C, C_2H_4, PMMA	700	direct	GSI

Tab. 2.1: Overview of the FOOT research program. In the last column, also the facilities providing the beams are reported.

- the GSI, that has a quite large experimental cave and provides $^{4}\mathrm{He}$, $^{12}\mathrm{C}$ and $^{16}\mathrm{O}$ (and other ion species) also at higher energies in the range of interest for space radioprotection.

2.2 Inverse kinematic approach

As reported in Sec. 1.4.1, due to kinematic reasons, target fragments originating from proton-tissue (p→X) interactions have a very low energy and short range. These fragments can travel only few tens or hundreds of $\mu\mathrm{m}$ from the emission point (Fig. 1.17a), hence even with a relatively thin target ($\sim\mathrm{mm}$) they would stop inside it, releasing all the energy within the target and invalidating any detection attempt. On the other hand, an even thinner target ($\sim\mu\mathrm{m}$) implies other kind of issues: mechanical problems would arise since it is difficult to handle such a fragile target without risking any damage to it and, most of all, the interaction rate would be extremely depressed, so the beam time required to collect a sufficient amount of data would become excessively long.

To overcome this issue, an alternative solution has been proposed to study target fragments: an *inverse kinematics* approach. The basic idea is to switch the projectile and target role: instead of shooting a proton beam onto a tissue-like (carbon or oxygen) target, tissue-like nuclei will be accelerated to impinge on a proton target. If the kinetic energy per nucleon is kept the same, this transformation results only in a reference frame change, from what can be called "patient reference frame" to a new one, that will be our "laboratory frame". In this way, fragments originated from a carbon or oxygen beam, with the same kinetic energy per nucleon that would have a proton beam, are emitted with higher energy. The consequent rise of the mean range ensures an easier detection and reconstruction of the event kinematics, but also the use of a thicker target, with a consequent increase of the interaction rate.

To switch to the patient frame and obtain the nuclear cross section of proton onto oxygen or carbon, the Lorentz transformations must be applied in order to convert the coordinates between two different and inertial reference frames. If we consider, that the beam direction is towards the positive part the z-axis, two reference frame can be identified: the laboratory frame S, where the proton target is at rest and the ion beam

is moving along z at a constant velocity β towards the target, and the patient frame S', where the ion is at rest while the proton is moving along z with the same velocity β but in the opposite direction. The 4-momentum of the ion in S and the 4-momentum of the proton in S' are $\mathbf{P} = (E/c, \boldsymbol{p})$ and $\mathbf{P'} = (E'/c, \boldsymbol{p'})$ respectively, where E and E' are the energies. In this configuration, the proton 4-momentum components in the S' frame are given by:

$$\frac{E'}{c} = \gamma \left(\frac{E}{c} - \beta p_z \right) \tag{2.4}$$

$$p'_x = p_x \tag{2.5}$$

$$p'_y = p_y \tag{2.6}$$

$$p'_z = \gamma \left(-\beta \frac{E}{c} + p_z \right) \tag{2.7}$$

These equations can be written also in matrix format:

$$\mathbf{P'} = \mathbf{\Lambda}\, \mathbf{P} \tag{2.8}$$

where $\mathbf{\Lambda}$ is a 4×4 matrix as follows:

$$\begin{pmatrix} E'/c \\ p'_x \\ p'_y \\ p'_z \end{pmatrix} = \begin{pmatrix} \gamma & 0 & 0 & -\beta\gamma \\ 0 & 1 & 1 & 0 \\ 0 & 0 & 1 & 0 \\ -\beta\gamma & 0 & 0 & \gamma \end{pmatrix} \begin{pmatrix} E/c \\ p_x \\ p_y \\ p_z \end{pmatrix} = \begin{pmatrix} \gamma\, E/c - \beta\gamma p_z \\ p_x \\ p_y \\ -\beta\gamma\, E/c + p_z \end{pmatrix} \tag{2.9}$$

The inverse Lorentz transformation is

$$\mathbf{P} = \mathbf{\Lambda^{-1}}\, \mathbf{P'} \tag{2.10}$$

where the inverse matrix $\mathbf{\Lambda^{-1}}$ is

$$\mathbf{\Lambda^{-1}} = \begin{pmatrix} \gamma & 0 & 0 & \beta\gamma \\ 0 & 1 & 1 & 0 \\ 0 & 0 & 1 & 0 \\ \beta\gamma & 0 & 0 & \gamma \end{pmatrix} \tag{2.11}$$

therefore $\mathbf{\Lambda^{-1}}$ is simply equal to $\mathbf{\Lambda}$ with a change of the β sign:

$$\mathbf{\Lambda^{-1}}(\beta) = \mathbf{\Lambda}(-\beta) \tag{2.12}$$

Even if the fragments angular emission distribution is not essential in proton-nucleon interactions, as seen in Sec. 2.1, the inverse kinematics strategy requires an emission angle measurement with a resolution of the order of few mrad in order to correctly apply the Lorentz boost. Therefore, both the projectile and fragments directions have to be measured accurately, and also the MCS of any particle inside the beam must be kept well below the mrad. This strongly limits the allowed thickness of the target. Moreover, the target thickness density should be of the order of $\mathrm{g\,cm^{-2}}$ or less, in order to minimize the probability of secondary fragmentation within the target. A reasonable target thickness is 2-$4\,\mathrm{mm}$, which is a good trade-off between the interaction rate and the required angular resolution.

2.3 Preliminary studies

The FOOT experimental setup has been designed, and is still being optimized, to perform the experimental measurements with the resolutions required by the radiobiology desiderata reported in Sec. 2.1. Since the measurements will be performed in different European facilities, the portability of the entire detector setup is a relevant parameter that has to be considered. The experimental setup has to be compact and "table top" in order to be easily movable, and has to fit the different experimental and treatment rooms where the beams of interest are available. The use of a magnetic spectrometer composed by a permanent magnet and high precision tracking detectors is a suitable option in this context.

Even though MC codes are not yet enough reliable, preliminary MC simulations have been performed with FLUKA (Ferrari et al. 2005; Böhlen et al. 2010) to drive the detector design (see Chap. 3). As well as the electromagnetic physical processes, FLUKA takes into account also hadronic interactions and in this work, and in general in the FOOT project, it has been preferred to other MC codes because it has been successfully applied to simulation of proton and ion beams in PT applications. Via MC simulations, the fragments production has been evaluated in terms of angular and energy distribution (Fig. 2.2). The kinetic energy per unit mass distribution of fragments produced by a $200\,\mathrm{MeV/u}$ ^{16}O ion beam impinging on a $2\,\mathrm{mm}$ thick polyethylene target is depicted in Fig. 2.2a: except for protons, characterized by an extremely broad spectrum, fragments distributions are peaked at a value corresponding to the beam energy. The rise at very low energy is due to target fragments. In fact it is more relevant for light ions which, being the kinetic energy per nucleon the same, have a range sufficiently long to escape from the target. For what concerns the fragments angular spectrum, as expected the distribution narrows as the charge and mass increase, so the fragments are mostly forward peaked (Fig. 2.2b). Fragments with $Z \geq 3$ are mainly confined in a $10°$ angle with respect to the beam direction.

Due to the large angular aperture of the lighter fragments, the required size, weight and cost of the magnetic spectrometer would be unfeasible. This consideration has led to the decision to develop two different experimental setups:

- a setup based on electronic detectors and a magnetic spectrometer optimized for heavy fragments ($3 \leq Z$)
- an emulsion chamber spectrometer optimized for light fragments ($Z \leq 3$) measurements

The data that will be obtained for lithium ($Z = 3$) ions will serve as link between the measurements achieved with the two experimental setups.

2.4 Electronic detector setup

The FOOT electronic setup aims to experimentally measure the production cross section for the heavier fragments ($Z \geq 3$). The fragments mass ID is performed combining the measurements of the particles momentum, kinetic energy and the time of flight. The

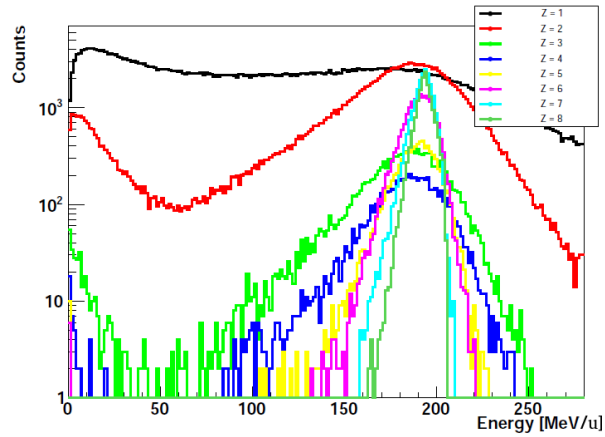

(a)

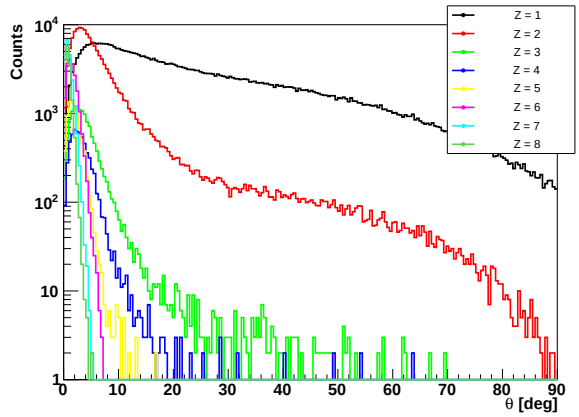

(b)

Fig. 2.2: Emission angle (with respect to the beam direction) distribution (a) and energy distribution (b) of fragments exiting the target in case of a $200\,\mathrm{MeV/u}$ $^{16}\mathrm{O}$ ion beam impinging on a $2\,\mathrm{mm}$ thick polyethylene target.

charge ID, instead, relies on the evaluation of the energy loss ΔE and of the time of flight, from which it is possible to obtain β, according to Eq. 1.5. Further details about the mass- and charge ID will be given in Chap.4.

The setup includes several detectors (Fig. 2.3), whose characteristics are summarized in Tab. 2.2 and then extensively reported in this Section. The setup size has been established as a trade-off between the geometrical acceptance, the portability and the cost: the request of the largest possible acceptance is in fact limited by the cost, the ease of transport and the space available in the experimental areas of the selected facilities. Longitudinally, the whole setup can be contained in about $1.5\,\mathrm{m}$ (Fig. 2.3).

Several detectors included in the electronic setup have already been tested. Most of

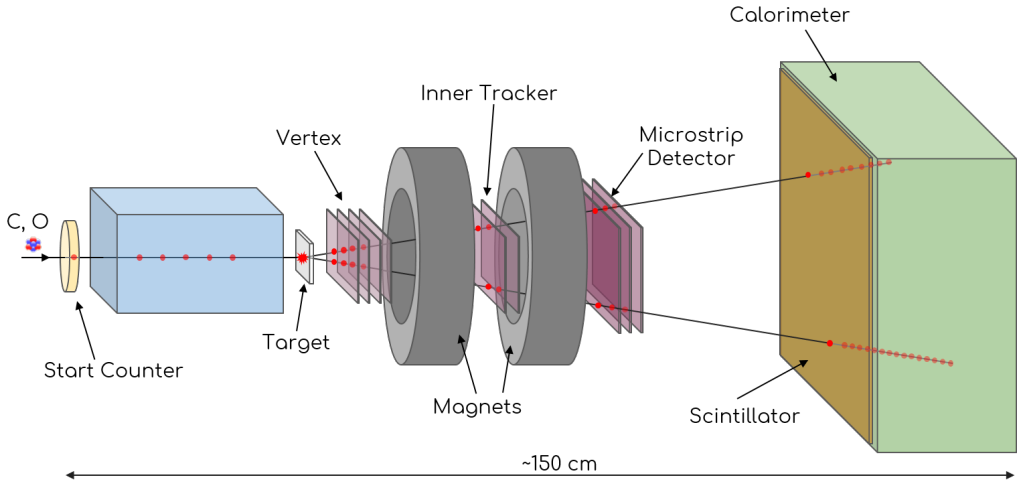

Fig. 2.3: Sketch of the FOOT electronic setup (not in scale).

Detector	Main characteristics
Start counter	plastic scintillator, 250 µm thick
Beam monitor	Ar/CO_2 drift chamber, 12 layers of wires
Vertex	4 layers of pixel silicon chips, 50 µm thick, $\sim 2\,cm \times 2\,cm$ area
Inner tracker	2 layers of pixel silicon chips, 50 µm thick, $\sim 8\,cm \times 8\,cm$ area
Microstrip detector	3 layers of silicon microstrips, $\sim 9\,cm \times 9\,cm$ area
Scintillator	2 layers of orthogonal 20 bars $2\,cm \times 40\,cm \times 0.3\,cm$ each
Calorimeter	288 bismuth germanate crystals, 24 cm long

Table 2.2: Main characteristics of the detectors included in the electronic setup.

the experimental tests have been carried out at CNAO, at Trento protontherapy center and also at LNS.

Three different regions can be identified in the setup: the *pre-target region*, the *magnetic spectrometer* and the *downstream region*.

2.4.1 Pre-target region

The detectors in this region are designed to monitor the primary beam and are a plastic scintillator and a drift chamber.

Start Counter

The Start Counter (STC) is a thin plastic scintillator layer placed about 30 cm before the target that monitors the primary particles rate and gives the trigger signal for event acquisition. It counts the number of primary particles and provides the event initial time. Moreover, in combination with another scintillator detector placed downstream the target, it provides the time of flight measurement.

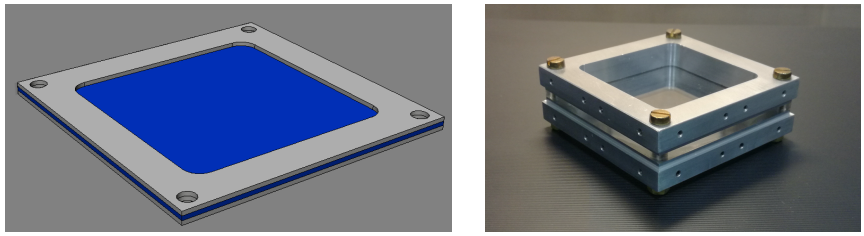

(a) (b)

Fig. 2.4: (a) Technical drawing of the STC and (b) photo of its mechanical frame.

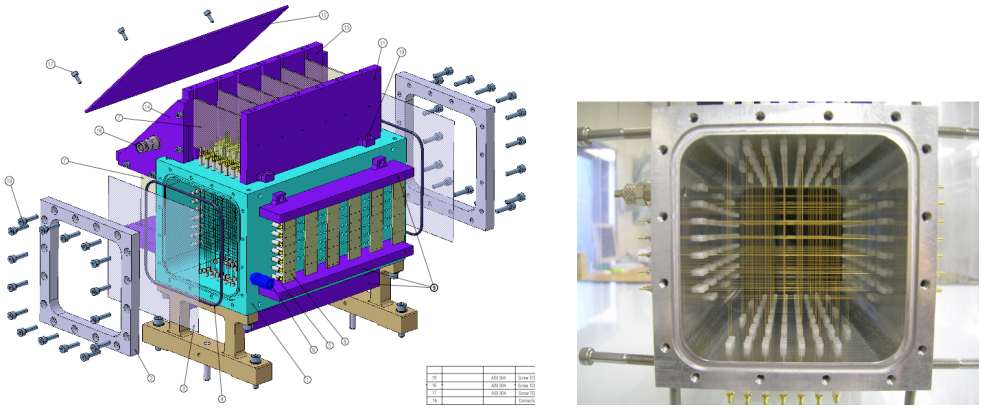

(a) (b)

Fig. 2.5: (a) Technical drawing and (b) photo of the inside of the BMN.

The STC is a foil of EJ-204 plastic, characterized by a rise time of $700\,\mathrm{ps}$ and a light yield of 10000ph/MeV (Fig. 2.4a). The four channels will be read-out by 48 Silicon Photomultipliers (SiPMs), 12 per side. The transversal dimensions are about $5\,\mathrm{cm} \times 5\,\mathrm{cm}$. The thickness, instead, is still matter of study, as it should be a compromise between the maximization of the light output and the minimization of the probability of fragmentation within the detector. A reasonable thickness value ranges between $250\,\mu\mathrm{m}$ and $1\,\mathrm{mm}$. A dedicated mechanical frame have been recently produced (Fig. 2.4b)

Since the measurement of the time of flight is crucial to achieve the desired mass ID resolution, the STC time resolution has to match the time resolution of the other scintillator detector. Therefore STC aims for a time resolution of about 30-$40\,\mathrm{ps}$ for the incoming beam particles (C and O). A $250\,\mu\mathrm{m}$ prototype has been tested with carbon ion beams at CNAO in July, the results will be available in the next months.

Beam Monitor

The Beam Monitor (BMN) is a Ar/CO_2 80/20% drift chamber (Fig. 2.5a and 2.5b) placed between the STC and target. It was built for the FIRST experiment (Abou-Haidar et al. 2012), and is composed by 12 planes of alternated horizontal and vertical wires. Each

plane has 3 rectangular cells ($16\,\mathrm{mm}\times10\,\mathrm{mm}$) with the long side perpendicular to the beam direction. The total dimensions are $11\,\mathrm{cm} \times 11\,\mathrm{cm} \times 21\,\mathrm{cm}$. The choice of a drift chamber detector relies on its low density material in order to minimize the MCS the production of fragments within the detector.

The BMN is equipped with a front-end electronic which preamplifies the signals that are then digitized by a time to digital converter (TDC). While the primary beam energy will be accurately known, each primary particle position is associated with an uncertainty due to the intrinsic beam lateral spread (usually $< \mathrm{mm}$). Since the primary 4-momentum is required to perform the Lorentz boost, the position and the direction of primary particles will be measured by the BMN. The achievable resolution is about 150-200 $\mu\mathrm{m}$ for position measurements, $\sim\mathrm{mrad}$ for angular measurements. Dedicated electronics will be able to detect also multi-track events, in order to reject the events in which the primary ion has fragmented in the STC. The tracks inside the cells will be reconstructed via dedicated Kalman filter algorithm.

The first experimental test will be run with proton beams in December 2018 at Trento protontherapy center, in order to calibrate the single-cell space-time relations and asses the single cells efficiency and the spatial resolution.

2.4.2 Magnetic spectrometer

The magnetic spectrometer includes two pixel detectors, a microstrip detector and a permanent magnet system that provides the required magnetic field. It is designed to measure the fragments momentum. Currently, a suitable mechanics is being developed

Permanent Magnet

The magnetic field will be provided by two Permanent Magnets (PMs) in *Halbach configuration* (Fig. 2.6): in each of them twelve blocks of magnets are arranged in a annular configuration. An external aluminum case will preserve the blocks arrangement. The choice of the material composing the PM blocks has been driven by considerations about the radiation resistance: in fact, in the FOOT setup the PMs will be severely exposed to various radiations, in particular neutrons and light ions (mainly protons and He ions). Radiation exposure can degrade an damage the PM material, thus altering the produced field. Recent studies (Simos et al. 2018) about the demagnetization of different PMs materials proved that Sm_2Co_{17} is particularly insensitive to radiation exposure compared to other PM materials. Therefore, the choice of the material for the FOOT PMs has fallen upon Sm_2Co_{17}.

The Halbach configuration produces an approximately uniform field in the internal hole, as represented in Fig. 2.7a: the field obtained is comparable to the one achievable with a dipole magnet. In the FOOT case, considering the axis of the magnets coincident to z-axis as in Fig. 2.6, the y component of the magnetic field, B_y, is significantly higher than the other two, which are approximately negligible inside the PMs hole. The trend of B_y as a function of x and z in planes passing through the PMs centers is depicted in Fig. 2.7b and 2.7c. In particular, along z the double gaussian trend due to the presence of tho separate PMs can be seen. In fact, the solution with two PMs has been preferred

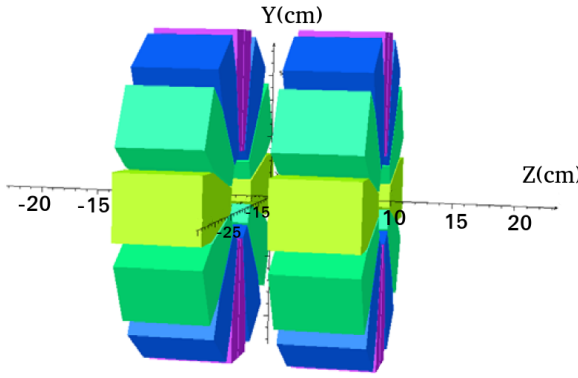

Fig. 2.6: Schematic view of the two magnets in Halbach configuration. The center of the magnetic system coincides with the center of the reference frame.

to a single PM in order to place an intermediate station for momentum measuring. The extent of the fringe field along z is proportional to the to the inner radius R_{in}.

To enhance the momentum measurement resolution, the particles deflection, or the gained transverse momentum Δp_T, must be maximized. Since we have that

$$\Delta p_T = q \int_0^L B \, dl \tag{2.13}$$

where q is the particle charge, B the intensity of the magnetic field and L is the length of the magnetic field, to improve the resolution the crucial parameters are B and L. The Halbach configuration is characterized by a field intensity which is proportional to the ratio between the external and internal radii, R_{out} and R_{in}, in particular:

$$B \propto \ln\left(\frac{R_{out}}{R_{in}}\right) \tag{2.14}$$

The value of R_{in} is assessed by the angular aperture of fragments and the distance between the PMs and the target, while R_{out} value has to be a compromise between the desired B field intensity and the cost. A B field with a maximum value of $0.8 - 0.9\,\mathrm{T}$ is a reasonable choice, and higher value may be difficult to obtain due to saturation effects arising around $1.19\,\mathrm{T}$. The PMs length affects the overall length of the magnetic field region: longer PMs (along their axis direction) would increase the particles deflection, but would also mean a higher cost. At present, the PMs dimensions are still being optimized, and a realistic values are: length in the range $7\,\mathrm{cm} - 10\,\mathrm{cm}$, internal radius of $4\,\mathrm{cm}$, blocks thickness ($R_{out} - R_{in}$) of about $10\,\mathrm{cm}$.

Vertex detector

The Vertex detector (VTX) is a stack of four MIMOSA28 (M28) silicon chips[1] (Fig. 2.8a) belonging to the family of the CMOS Monolithic Active Pixel Sensors (MAPS), which

[1] www.iphc.cnrs.fr/PICSEL.html

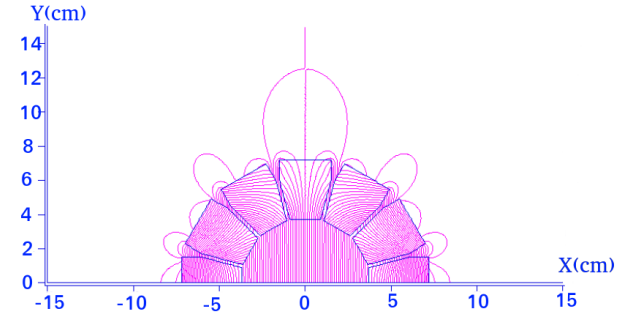

(a)

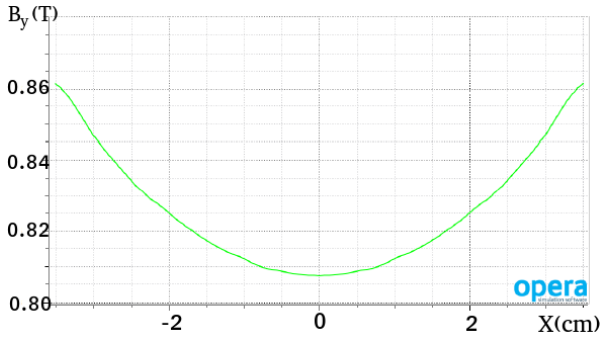

(b)

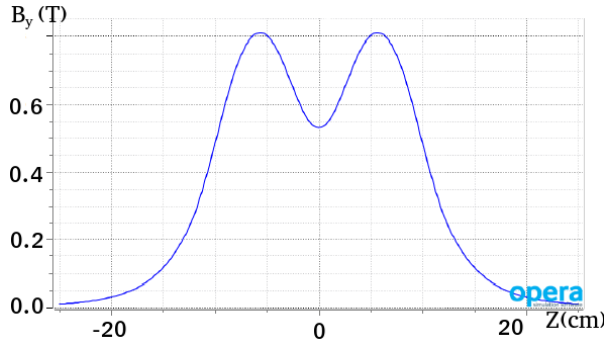

(c)

Fig. 2.7: (a) Simulation of the magnetic field lines in $x - y$ plane. (b) B_y as a function of x (at y=0 and z =center of one of the PMs) and (c) as a function of z (at x=y=0). All the figures have been obtained for two 7 cm long (along z) PMs with 10 cm blocks thickness.

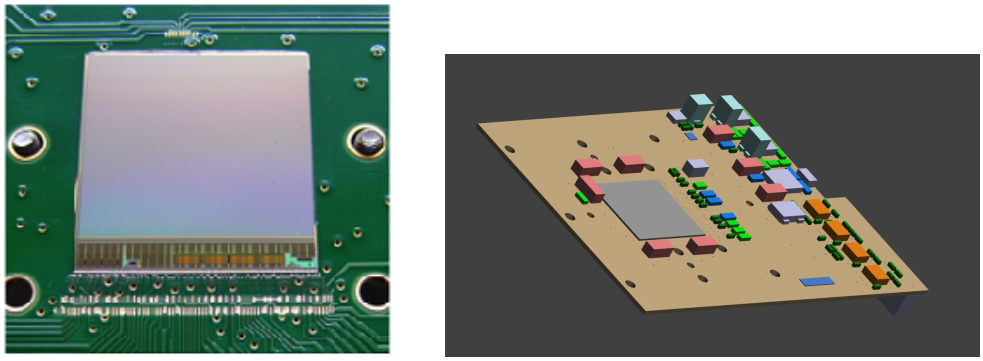

(a) (b)

Fig. 2.8: (a) Picture of a M28 chip. (b) Technical drawing of one of the VTX boards; the gray box in the middle represents the sensor.

are commonly used for experiments in particle and heavy ion physics. The sensor is a matrix of 928 rows×960 columns of pixels, $20.7\,\mu\mathrm{m}$ pitch, for a total sensitive area of $20.22\,\mathrm{mm} \times 22.71\,\mathrm{mm}$. The thickness of each sensor is $50\,\mu\mathrm{m}$. Each sensor will be housed in a dedicated read-out board (Fig. 2.8b). The VTX stack will consist of two sub-stations with two sensors each: within the same sub-station the sensors will be placed at a relative distance of $2\,\mathrm{mm}$ to each other, while the two sub-stations will be separated by about $10\,\mathrm{mm}$ due to the size of the board electronic components.

This detector is placed right after the target ($\sim 0.5\,\mathrm{cm}$) and is the first tracking station of the magnetic spectrometer: it contributes to the measurement of the particles momentum in the magnetic field and will evaluate for each event the vertex position, *i.e.* the position inside the target where the beam interacted originating the fragments. When a charged particle crosses this kind of detector, it produces a signal in a number of pixels which is proportional to the energy loss: by means of dedicated reconstruction clusterization algorithms an accuracy of few $\mu\mathrm{m}$ on the particle position can be achieved.

Inner Tracker

The Inner Tracker (ITR) is the second station of the magnetic spectrometer and is placed between the two permanent magnets, at a distance of about $20\,\mathrm{cm}$ from the target. At this point, accordingly to the emission angle distribution, the fragment spatial distribution is broader here than in the VTX. Consequently, the area to be covered is larger. The choice of the detector has fallen again upon M28 chips, as for the VTX. However, since each sensors covers an area of about $2\,\mathrm{cm} \times 2\,\mathrm{cm}$, a different spatial configuration is needed. It has been proposed to employ a structure composed by ladders similar to the ones implemented in the PLUME project[2] (Fig. 2.9a), where each ladder is composed by two modules housing six M26 pixel sensors (a former and smaller version of M28) each, to implement a double plane tracker. In the FOOT setup, the six M26 will be replaced by

[2] www.iphc.cnrs.fr/PLUME.html

four M28 sensor per plane in each module. Four of these ladders will be disposed as sketched in Fig. 2.9b to cover a total area of about $8\,\mathrm{cm} \times 8\,\mathrm{cm}$. In each module the four sensors are glued and bonded on a kapton Flexible Printed Cable (FPC), having two or three conductive planes and an overall thickness of about $100\,\mu\mathrm{m}$. The two modules of the same ladder are glued on a $2\,\mathrm{mm}$ layer of silicon carbide low-density foam, which determines the distance between the modules (Fig. 2.9c). To minimize the horizontal dead area the distance between two consecutive sensors in the same module is about $30\,\mu\mathrm{m}$, as achieved in the PLUME project.

Microstrip Silicon Detector

The Microstrip Silicon Detector (MSD) is the final station of the magnetic spectrometer and consists of a telescope of microstrip layers placed beyond the PMs and at about $35\,\mathrm{cm}$ from the target. This detector has a dual role: it will give information about the track position to contribute to the momentum reconstruction, but it will also measure the fragments ΔE. In this way, together with the scintillator energy loss measurement, two separated and independent estimation of the ΔE will be provided.

Three layers of orthogonally oriented silicon miscrostrips will cover a total area of about $9\,\mathrm{cm} \times 9\,\mathrm{cm}$, separated from one another of approximately $2\,\mathrm{cm}$. A strip pitch of $125\,\mu\mathrm{m}$ has been chosen as a good compromise between the resolution requirements and a reasonable number of readout channels. A spatial resolution $< 35\,\mu\mathrm{m}$ can be achieved with a analogue readout.

The sensors can be of two types:

1. *Single-Sided Strip Detector* (SSSD). The sensor is $150\,\mu\mathrm{m}$ thick and is composed of parallel microstrips. In this case two planes with perpendicular strips would be glued together (biadhesive kapton). The total thickness of each plane of the MSD, $300\,\mu\mathrm{m}$ thick, can provide a good ΔE measurement, however it can also represent a problem in terms of MCS and re-fragmentation.
2. *Double-Sided Strip Detector* (DSSD). In this case each sensor provides orthogonally oriented strips with the same thickness, therefore the thickness of each plane of the MSD would be half with respect to SSSD case.

The read-out chip was tested last year in Trento and Laboratori Nazionali del Sud (LNS) with $300\,\mu\mathrm{m}$ thick DSSDs. It has been verified that no saturation even for low energy ions occurred.

The detectors composing the magnetic spectrometer, except the VTX, will be placed at different distances from the target, depending on the beam energy. At $200\,\mathrm{MeV/u}$ the system ITR-PM will be placed at $\sim$30 cm from the target and the MSD at $\sim$60 cm. At higher beam energy ($700\,\mathrm{MeV/u}$) the system ITR-PM and the MSD will be shifted forward ($\sim$30 cm and $\sim$60 cm respectively), in order to increase the magnetic region length L and improve the momentum resolution. Since the detectors and PMs transversal dimensions do not change, the expansion of the overall longitudinal dimension of the magnetic spectrometer leads to a decrease of the angular aperture. However, this will not be an issue because, at high energy, fragments are even more forward peaked and

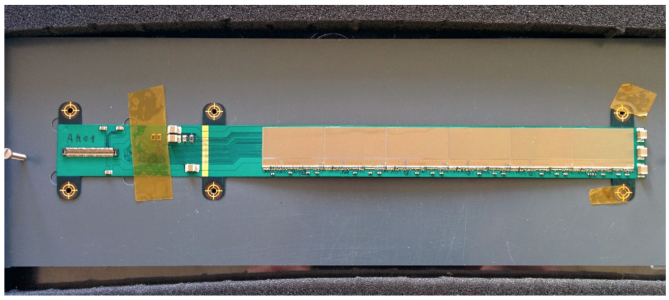

(a)

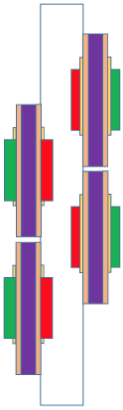

(b)

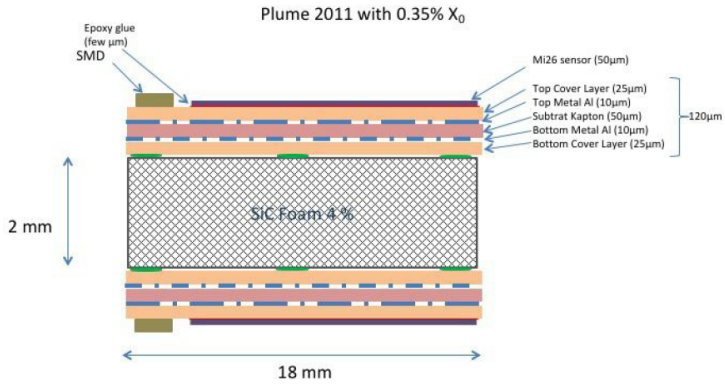

(c)

Fig. 2.9: (a) Picture of a PLUME ladder. (b) Schematic view of the ITR setup. (c) Transversal section of a PLUME ladder.

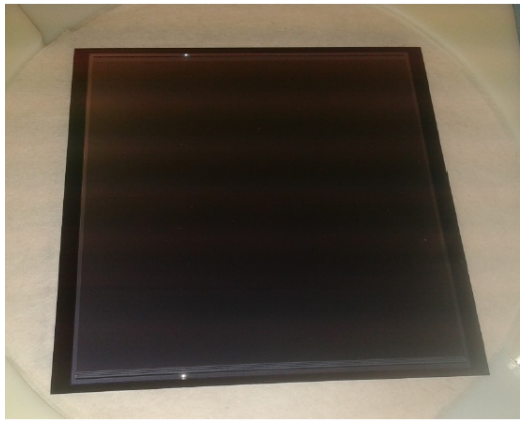

Fig. 2.10: Picture of a MSD layer prototype.

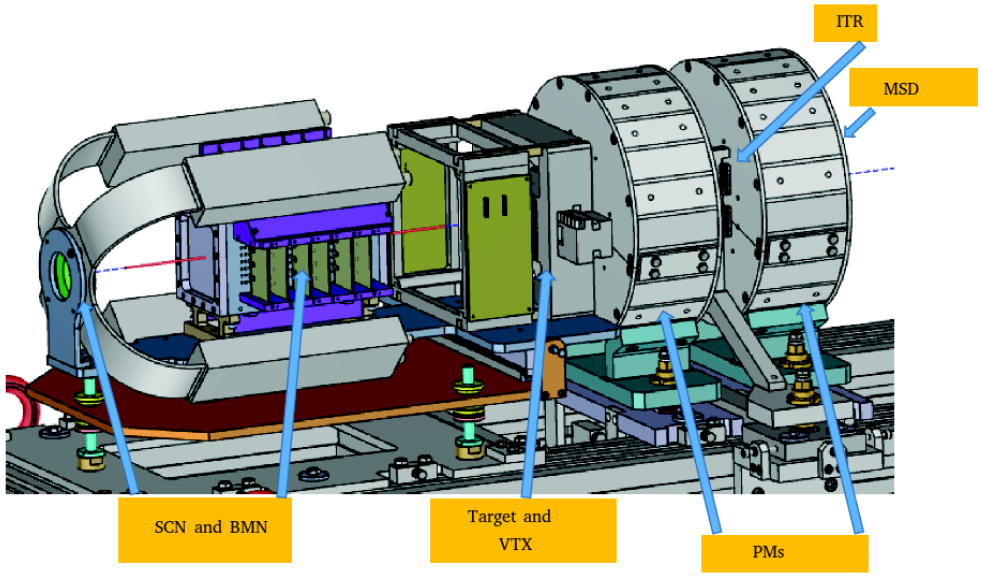

Fig. 2.11: Technical drawing of the mechanics for the pre-target, target and magnetic spectrometer regions.

well contained in a smaller solid angle. From a practical point of view, the shift of the detectors will be possible thanks to a dedicated mechanics which also includes the target (Fig. 2.11).

2.4.3 Downstream region

A plastic scintillator and a calorimeter are the last detectors composing the FOOT electronic setup. Their distance with respect to the target position will be changed according to the primary beam energy: at $200\,\mathrm{MeV/u}$ they will be placed at a distance of about $1\,\mathrm{m}$ from the target, while at $700\,\mathrm{MeV/u}$ their position will be moved downstream to about $2.9\,\mathrm{m}$. This would permit an improved estimation of the fragments β thanks to the increased lever arm. These measurements at high energy will be performed at the GSI, since at the CNAO and HIT facilities the highest energy available is well below $500\,\mathrm{MeV/u}$. Therefore, the increase of the total setup size will not be an issue, since the GSI experimental cave is spacious enough.

Scintillator detector

The Scintillator detector (SCN) will both measure fragments ΔE and stop the time of flight measurement. It is composed of two layers of 20 orthogonally oriented plastic scintillator bars (EJ200), each one $3\,\mathrm{mm}$ thick, $2\,\mathrm{cm}$ large and $40\,\mathrm{cm}$ long (Fig. 2.12a), with a covered total area of $40\,\mathrm{cm} \times 40\,\mathrm{cm}$ that matches the fragments aperture at $1\,\mathrm{m}$ from the target. The detector granularity has been chosen according to the fragments expected separation at $1\,\mathrm{m}$. The bars thickness, instead, is a compromise between the achievable

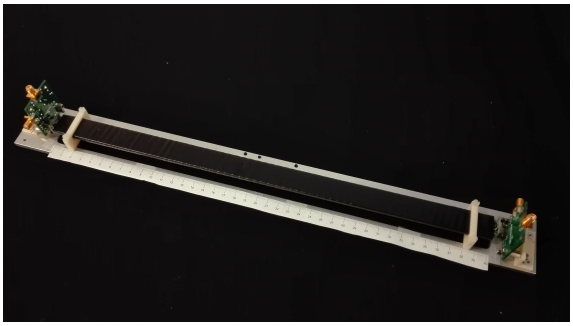

(a)

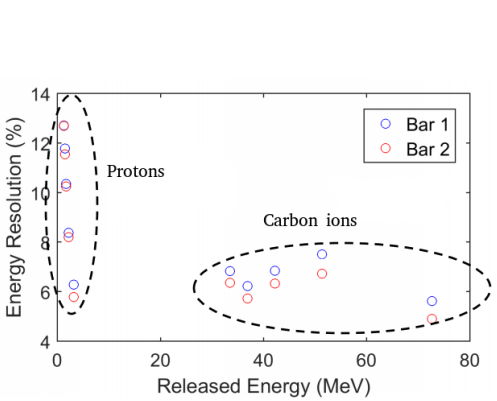

(b)

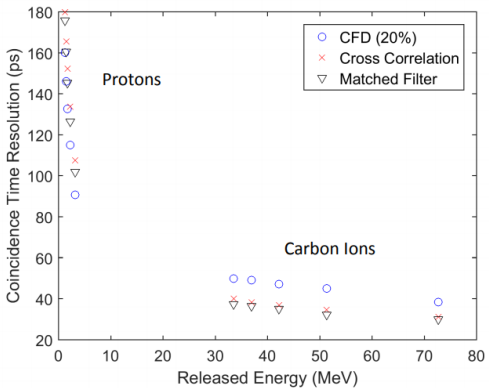

(c)

Fig. 2.12: (a) Picture of a SCN bar prototype. (b) Energy resolution calculated for the two tested bars as the ratio of the standard deviation and the mean of the collected energy as a function of the deposited energy ΔE. (c) Coincidence time resolution obtained with the two bars and calculated with different methods. In both plots the points at high ΔE correspond to carbon ions, while the ones at low ΔE are are protons.

ΔE resolution and the effort to reduce the secondary fragmentation probability: in fact, while a thicker bar would provide a higher light output and therefore an improved ΔE resolution, due to the longer thickness to be traversed it would also enhance the probability of re-fragmentation, thus spoiling the ΔE measurement. Each bar will be coupled by means of an optical glue at both ends to up to four SiPMs connected in series on each side.

An experimental campaign designed to study the detector energy and time resolution, the expected light attenuation inside the bars and the position reconstruction capability have been carried out at Trento Proton Therapy Center (Morrocchi et al. 2018) and at CNAO. Two prototype bars have been exposed to proton and carbon ion beams at different energies, ranging from 60 to 230 MeV for protons and from 115 to 400 MeV/u for carbons. The energy resolution has been obtained as the ratio of the standard deviation and the mean of the collected energy is depicted in Fig. 2.12b as a function of

the released energy. It ranges between 6% and 13%. The resolution obtained on time measurement is about $30 - 40\,\mathrm{ps}$ for carbon ions and higher than $100\,\mathrm{ps}$ for protons. The standard deviation of the coincidence time resolution obtained is reported in Fig. 2.12c as a function of the deposited energy.

The test also proved that the energy collected at the two end of the bar is a function of the beam interaction position. Therefore, this dependence can be exploited to retrieve the interaction position.

Calorimeter

The last detector is a bismuth germanate (BGO) crystals Calorimeter (CAL) designed to measure the kinetic energy of the fragments that will stop inside it. The 288 crystals composing the calorimeter have a truncated pyramid shape and are $24\,\mathrm{cm}$ long, with a front face area of about $2 \times 2\,\mathrm{cm}^2$ and $3 \times 3\,\mathrm{cm}^2$ the outer face (Fig. 2.13a). They will be arranged in a pointing geometry (Fig. 2.13b) and they will be read-out by $8 \times 8\,\mathrm{mm}^2$ SiPMs. Since the whole detector weight exceeds $300\,\mathrm{kg}$, a robust and solid support mechanics is needed to maintain the crystals in the desired configuration. At present, an ensemble of 3D-printed plastic boxes, each one housing a matrix of 9×9 crystals is under study.

Recent tests performed with proton, $^4\mathrm{He}$ and $^{12}\mathrm{C}$ ion beams have been performed at HIT to study the energy resolution. The energy resolution has been obtained as the width of the signal peaks (Fig. 2.13c) for all the three beams at different energies (Fig. 2.13d). The test demonstrated that a relative energy resolution ranging between 1-3% can be achieved.

A non negligible issue associated with this kind of detector is the production of neutrons, since when a fragment undergoes nuclear interaction inside a crystal, one or more neutrons can be produced: they can travel far from the calorimeter, carrying away part of the fragments energy and thus spoiling the measured kinetic energy, which would be lower than the true one (more details in Sec. 4.3).

2.4.4 DAQ and trigger

The FOOT detector will be equipped with a Data Acquisition (DAQ) system designed to acquire the largest sample size with high accuracy in a controlled and online-monitored environment. The DAQ system that will be implemented is a flexible hierarchical distributed system based on Linux PCs, VME crates and boards and standard communication links like Ethernet, USB and optical fibers.

Since due to the high number of read-out channels the M28 of the magnetic spectrometer are the slowest detectors in the FOOT setup, the maximum rate is dictated by their read-out time ($\sim 180\,\mu\mathrm{s}$). Therefore the FOOT setup will operate at a maximum rate of about 1-$10\,\mathrm{kHz}$.

To avoid any source of systematic errors due to the trigger selection, the main trigger of the experiment will be very simple: a minimum bias trigger on signals provided by the STC. The trigger signal will be obtained asking for at least a time coincidence between a certain number of SiPMs signals in the STC within a small time gate. Both the number of SiPMs and the time gate value are still matter of study. However, other trigger solutions

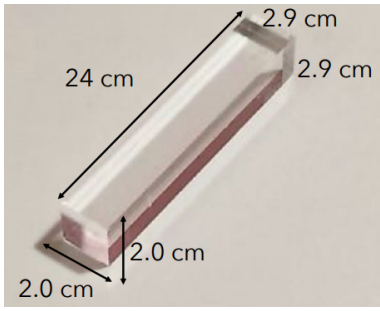

(a)

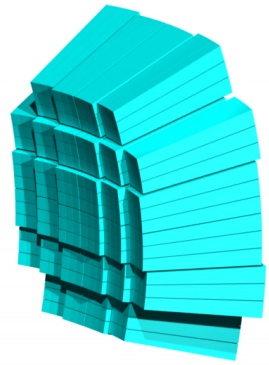

(b)

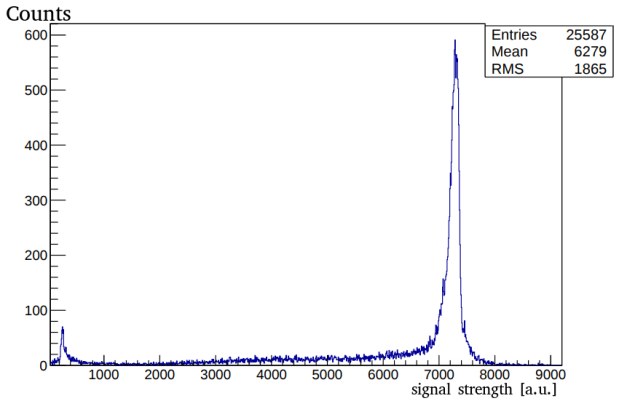

(c)

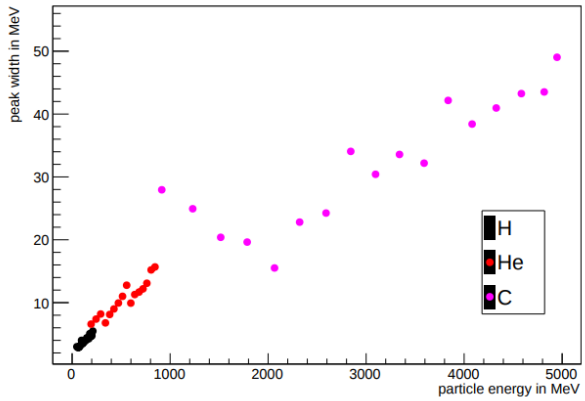

(d)

Fig. 2.13: (a) Picture of a BGO crystal and (b) schematic view of the CAL crystals setup. (c) Signal induced by a $430\,\mathrm{MeV/u}$ carbon beam. (d) Energy resolution (peak width in MeV) for proton, helium and carbon at different energies.

will be explored: in fact, to avoid possible pile-up in the detectors, a more sophisticated trigger able to exclude the events in which the primary has not interacted with the target could be envisaged.

2.5 Emulsion spectrometer

To characterize the production of low-Z fragments ($Z \leq 3$) an Emulsion Cloud Chamber (ECC) detector has been envisaged, since it extends the angular acceptance up to about $70°$. The capability of this kind of detector to separate and measure different fragments produced by ion beams at therapeutic energy has already been proved (De Lellis et al. 2007; Aleksandrov et al. 2015). The first data taking is foreseen in late 2018 at GSI, to explore the nuclear fragmentation of helium ion beams at $700\,\mathrm{MeV/u}$.

Emulsion films allow for a high spatial resolution in tracking ionizing radiation in the three dimensions, as well as a measure of the ionization. The emulsion films employed for FOOT are similar to the ones used in the OPERA experiment and are composed of $70\,\mu\mathrm{m}$ thick sensitive layers made of AgBr crystals of $0.2\,\mu\mathrm{m}$ diameter scattered in a gelatine binder, and placed on the two sides of a $180\,\mu\mathrm{m}$ plastic base (Fig. 2.16), with a total thickness of $320\,\mu\mathrm{m}$ and a transversal area of $12\,\mathrm{cm} \times 10\,\mathrm{cm}$. When a ionizing particle passes through a nuclear emulsion film, it produces a latent image which, after a chemical process called *development*, is converted into a sequence of silver clusters, or *grains*, with diameter of the order of $0.6\,\mu\mathrm{m}$. This sequence represents the particle track: position and direction can be measured with high accuracy ($\sim 0.06\,\mu\mathrm{m}$ and $0.4\,\mathrm{mrad}$ respectively), while the energy loss, and thus the charge according to Eq. 1.5, can be retrieved from the grain density (about 30 grains/$100\,\mu\mathrm{m}$ for a minimum ionizing particle) (De Lellis et al. 2007). The grain density is proportional to the energy loss only over a certain energy range, above which a saturation effect takes place. To measure the energy loss of highly ionizing particles such as carbon ions, after the exposure and before the development emulsion films must be treated trough a specific procedure named *refreshing* (Fig. 2.15): this consists in keeping them at certain temperature ($> 30\,°\mathrm{C}$) and relative

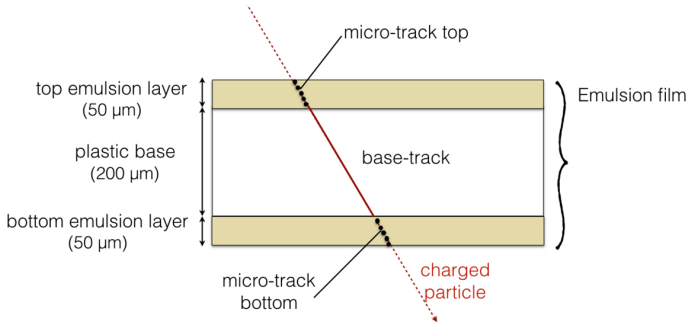

Fig. 2.14: Scheme of the tracks reconstruction: a micro-track is formed by a sequence of clusters aligned in the top or bottom layers, while a base-track in constituted by geometrically aligned top and bottom micro-tracks.

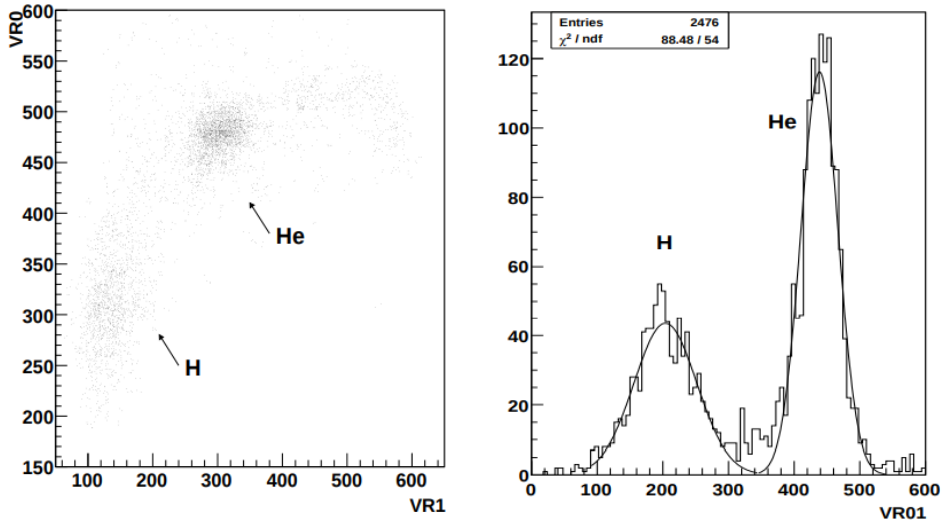

(a) (b)

Fig. 2.15: Results of the charge measurement of fragments produced by a $400\,\mathrm{MeV/u}$ performed with the nuclear emulsion technique (De Lellis et al. 2007). (a) Scatter plot of VR_0 versus VR_1 (volume-tracks obtained in two different refreshing conditions) providing the separation of hydrogen from helium . (b) Projection of the scatter plot onto an axis passing through the centers of the hydrogen and helium peaks.

humidity ($\sim 98\%$) for a suited amount of time after exposure, in order to partially or totally erase the tracks of particles and overcome the saturation effect. The disentanglement of particles with different ionization powers, and thus with different charge can be achieved by combining several films having undergone different refreshing treatments.

In the past, the emulsions technique was limited by the slowness of the read-out stage performed by visual inspection at the microscope. Today, recent innovative read-out technologies provide high speed automated scanning, overcoming this problem. Dedicated softwares running on GPUs are designated to recognize aligned dark pixels clusters corresponding to particle tracks. A straight sequence of pixels in one emulsion layer defines a *micro-track*, while two aligned micro-tracks belonging to the top and bottom layers of an emulsion film constitutes a *base-track* (Fig. 2.14). Base-tracks aligned along different films are connected to form *volume-tracks*. The propagation and fitting of track segments from an emulsion layer to the next permits the particle track reconstruction.

The emulsion spectrometer is composed by three sections (Fig. 2.16), in which these nuclear emulsion films are interleaved with passive layers made of different materials and having different roles:

1. *Vertex and tracking section.* The first section consists of several elementary cells made of emulsion films interleaved with carbon or C_2H_4 layers ($1\,\mathrm{mm}$). These passive layers act as targets, while the emulsions reconstruct the vertex position. The

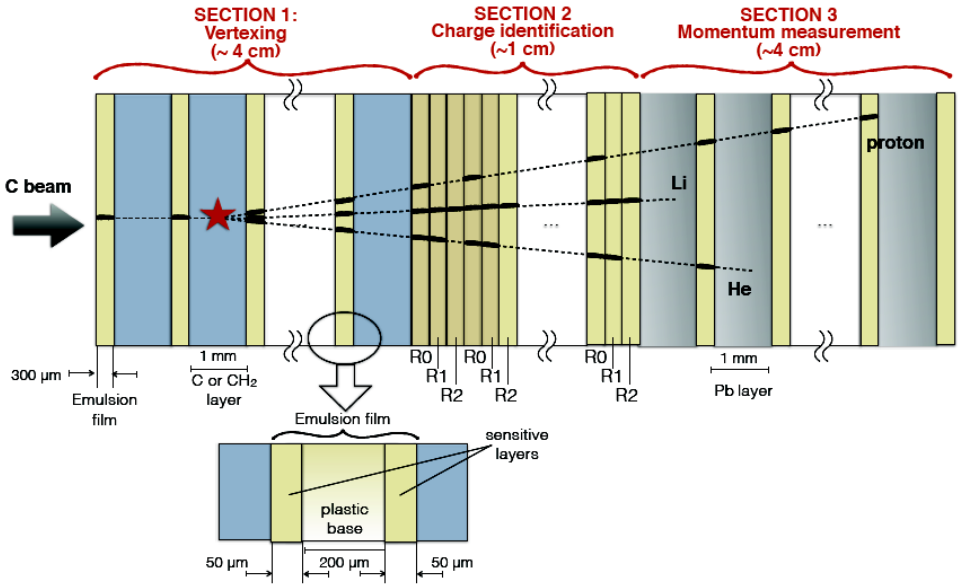

Fig. 2.16: Schematic overview of the ECC layout (not to scale).

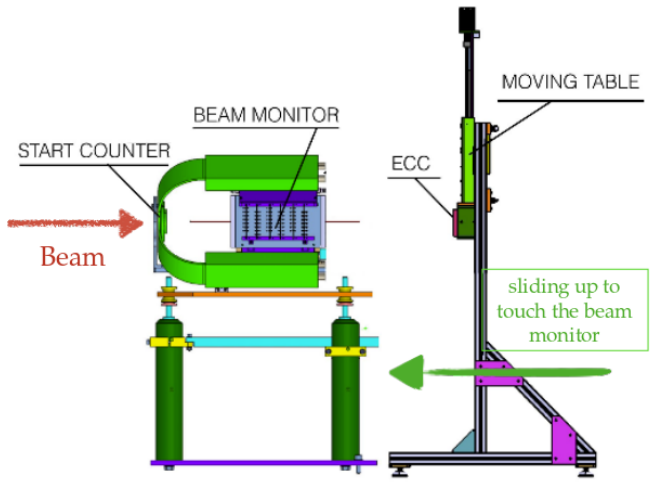

Fig. 2.17: Representation of the ECC experimental setup: the incoming beam is monitored by the STC and the BMN, while the emulsion stack is placed on a movable table that can be shifted in the plane transversal to the beam.

number of elementary cells has been optimized to achieve a statistically significant number of interactions.

2. *Charge measurement section.* This section is entirely composed of emulsion films, aiming to reconstruct light fragments charge. The dynamical range of FOOT ECC will be enhanced by the refreshing procedure. In this case, the elementary cell is made of three emulsion films, each of which is treated with different temperatures during the refreshing procedure. A sequence of 10 elementary cells is foreseen.

3. *Energy and mass measurement section.* The last section is composed of emulsion films interleaved with layers of passive absorbers made of high-Z material. By measuring the entire particle track length, the kinetic energy can be evaluated on the basis of the correlation between range and momentum. The number of elementary cells, the passive material composition and its thickness have to be optimized accordingly to the primary particle type and energy: reasonable choices are lead and tungsten, $1 - 2\,\mathrm{mm}$ thick, and a number of cells increasing with primaries energy and ranging between 10 and 50. The particles momentum can be estimated through the MCS method: by measuring the x-y spatial coordinates and the slope, the particle momentum p can be evaluated according to the formula

$$p = \frac{13.6\,\mathrm{MeV}}{\beta\ \delta\theta}\sqrt{\frac{x}{X_0}} \tag{2.15}$$

where $\delta\theta$ is the deviation of the track slope along its path (see also Sec. 1.2.3). The range and MCS methods are two independent procedures to measure energy and momentum, allowing the isotopic determination of the fragments.

The experimental setup envisaged for the next data taking at GSI, includes also the STC and the BMN (Fig. 2.17), since emulsions can be affected by a saturation phenomenon due to a too high density of tracks (local pile-up occurs at a particle density of about 1000 tracks/cm^2): therefore the beam rate will be monitored by the STC and the BMN will check its transversal profile for absolute flux normalization. The ECC will be placed on a remotely controlled table that allows to move the detector in the plane transversal to the incoming beam direction, in order to uniformly distribute the beam on the ECC surface and keep the particle density below the saturation threshold.

CHAPTER 3

Monte Carlo simulations

Even if the nuclear interaction models included in simulation codes are not enough reliable to provide physics outcomes with the accuracy required to produce sound radiobiological models, MC simulations can be safely used to drive the FOOT detectors design. In fact, during the planning stage, the MC simulation of the FOOT experimental setup has been, and still is, a powerful tool to optimize the design and identify possible critical points in the layout. Beyond the optimization, an important purpose of the simulation is the investigation of expected performances of the detectors, in order to improve the experimental accuracy and to learn how to reconstruct the events by combining the signals from the different detectors.

The MC code adopted to perform the simulations of the FOOT experimental setup is FLUKA (Ferrari et al. 2005; Böhlen et al. 2014). FLUKA has been preferred to other simulation codes since it has been robustly tested through the comparison with many experimental data and, nowadays, it is extensively adopted in many physics fields of study, such as particle, nuclear and medical physics. In particular, many FLUKA developments, concerning both physics models and the user interface, have been studied for its application in the context of PT. For these reasons, FLUKA is used at CNAO and HIT for clinical and research purposes. A recent review of FLUKA application in particle therapy can be found in a work by Battistoni et al. (2016b). Moreover, FLUKA has been used also for the simulation of experiments dedicated to fragmentation (Pleskac et al. 2012; Toppi et al. 2016) and test beams for the study of secondary particles production with therapeutic beams (Agodi et al. 2012; Piersanti et al. 2014; Mattei et al. 2017).

This chapter describes the development of the FOOT simulations carried out in the last three years. In Sec. 3.1 an overview of the FLUKA MC code is outlined, with particular attention to the hadronic models and the input construction. In Sec. 3.2, the methods employed to build the simulation input are reported, while in Sec. 3.3 is described how the customized FOOT output has been obtained by means of an advanced use of the FLUKA code. Finally, in Sec. 3.4, some considerations about CPU time and memory usage required by a simulation run are presented.

3.1 FLUKA MC code

The FOOT simulation has been built within the framework of the FLUKA[1] code (Ferrari et al. 2005; Böhlen et al. 2014). FLUktuierende KAskade (FLUKA) is a general purpose MC tool developed by the INFN and the European Organization for Nuclear Research (CERN). It is adopted in a wide range of applications, such as calorimetry, dosimetry, detector design, cosmic rays, neutrino physics, radiotherapy and many others. The code is developed using FORTRAN (both 77 and 95) language and is regularly updated and improved.

FLUKA is a theory driven MC code, and it has been extensively benchmarked with experimental data at single interaction level. Its predictions are obtained with minimal free parameters, which are fixed for all energies, targets and projectiles. FLUKA is based on original and extensively tested microscopic models, which consider the basic constituents of matter. The microscopic approach ensures correlations among the shower components and within interactions. It also provides predictions where no experimental data are available and ensures the fulfilling of conservation laws.

FLUKA is capable of simulating the transport and the interactions of particles in complex geometries, magnetic fields and in a wide range of materials. The code can handle the transport and the interactions of photons, leptons and hadrons from a few keV (or from thermal energies for neutrons) up to cosmic ray energies. As far as hadrons are concerned, all known mesons and baryons can be transported, apart from those composed by the bottom and top quarks. Moreover, FLUKA can also handle the transport and interactions of ionized nuclei, which is particularly advantageous in PT applications.

Flair, a graphical user interface based on Python, Tk, gnuplot and C++ (Vlachoudis et al. 2009), has been developed for a more friendly usage of FLUKA: it allows to edit, compile and run the input files (Fig. 3.1). It permits to visualize the geometry coded by the user and the possible errors in the geometry implementation.

[1] http://www.fluka.org

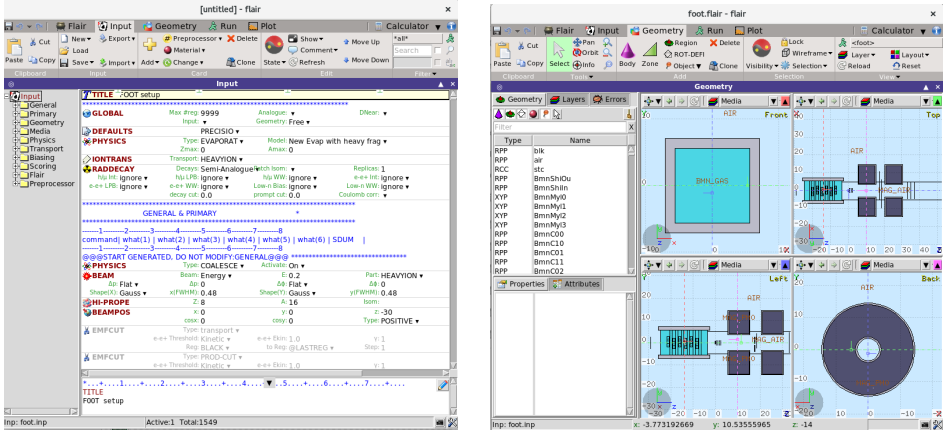

Fig. 3.1: The Flair interface allows the user to visualize the input file (left) and the geometry (right).

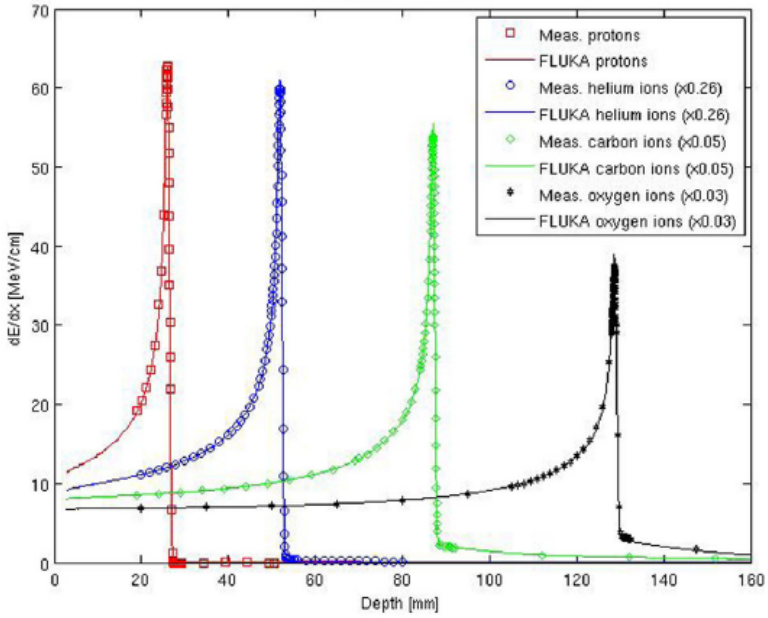

Fig. 3.2: FLUKA simulations of Bragg curves of protons ($54.19\,\mathrm{MeV}$), helium ($79.78\,\mathrm{MeV/u}$), carbon ($200.28\,\mathrm{MeV/u}$), and oxygen ions ($300.13\,\mathrm{MeV/u}$) compared with measured data at HIT (Battistoni et al. 2016b).

3.1.1 Physics Models

As seen in Sec. 1.2, charged particles mainly interact with matter through Coulomb electromagnetic interactions. In FLUKA, electronic stopping powers are calculated on the basis of the Bethe-Block formalism. In recent years, several corrections to the standard formalism have been applied to overcome the common simplifications due to Born approximation, thus achieving the high precision needed for the transport of therapeutic beams (Fig. 3.2). Nuclear stopping power is also considered.

In FLUKA, charged particles are transported through an original MCS algorithm, based on the Molière theory and including also an optional single scattering method (Ferrari et al. 1992). Instead of the standard Landau or Vavilov description (Landau 1944; Vavilov 1957), a statistical approach is used to simulate the energy loss of charged particles (Fassò et al. 2007) with satisfactory results (Fig. 3.3). The transport algorithm coded in FLUKA allows to accurately handle even some challenging problems, such as electron back-scattering and energy deposition in thin layers, even at energies of the order of few keV.

Since the goal of the FOOT experiment is to study the nuclear interactions of therapeutic ion beams, this section mostly focuses on FLUKA hadronic models, while the electromagnetic interactions, instead, are only briefly summarized in Fig. 3.4.

A description of the FLUKA hadronic models is reported in this section. However a detailed description of these models is beyond the purpose of this work and additional information can be found in Battistoni et al. (2015) and in Cerutti et al. (2017).

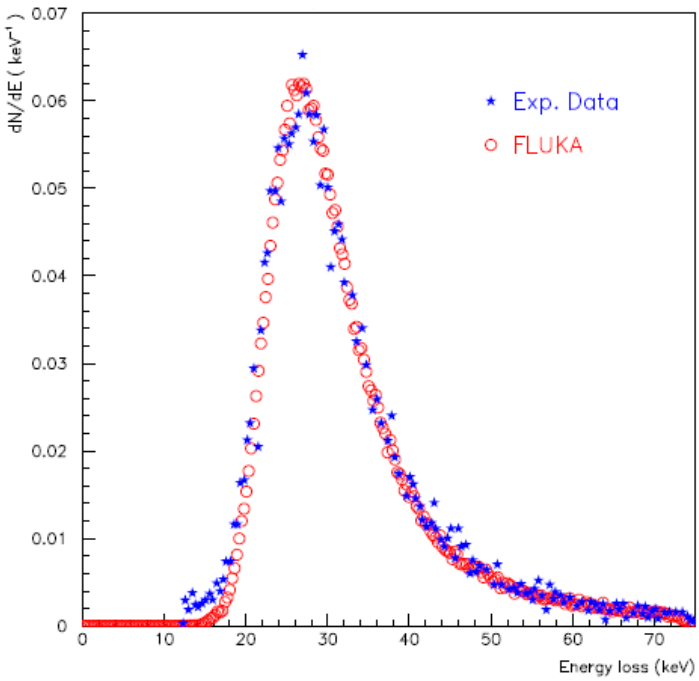

Fig. 3.3: Comparison between the experimental data (Bak et al. 1987) and the FLUKA simulated energy loss distribution for 2 GeV protons on a 100 µm thick silicon detector (Fassò et al. 2007).

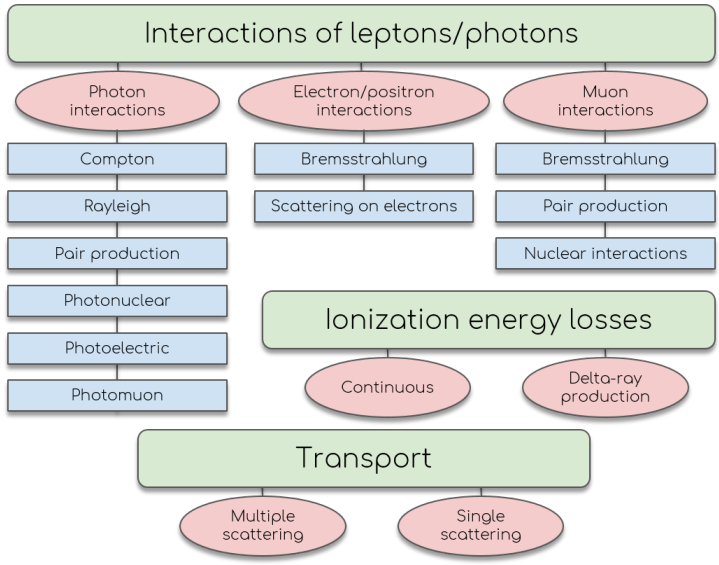

Fig. 3.4: Electromagnetic interactions considered in FLUKA [`www.fluka.org`].

As explained in Sec. 1.5, no exactly calculable model exists to describe nuclear and hadronic interactions. On the other hand, several high quality models with different energy ranges of applicability have been developed over the years, and FLUKA embeds many of these models, aiming to provide the best and smoothest possible connection between them in the transition energy ranges.

Hadron-nucleon (h-N) interactions

In FLUKA, h-N interactions are simulated through two different models, depending on the energy of the involved particles:

- at energies up to few GeV the isobar model handles the reactions through resonance production and decay
- at higher energies the interactions are described by the *Dual Parton Model* (DPM) (Capella et al. 1994), which is a particular quark/parton string model, coupled to a hadronization scheme.

Inelastic cross sections for h-N interactions are retrieved from parameterised fits based on the experimental data available in literature.

Hadron-nucleus (h-A) interactions

The description of inelastic h–A interactions is obtained through different event generators depending on energy and projectile (Fig. 3.5):

- PreEquilibrium Approach to NUclear Thermalization (PEANUT). This model handles h-A interactions when the momentum is lower than $5\,\mathrm{GeV}/c$ for nucleons, anti-nucleons and pions, and when the kinetic energy is lower than $1.5\,\mathrm{GeV}$ for kaons. PEANUT includes both a *Generalized Intra-Nuclear cascade* (GINC) and a *pre-equilibrium emission* stage. The propagation in the nucleus of the hadrons involved in elementary multiple collisions is simulated through the GINC model. The GINC modeling considers different nuclear densities for neutrons and protons, takes into account the curvature of particle trajectories due to the nuclear potential, employs binding energies obtained from tables, which are updated after particle emission, and ensures the energy-momentum conservation. Quantum effects are included: Pauli blocking, formation zone, nucleon anti-symmetrization, etc. The transition between the GINC and the pre-equilibrium step occurs when the energy of all nucleons drops to about $50\,\mathrm{MeV}$ and all particles except nucleons have been emitted or absorbed. The input configuration for the pre-equilibrium stage is characterized by the number of remnant protons and neutrons in the nucleus, by the number of particle-like excitons (nucleons excited above the Fermi level), and of hole-like excitons (holes created in the Fermi sea by the INC interactions), and by the nuclear excitation energy and momentum.
- *Glauber–Gribov cascade*. This event generator is used when the particle momentum is higher than $5\,\mathrm{GeV}/c$. Multiple collisions of a hadron with the nucleons constituting the target nucleus are considered by means of the Glauber-Gribov mechanism.

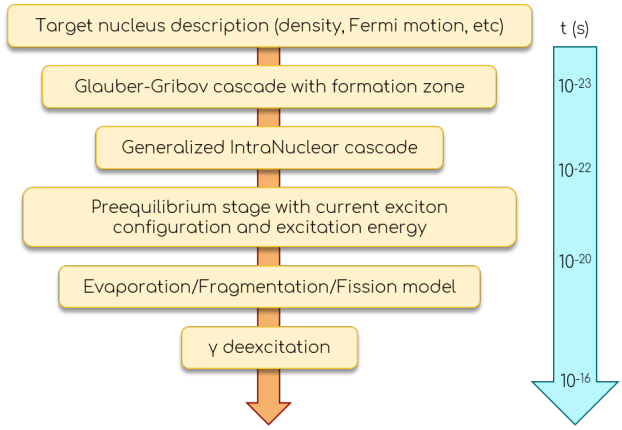

Fig. 3.5: Nuclear interactions flowchart [`www.fluka.org`].

The Glauber cascade is a quantum mechanical method to calculate all relevant hadron-nucleus cross sections (elastic, quasi-elastic and absorption) from hadron-nucleon scattering. Inelastic interactions are treated as multiple interactions of the projectile with n target nucleons. The Glauber-Gribov model is the field theory formulation of Glauber model.

Both generators include *evaporation/fragmentation/fission* and also final γ*-de-excitation*, which take place at the end of pre-equilibrium stage, when the nucleus is in thermal equilibrium system and is characterized by a certain excitation energy. In this last step of the chain, the dissipation of the residual energy can occur through different and competing mechanisms: the nucleus can evaporate (*i.e.* emit nucleons, fragments or γ-rays) or it can undergo fission. In addition, a Fermi break-up model is implemented for light nuclei ($A < 18$). The residual nuclei distributions and the neutrons production are ruled by these processes. Residual mass distributions are very well reproduced, however, the production of specific isotopes may be influenced by additional problems (sensitivity to details of evaporation, nuclear structure effects, etc.).

Nucleus-nucleus (A-A) interactions

Depending on the nucleus energy, the nucleus-nucleus interactions are treated in FLUKA by means of one of the three external generators interfaced with FLUKA (Fig. 3.6):

- *Boltzmann-Master Equation* (BME). Nucleus-nucleus interactions in FLUKA are treated by the BME model interface to FLUKA (Cerutti et al. 2006) for energies below $100\,\mathrm{MeV}$. The BME model describes, by means of a set of time-dependent transport equations, the de-excitation process of a two interacting nuclei system during the pre-equilibrium phase. The evolution towards the equilibrium state is described through a series of two body reactions and the emission of secondary particles with predictable multiplicity.

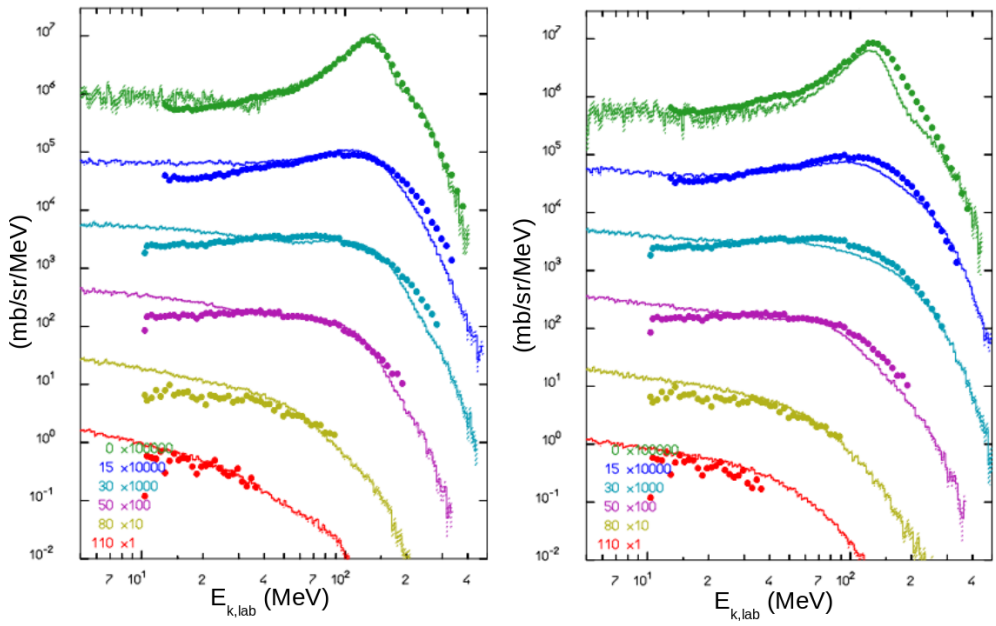

(a) (b)

Fig. 3.6: Neutron double differential production cross sections for C ions on C target at $135\,\mathrm{MeV/u}$ computed with the improved BME (a) and rQMD (b) and compared with experimental data (dots) (Cerutti et al. 2017).

- *Relativistic Quantum Molecular Dynamics* (rQMD). The interaction between two nuclei is described starting from their initial state, in which they are considered as a Fermi gas. The propagation of each nucleon in the potential generated by the others nucleons is described within the quantum mechanical formalism. Besides the dynamical evolution of the interacting particles, this model can also predict the production of fragments and unbounded nucleons. In the energy range $100\,\mathrm{MeV} - 150\,\mathrm{MeV}$ a progressive transition between BME and rQMD takes place. This transition is of particular relevance in PT, since it falls in the energy range relevant for therapy. Due to this reason, a great effort have been made in the recent years to smooth as much as possible the passage from one model to the other. For energies higher than $150\,\mathrm{MeV}$ and lower than $5\,\mathrm{GeV}$ an interface to an extensively modified version (Andersen et al. 2004) of rQMD-2.4 (Sorge et al. 1989; Sorge 1995) has been developed.

- *Dual Parton Model and JETs* (DPMJET-III). It is a QCD inspired MC event generator based on the DPM in connection with the Glauber formalism (Roesler et al. 2001). It is capable of simulating h-h, h-A, A-A interactions from a few GeV up to the highest cosmic ray energies, however FLUKA implements the DPMJET-III only to treat A-A interactions for energies higher than $5\,\mathrm{GeV}$.

```
*...+....1....+....2....+....3....+....4....+....5....+....6....+....7....+...
BEAM          1.E+04    0.0D+00       0.0       0.0       0.0       0.0PROTON
*keyword    momentum mom.spread  diverg.   X-width   Y-width  ignored particle
*            WHAT(1)    WHAT(2)   WHAT(3)   WHAT(4)   WHAT(5)   WHAT(6)   SDUM
```

Fig. 3.7: Example of a FLUKA card (`www.fluka.org`).

All the external generators share the same evaporation/de-excitation stage developed within the FLUKA framework for h–A interactions.

3.1.2 Standard input and geometry

To run a simulation, the user has to prepare an input file, which can be written with an ordinary text editor or by means of the graphic interface Flair. FLUKA inputs are ASCII files with extension `.inp` and are composed of a variable number of *commands*, each one consisting of one or more lines, which are called *cards* for historical reasons. Each card is composed of one keyword, six floating point values called WHATs, and one character string called SDUM (Fig. 3.7). The FOOT input is reported in App. A as example.

Usually, all the instructions needed by FLUKA to run a standard simulation can be given through the available cards in the input file, without requiring any code development from the user. However, there are some situations requiring a more advanced customization level, because the problem is too complex or because the desired output is too problem-specific to be available as a FLUKA standard option, as in the FOOT case (see Sec. 3.3). A higher level of customization can be obtained in FLUKA by means of the *user routines*. FLUKA user routines are a set of subroutines which allow to define non-standard input and/or output. The most of them are collected in the FLUKA standard distribution library as template routines and can be called by inserting specific cards in the input file. The user can modify these templates according to its desire. Since FLUKA is written in FORTRAN, this is also the user routines language.

Typically, the input structure is the following:

- *Titles and comments*. The user must specify the input title in the `TITLE` card and, even if it is not mandatory, it is useful to add some comments for documentation purposes.

- *Physics settings definition*. The user can choose between several pre-defined defaults (card `DEFAULTS`), each one conceived and optimized for specific applications. The defaults set transport and production thresholds for different particles. To override and modify these thresholds, different cards are available: `PART-THR` defines transport and production cutoffs for hadrons, muons and neutrinos; `EMF-CUT` does the same for electrons, positrons and photons; `DELTARAY` activates the δ-rays production by hadrons; `PAIRBREM` controls the simulation of pair production and Bremsstrahlung by hadrons and muons. In addition, `RADDECAY` activates the simulation of radioactive decay.

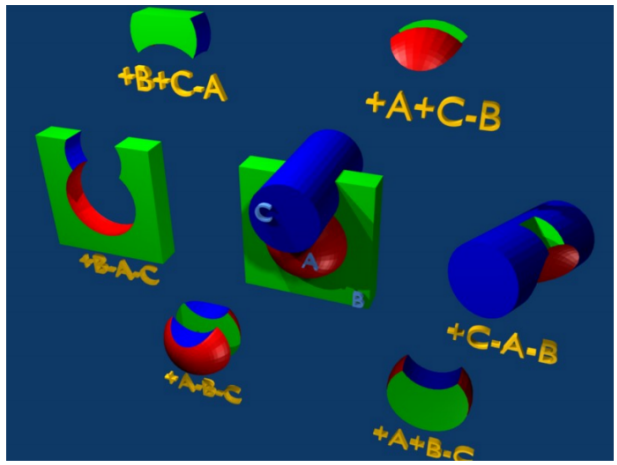

Fig. 3.8: Illustrative examples of FLUKA combinatorial geometry [`www.fluka.org`].

- *Particle source definition*. The beam particle type and energy are defined in the card `BEAM`, while the source position in the card `BEAMPOS`. With these two cards it is possible to define for example gaussian or rectangular distributed sources with a certain angular and energy spread, whereas sources with more complicated spatial, direction or energy distributions require an additional card, `SOURCE`, and the coding of a specific user routine. The `SOURCE` card, in fact, passes some user defined parameter to this dedicated routine. A special case is represented through a heavy ion source: in this case the user has also to specify the charge and the mass of the heavy ion through the card `HI-PROPE`, otherwise a ^{12}C ion beam is assumed as default source.

- *Geometry definition*. In FLUKA the combinatorial geometry is based on the concept of *bodies* and *regions*: the first ones are closed solid figures as spheres (`SPH`), cylinders (`RCC`), parallelepipeds (`RPP`), etc., or semi-infinite portions of space as half-spaces, infinite cylinders, etc., whereas regions, defined by the card `REGION`, are created by combining bodies through Boolean operations, *i.e.* addition, intersection and subtraction (Fig. 3.8). The syntax of the body cards is not unique, because the meaning of the WHATs, which in body defining cards correspond to dimensions and global positions, depends on the body type. Regions are the core elements of FLUKA geometry since, differently from bodies, which are merely shapes in the space, they represent physical objects, each one composed of one single material. FLUKA provides also the option of implementing modular geometries: one single module, composed of an arbitrary number of bodies and regions, can be repeated as many times as needed, avoiding the description of repetitive structures in all details. This can be achieved through the card `LATTICE`. A particularly advantageous feature of FLUKA is the possibility of import in Flair the voxel geometry from a Computed Tomography (CT) scan by means of the card `VOXELS` for PT applications. All medical images in DICOM format (a data interchange protocol

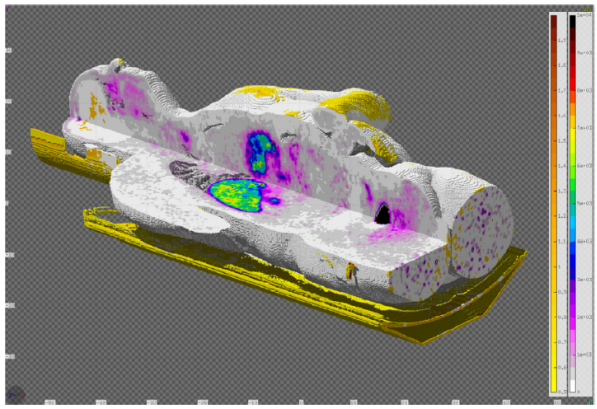

Fig. 3.9: CT voxel geometry and PET dose distribution imported in Flair (Battistoni et al. 2015).

used in medical practice), as PET dose maps and dose distributions from TPS, can be imported and visualized (Fig. 3.9). The definition of bodies and regions must be embraced between the cards `GEOBEGIN` and `GEOEND`. The whole simulated geometry must be surrounded by a particular region, the *blackhole*, which is a fictitious material used to avoid an infinite tracking of particles: each particle crossing the blackhole region boundaries is killed and its tracking is terminated. Sometimes, it is convenient to separate the whole geometry declaration from the rest of the input: the geometry description can be stored in a different file, usually with `.geo` extension, which is recalled by the standard input file. This is particularly advantageous when the same geometry has to be run with different inputs (for example different beam energies): in this case, changes in the geometry can be made in one single `geo` file shared between different `inp`.

- *Material definition*. FLUKA embeds an extensive database containing many pre-defined materials (from elements, to the most common molecules, to complex biological materials), each of them characterized by a default name, density and atomic number and weight. The blackhole region must be filled with a special material, internally called `BLCKHOLE`, which absorbs every particles entering in it. The user can modify the pre-defined materials and can also create its own ones: the card `MATERIAL` must contain the material definition and, if the material is a compound or a mixture, the card `COMPOUND` specifies the atomic composition by mass, atom or volume fraction. As default, for each element composing a material FLUKA considers its natural isotopic composition, unless the user specifies the atomic mass number.

- *Material assignments*. Each region declared in the input file, must be associated to one and only one material via the card `ASSIGNMA`. If several regions made of the same material have been declared in succession they can be filled all at once in one single `ASSIGNMA` card. This card is also used to specify whether the current region is a magnetic region or not.

- *Magnetic field definition*. The card MGNFIELD can be used by the user set some tracking parameters for transport in the magnetic field and to define a homogeneous magnetic field, while more complicated fields require a specific user routine. The defined magnetic field is applied only to the regions declared as magnetic in the ASSIGNMA card. When tracking particles in magnetic field, FLUKA, like many other MC codes, makes use of a specific tracking algorithm because the analytic solution for the crossing of a helix with a generic surface is a time consuming process. Therefore, magnetic field tracking is performed by iterations which are stopped when the desired boundary crossing accuracy is reached. The parameter regulating the tracking in magnetic fields must me carefully set by the user according to the needs of the simulated problem. parameters defining the tracking accuracy.

- *Scoring and estimators definition*. In FLUKA the quantities of interest are scored by estimators acting like virtual detectors. Several kinds of built-in estimators are available: they can score energy and dose deposition, particle fluence, particle double differential yield and many other quantities. Examples of most used estimators are: the USRBIN, whose results are normalized to bin volumes, usually used to estimate the energy or dose deposition in a mesh or in selected regions specified by the user; the USRBDX, used to estimate quantities, for example particle fluence, on a surface; and USRYIELD, employed to measure angular or energy yields around a fixed direction of particles exiting a given surface.

- *Biasing definition*. FLUKA offers the possibility of running the simulation in biasing mode. This is particularly convenient in cases where only few histories contribute to the response of interest, for example when the fluence of particles passing a shield is studied. To speed up the simulation still obtaining meaningful results, the real physical problem can be substituted with a mathematically equivalent one, having the same solution but faster statistical convergence. The card BIASING assigns to each region an importance proportional to how much the particles are expected to contribute to the final result in that region. The biasing algorithm of *splitting/russian roulette* is then performed depending on the ratio between the importance of two subsequent regions. Also other types of biasing algorithm are available. The biasing technique, however, can be employed only when average measurements are pursued: in event-by-event outputs, in fact, it can lead to ambiguous and inappropriate results, since particles are artificially killed or doubled.

- *Random number initialisation*. To perform statistically independent runs, each run must associated to a different seed of the random numbers generator. FLUKA uses a portable random number generator in double precision, named FLRN64, based on the algorithm proposed by Marsaglia & Tsang (2004). This is a high quality generator, whose period is 2^{144} (*i.e.* $\simeq 10^{43}$). In each run the seed must be specified in the card RANDOMIZ to determine the sequence of random numbers for that run.

- *Starting of the run* and *number of primaries*. At the end of the input file, the START card initiates the run. In this card, the number of requested primaries is declared. Each primary particle initiates an *event*, which is the history of the primary particle

itself and all its daughters. An event ends when all the produced particles escape the geometry or when the energy of all particles is below the tracking energy threshold.

In addition to all the presented commands, other special cards are available for more advanced problems, such as transport of optical photons, event by event scoring, calling user routines, etc.

3.1.3 Standard output

The standard output of FLUKA consists of a series of files, of which the most important are:

- a main output file (`*.out`), containing the interpretation of the input and the statistics of the run, as well as many physics information, such as the activated nuclear models, transport thresholds, beam characteristics, materials properties and parameters;
- a file containing the last used random number seeds (`ran*`), useful to simulate more than one independent run to improve the statistical error;
- a file reporting possible error messages (`*.err`);
- files containing the estimators output (`*fort*`), which can be ASCII or binary files, depending on the user wish;
- possible extra output generated by user routines, when present.

3.2 Building the simulation input

The beginning of this PhD work coincided with FOOT early days. Since then, and thanks to the results of the analysis of the produced simulated data, the FOOT experimental setup has undergone many changes and variations, according to which the simulation had to be consequently tuned. In the last three years, several reliable and accurate simulation versions describing the evolving experimental setup have been provided to the FOOT collaboration, in order to optimize the layout, study the detector performances and test the reconstruction code. The last developed simulation version is the number 14 (Fig. 3.10), which has been released few months ago and is now available to the collaboration members in the online repository GIT[2]. This is the first version to be fully integrated in the reconstruction code. In fact, geometry and materials must be identically implemented also in the reconstruction code for track reconstruction purposes. The whole input file of FOOT V14 is reported in App.A.

3.2.1 FOOT input geometry and physics features

In the FOOT geometry implemented in FLUKA, the origin of the reference frame coincides with the center of the target, and the detectors, as can be seen in Fig 3.10a, are

[2] `https://github.com`

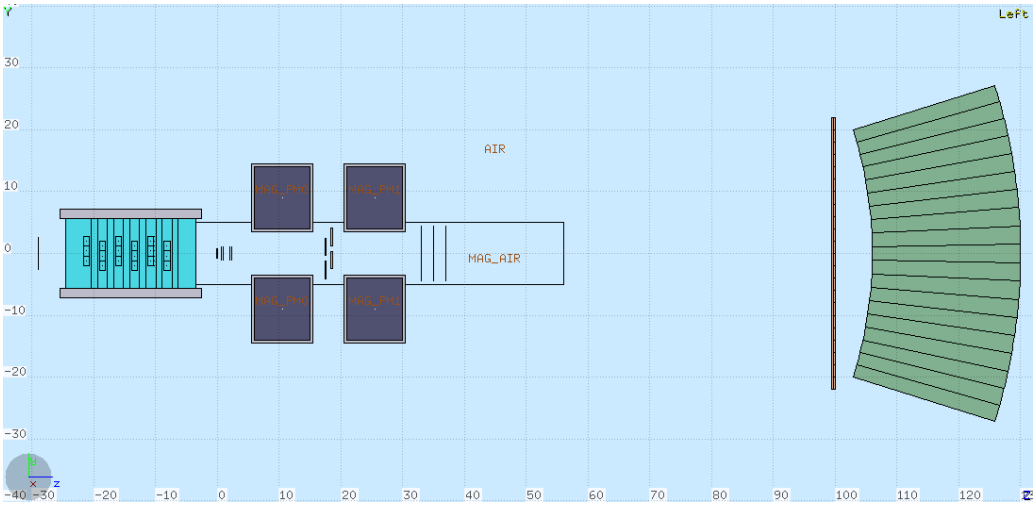

(a)

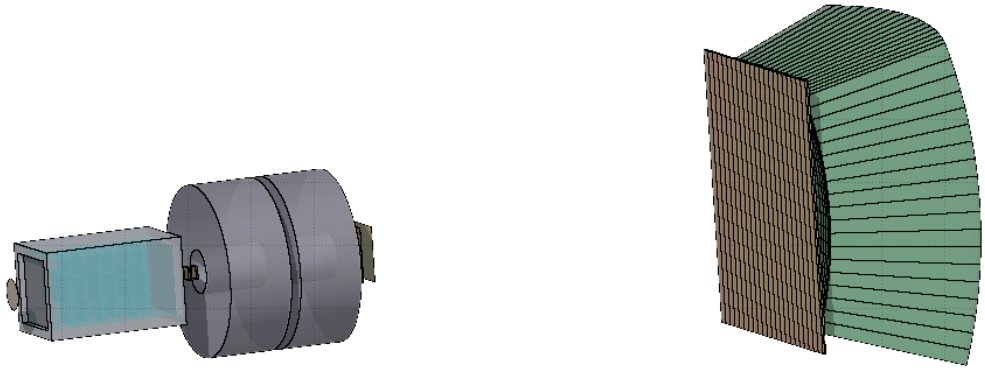

(b)

Fig. 3.10: 2D (a) and 3D (b) view of the simulated FOOT geometry version 14, obtained with Flair GeoViewer.

disposed along the z axis, which is also the beam axis. The FOOT detectors have been implemented in the `geo` file with high accuracy:

- the STC is simply simulated as a very short ($250\,\mu\mathrm{m}$ tall) plastic scintillator cylinder, with the basis perpendicular to the beam axis (Fig. 3.11a-b);
- the BMN is simulated as a parallelepiped filled with gas, surrounded by an aluminum box (Fig. 3.11b-c-d). Fictitious parallelepiped regions of gas simulating the cells have also been added: in this way the scoring can be performed only in the cells and not in the entire gas region, thus saving computing time and memory. Both the anode and the cathode wires have been implemented as well (Fig. 3.11d);

- the target region is simulated as a simple parallelepiped (Fig. 3.11e) made of the desired material (carbon or polyethylene)
- the four VTX planes have been implemented according to the real M28 design (Fig. 3.11e-f). The sensitive region in each VTX plane is in fact bordered with an insensitive silicon frame region. To avoid the implementation of an excessive number of regions, the pixels are not simulated in the geometry. Instead, starting from the hit position, a specific algorithm coded in one of the user routines calculates run-time the row and column corresponding to the hit pixel, in order to print this information in the output;
- the two PMs are simulated as annular magnets surrounded by an aluminum case (Fig. 3.12a). Since the magnets are only passive elements, the blocks composing each magnet (see Sec. 2.4) have been neglected for simplicity, and the PMs are simulated as homogeneous rings;
- the M28 chips integrated in the four ITR ladders are simulated exactly as the VTX planes (Fig. 3.12b). In addition, the various passive layers composing each ladder have been implemented with the correct material assignment (Fig. 3.12c). Thus, the effects of MCS due to the ladder materials are simulated too;
- the MSD planes are simple silicon parallelepipeds (Fig. 3.12d) since, similarly to pixels, also the microstrips are not implemented in the geometry, and are instead retrieved during the simulation run by a specific algorithm in the user routines;
- contrary to pixels and microstrips, both SCN (Fig. 3.12e) and CAL (Fig. 3.12f) segmentation are reproduced in the geometry file: to each SCN bar (parallelepipeds) and CAL crystal (truncated pyramids) corresponds an individual region.

Since the beginning, it has been decided not to implement in the simulation stage the smearing due to the detector response, but to postpone this step in the analysis phase, in order to have the full MC truth always at disposal. Therefore, no detector efficiencies, pixel clusterization in the pixel chips or other detectors related effect influences the results of FOOT simulations.

The adopted pre-defined physics defaults, passed to the input file through the card `DEFAULTS`, is `PRECISIO`, which is recommended for precision simulations (Fig. 3.13). The `PRECISIO` physics settings include the activation of:

- transport of electrons, positrons and photons
- Rayleigh scattering and inelastic form factor corrections to Compton scattering and Compton profiles
- detailed photoelectric edge treatment and fluorescence photons
- low-energy neutron transport to thermal energies
- fully analogue absorption for low-energy neutrons
- particle transport minimum threshold set at $100\,\mathrm{keV}$, except neutrons ($1 \times 10^{-5}\,\mathrm{eV}$)
- MCS threshold at minimum allowed energy

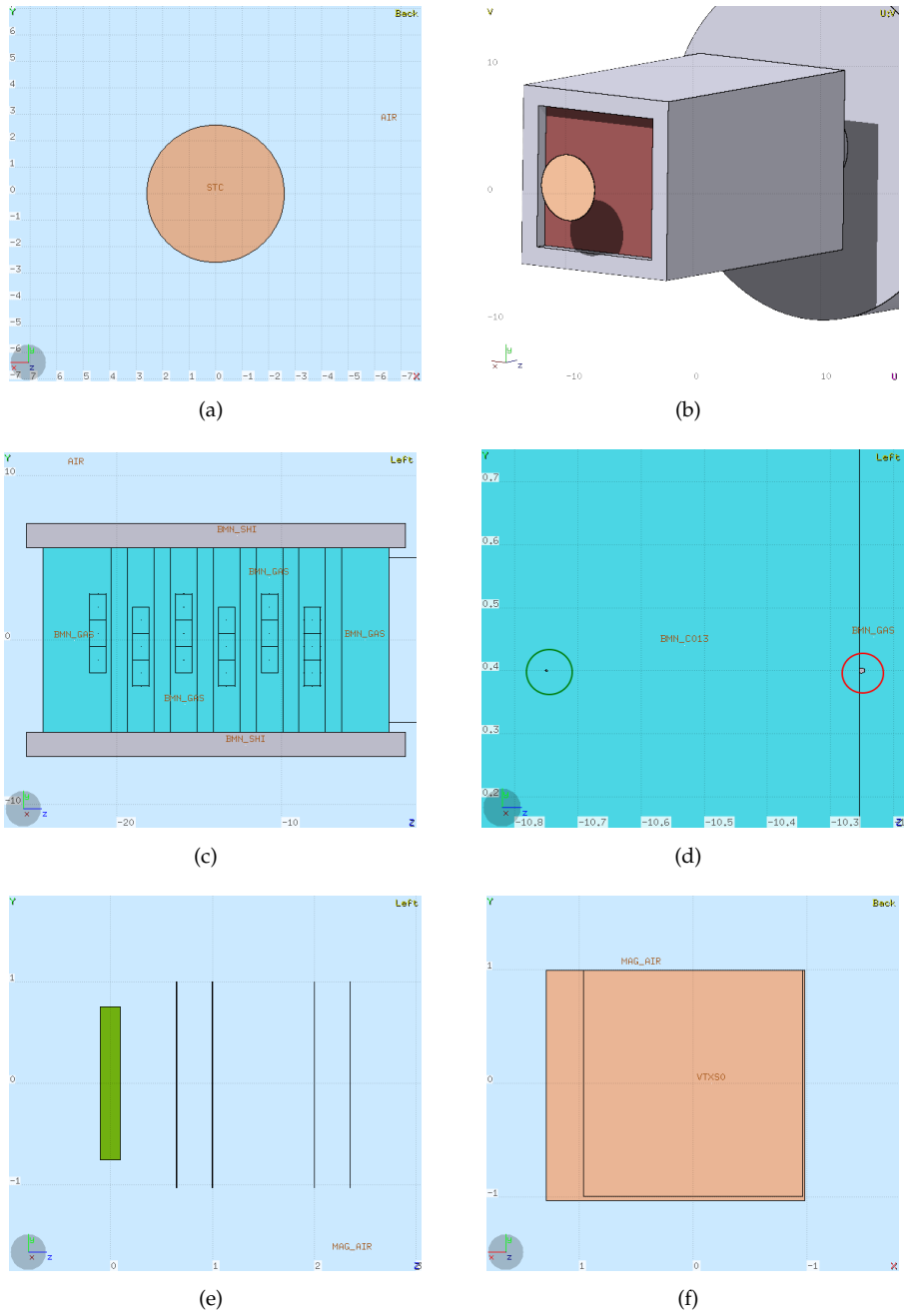

Fig. 3.11: (a) $x - y$ view of the STC. (b) 3D view of STC and BMN. (c) $y - z$ view of the BMN; the cell structure can be seen. (d) Detail of a BMN cell: one of the cathode wires (circled in red) and in the center of the cell the anode wire (circled in green) are visible. (e) $y - z$ view of the target and the four VTX planes. (f) $x - y$ view of one of the VTX planes; the inner square represents the sensitive region. All the images are obtained with Flair GeoViewer.

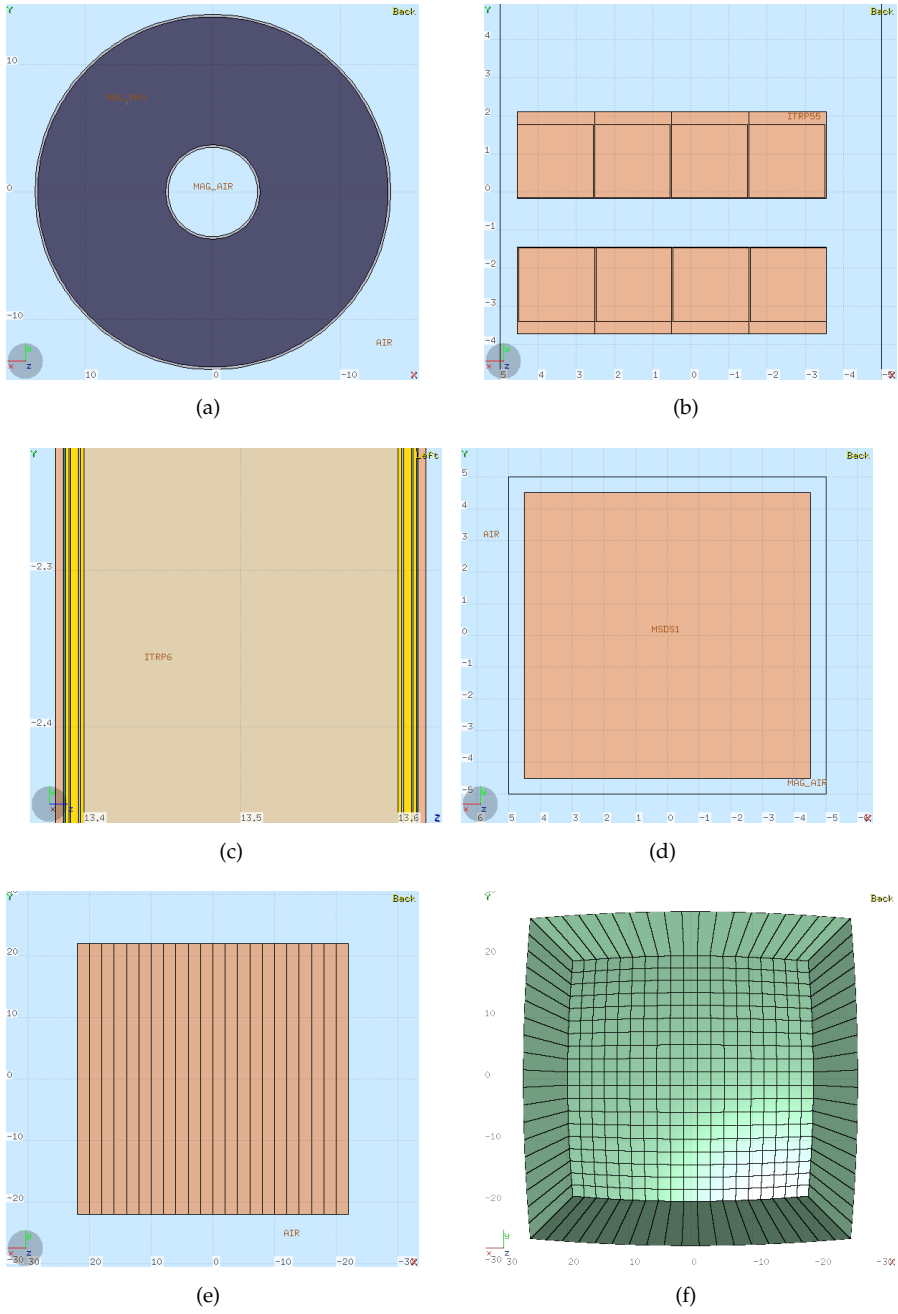

Fig. 3.12: (a) $x - y$ section of the the first magnet. (b) $x - y$ view of two ITR layers. (c) $x - y$ view of one of the MSD planes; the cell structure can be seen. (d) $y - z$ section of the scintillator and the calorimeter; the two orthogonal layers of scintillator bar can be seen. (e) $x - y$ view of the first scintillator bars layer. (f) $x - y$ 3D view of the calorimeter. All the images are obtained with Flair GeoViewer.

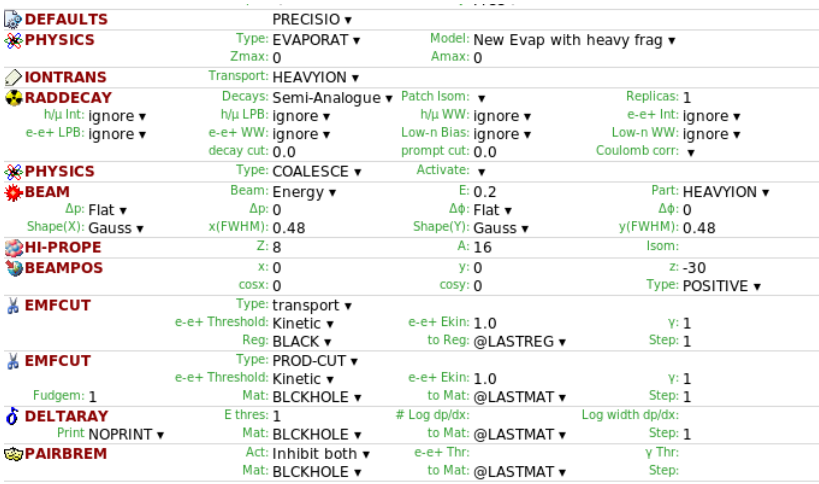

Fig. 3.13: Physics cards implemented in FOOT input file.

- δ-rays production on with threshold $100\,\mathrm{keV}$
- restricted ionization fluctuations activated for hadrons, muons and EM particles
- heavy particle e^+e^- pair production with with the minimum threshold equal to $2m_\mathrm{e}$
- heavy particle Bremsstrahlung with photon production above $300\,\mathrm{keV}$
- heavy fragment transport

However, the low energy thresholds for photons and electrons production led to very long computing times and huge output files (see Sec.'3.4). To overcome this problem at this preliminary experimental stage, an increase of production and transport thresholds for photons and electrons is a reasonable compromise. In fact, at present the analysis is focused on fragments identification performances. Therefore the production and transport thresholds for photons, electrons, δ-ray and e^+e^- pairs have been set to $1\,\mathrm{GeV}$ (Fig.3.13). This allowed to considerably speed up the simulation runs and shrink the output files to an acceptable size (see Sec.'3.4).

At present, primaries are simulated as a beam along the z direction, with a FWHM in the transverse directions miming a real therapeutic beam. However, the ion source parameters will be adjusted in the future to simulate the real beam of a selected facility.

3.2.2 Magnetic field

In this work, a particular attention has been devoted to the management of the magnetic field. Ing. Sanelli, from Frascati Laboratories, designed the PMs layout and provided a map produced with a dedicated magnetic field simulation software. The map consists of an ASCII file reporting in a table the three components of the field in a 3D mesh of points evenly spaced by $0.5\,\mathrm{cm}$ along each direction. This map will be later substituted by an experimentally measured map once the magnets will be produced by the manufacturer.

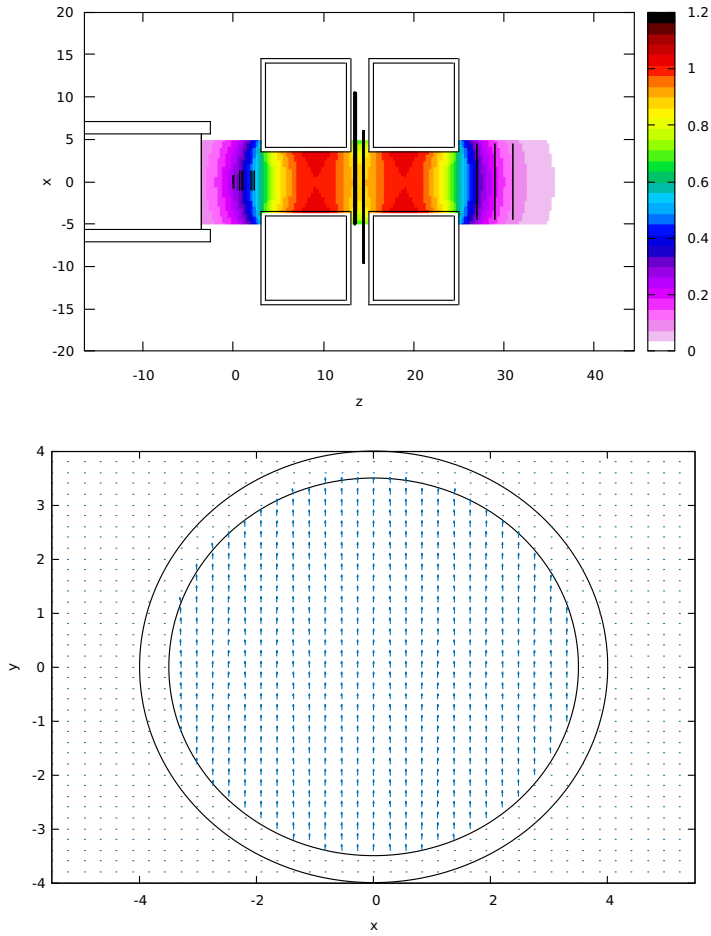

Fig. 3.14: Top panel: magnetic field intensity in the $z - x$ plane. Bottom panel: magnetic field vectors in the $x-y$ plane passing through the middle of the first magnet; the inner circle represents the magnet internal radius. Both the plots have been obtained by means of Flair.

As seen in Sec. 3.1.2, a FLUKA standard input can handle only a constant magnetic field, therefore to manage more complex fields, as in this case, a dedicated user routine has been developed. It is capable of reading the map and of interpolating run-time the magnetic field to calculate its components at any point (see Sec. 3.3 for more details). Hence, at each particle step, the code can retrieve the magnetic field acting on that particle in that precise point (Fig. 3.14).

In FLUKA, a default accuracy of $0.05\,\mathrm{cm}$ is adopted in generic inputs for particles step-size (*i.e.* the distance between two subsequent interaction). However, when dealing with very thin detectors ($\sim$tens or hundreds of µm) as the $50\,\mu\mathrm{m}$ thick pixel detectors (VTX and ITR), the default accuracy is not enough, hence it must be increased by the

user. Several solutions have been tested and an accuracy of $0.1\,\mu m$ for the step-size and $0.1°$ for the maximum angle provided a suitable tracking accuracy and a sustainable CPU time consuming (see Sec. 3.4).

3.2.3 The MakeGeo software

After an initial phase when all the geometry or simulation parameters changes were implemented by hand, *i.e.* by directly modifying the `inp` and/or `geo` files, the necessity of writing the input in a more automated way became evident due to the increasing complexity of the geometry. Moreover, to investigate the detector performances, several simulations differing slightly one from another were often required: for example, to study the particle reconstruction performances we tested different setup configurations with the detectors placed at different distances from the target, and therefore each body used to define the regions associated to a certain detector should have been consequently modified to move them in the geometry space. Performing such modifications by hand is impractical, excessively time-consuming and therefore not an efficient method. To speed up, simplify and automate the process, a first version of an in-house C++ software, named `foot_geo`, was developed. It inherited the structure of an analogous software developed for the FIRST experiment, which was hugely modified, expanded and adapted to FOOT requirements. Starting from a basic input file and an header file containing some user defined values of detectors dimensions, positions, distances and other customized parameters, this software was capable of modifying the `inp` file and creating *ex novo* the correct `geo` file containing the geometrical description of the entire FOOT setup in a FLUKA readable format.

In the last year a great effort have been made to develop and upgrade the reconstruction software, called Software for Hadrontherapy Optimization Experiment (SHOE). It will run both on simulated and experimental data to reconstruct the particle tracks and the events. In particular, the track reconstruction will be performed by means of a Kalman filterFOOT algorithm implemented in the external open source GENFIT library (Rauch & Schlüter 2015), which takes into account magnetic fields and MCS inside crossed materials. Therefore, geometry, materials and magnetic field characterizing the simulated FOOT setup are required not only by FLUKA to produce simulated data, but also by the reconstruction software to evaluate the MCS and to reconstruct the hits position. Of course, geometry, materials and magnetic field simulated with FLUKA must be identical to the ones used in SHOE. However, while the magnetic map file can be easy read from both FLUKA and SHOE, the logic used by FLUKA to describe geometry and materials is completely different from the one adopted in the reconstruction code by GENFIT, which makes use of ROOT `TGeometry` classes.

At first, the ROOT geometry needed by SHOE was built independently from the FLUKA one: the first was implemented in order to accurately reproduce the second, but in a separate and independent stage. This method proved to be quite time consuming, as well as error prone because of the non-negligible probability of introducing mismatches between the simulated and the reconstructed geometries, since they have been often modified due to testing purposes.

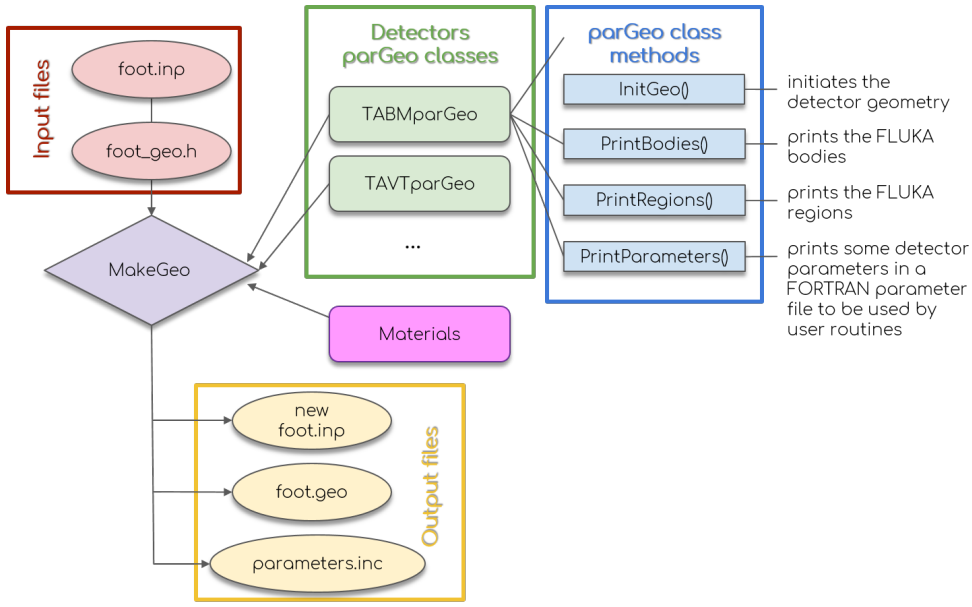

Fig. 3.15: Block diagram of the `MakeGeo` software.

To overcome this issue and improve the efficiency of the geometry implementation process, new *ad hoc* SHOE classes have been developed. The `parGeo` classes, one for each detector (Fig. 3.15, green boxes), take care of producing the geometry both in FLUKA and in ROOT format (see App. B). These classes create the `TGeometry` *volumes* required to configure each detector. The volumes represent elements of the geometry described in a local coordinate frame, and they can be nested one inside the other to produce the desired detector configuration. When inserting a daughter volume inside another volume, a geometrical transformation with respect to its local reference frame must be specified because, when positioned, the daughter volume becomes a node of its container.

For what concerns the materials definition, even if ROOT embeds a quite complete pre-built elements database, we preferred to use exactly the same material definitions used in FLUKA to obtain the best possible matching. To this purpose, another class, called `Materials`, have been developed in the SHOE library to manage the materials: by reading a basic FLUKA input file where all the materials of interest are defined with all their properties and characteristics, this class creates the `TGeoMaterial` and `TGeoMixture` objects which are required by SHOE.

A specific macro, `MakeGeo.cxx` (Fig. 3.15, purple boxes), calls in each detector geometry class the methods `PrintBodies` and `PrintRegions` (Fig. 3.15, blue boxes), which implement the logic to write also the FLUKA geometry, starting from the volumes dimensions created in the `TGeometry` format and transforming the local coordinates in global coordinates. Starting from a basic `inp` file and a parameter header file (Fig. 3.15, magenta boxes) as the `foot_geo` software, this macro therefore produces an executable, `MakeGeo`, which creates the simulation files (`geo`, `inp`) (Fig. 3.15) needed to run FLUKA.

3.3 Building the simulation output

As explained in Sec. 3.1, in FLUKA several built-in estimators are available. The generated output are statistical estimations of the average value of the population corresponding to one of various radiometric quantities. These estimators can be used with no need of writing any line of code.

However, some situations require a customized output, in particular when MC simulations have to produce data to be processed as real experimental data. These situations require an *ad hoc* event-by-event output, especially when many particles are produced in the same event. This is precisely the case of FOOT: the analysis event-by-event, in which fragments originating from the same primary interacting with the target are identified, is crucial to retrieve the production cross sections of the different produced ions.

Moreover, the various detectors composing the FOOT experimental setup provide different types of information (for example the pixel detectors measure the particles position, while the scintillator gives energy release and timing information). Therefore, the output has to be modeled on the detectors characteristics, reproducing the information given by each of them.

Due to these reasons, it has been decided to produce simulation outputs describing the whole history of the produced particles to perform accurate analysis of each event.

Another requirement that the simulation output has to fulfill is that the produced data structure should be easy to handle for all the collaboration members, the most of whom is not familiar with FLUKA. To this purpose, we decided to store the event data of each simulation in a `root` file, which is a format familiar to most people in the FOOT collaboration. Since the FLUKA output is an ASCII text file, a simple portable code, named `Txt2Root`, has been developed to convert it into a `root` file. The output information is therefore stored in TreeBranches that can be easily read by the reconstruction algorithms.

Therefore, FOOT outputs are generated in a two-step approach:

1. basic event generation within FLUKA environment
2. post-processing of events, including a ROOT Tree generation

Another possibility is to directly integrate the production of a `root` file output in the FLUKA user routines. So far, this procedure has not been adopted to avoid portability issues in different computer architectures.

3.3.1 User routines

To produce the FOOT customized and problem-specific output, several FLUKA user routines have been developed. They are based on a user routine package used in previous experimental situations. Aiming to a customized output on the basis of the FOOT analysis requirements, these routines have been deeply revised and modified and also new routines have been introduced to adapt the simulation to the problem. These routines are called in different moments of the run, *i.e.* at the beginning/end of the run or in each event (see Fig. 3.16 for the time scheme), and are configured to produce a customized event-by-event output written in an ASCII file (`*TXT.dat`).

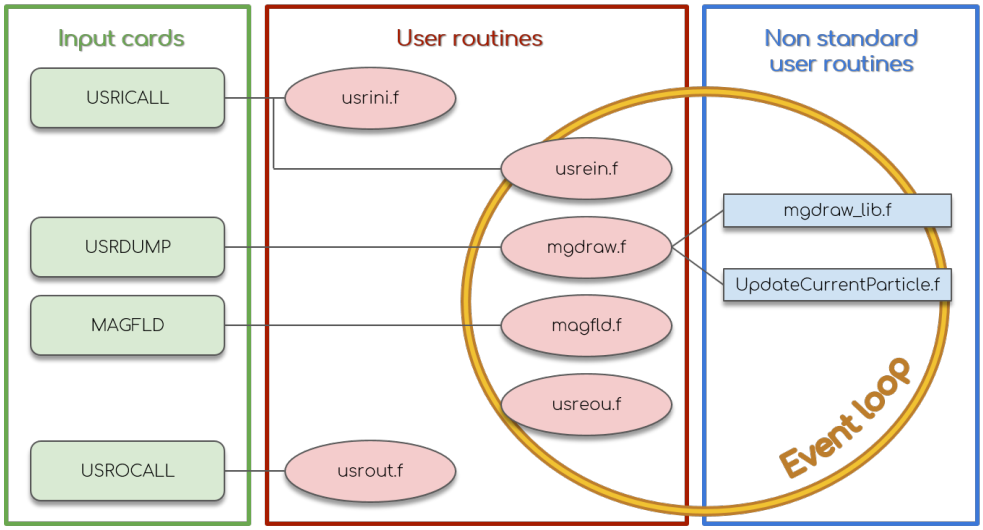

Fig. 3.16: Block diagram of the user routines logic.

At present, the user routines and the auxiliary files required to produce the FOOT simulations output (see Fig. 3.16) are:

- `mgdraw.inc`: this is a custom include file containing the common blocks shared by the other user routines. In FORTRAN, a common block is a portion of memory in which are stored data that can be used in different routines without using arguments. This file, reporting the common blocks declarations, is not a standard FLUKA routine but has been introduced for programming convenience.

- `parameters.inc`: another custom include file containing detectors parameters needed and used by the other user routines. Since these parameters are strictly related to the implemented geometry, to reduce the probability of introducing errors this file is automatically generated when producing the FLUKA geometry with the `MakeGeo` software according to the current geometry.

- `usrini.f`: this file contains the initialization subroutine `USRINI`, which is called at the beginning of the run by the `USRICALL` card in the input file. In this card the meaning of the WHATs is user defined, therefore the calling parameters can provide the `USRINI` subroutine with useful information, such as thresholds, or they can be used as flags to drive the routines actions. In the FOOT input, the `USRICALL` card provides two flags: a debug flag producing, if activated, a verbose output or an event display, and a trigger flag (see Sec. 3.3.2). Since the customized scoring in the detectors is performed on a region basis, the main task of the `USRINI` subroutine is to recognize and store the region names. In fact, each region of the

experimental setup has a double identifier: the first one is its name defined and used by the user, while the second one is a sequential number internally assigned and used by FLUKA. Hence, an algorithm capable of linking the region name to the FLUKA internal number has been implemented in the `USRINI` subroutine. This allow the user to easily recall in the other user routines the regions in which the scoring must be performed.

- `usrein.f`: it contains the `USREIN` subroutine, which is called at the beginning of each event before the sampled primary is transported. In FOOT simulations, it allows the user to initialize the event by zeroing the output arrays of the common blocks declared in the `mgdraw.inc` file.

- `mgdraw.f`: the subroutine `MGDRAW` contained in this file is the core of the output building, since it handles the energy depositions recording. It allows to intercept the transport and the interaction processes at every step. This subroutine is activated by the card `USRDUMP`, and is used to write the output file where all or selected transport events are recorded. Several entries[3] can be found in this subroutine: `SODRAW`, which manage the injection of the primary particle in each event; `MGDRAW`, in which the customized scoring in the detector regions is coded and the energy deposition along each step is calculated; `BXDRAW`, in which the scoring at region crossings is performed; `ENDRAW`, which handles local depositions of particles below threshold; `USDRAW`, where the simulation searches inelastic nuclear interactions in the target or in other regions of interest and the trigger flags are coded.

- `UpdateCurrentParticle.f`: this is not a standard FLUKA user routine. It manages the logic to recognize new created particles and is called by the various entries in `mgdraw.f`.

- `mgdraw_lib.f`: this is not a standard FLUKA user routine, but is a custom service routine for `MGDRAW`. It contains the custom service subroutines that fill the output arrays for every specific detector and for crossing borders.

- `magfld.f`: the subroutine `MAGFLD` is activated by the input card `MGNFIELD` if WHAT(4-6) are set equal to 0. It returns the magnetic field intensity and direction on the basis of the current position and region. In fact, this subroutine is called only if the region where the particle is transported in that moment has a magnetic flag activated in the card `ASSIGNMA`. In FOOT simulation, this routine reads a file containing a magnetic field map and interpolates it at run time when tracking in a region with magnetic field on.

- `usreou.f`: the `USREOU` subroutine contained in it is called at the end of each event, *i.e.* when the primary and all its descendant particles have been transported. In FOOT case, this subroutine implements trigger logic for data output (see Sec. 3.3.2) and writes the output arrays on the output ASCII file at the end of the event.

[3] An entry is a FORTRAN feature allowing a subroutine to have multiple names and argument lists.

- `usrout.f`: it contains the `USROUT` subroutine, which is called at the end of the run by the card `USROCALL` in the input file. It can be used to print customized output.

Several check-points placed in the user routines can write in the `log` file user defined error messages, if any, thus allowing the user to control the correctness of the run.

The desired simulation output can be produced by launching the run together with the executable generated by linking the properly compiled user routines. During the run each routine will be called at the right time (Fig. 3.16), thus ensuring the correct management of the scoring throughout the entire run.

3.3.2 Simulation trigger

To speed up the simulation run and reduce the size of the output file, a trigger logic has been implemented in the user routines, so that only the events satisfying the trigger request are printed in the output file. The user can specify a trigger flag in the `USRICALL` card which, depending on its value, selects one of the available logic channels implemented in the user routines to set the trigger. At present, the available triggers consist in the presence of at least one nuclear inelastic interaction in one or more regions. The most used trigger is the occurrence of the interaction within the target volume, since these are the events of interest for the FOOT experiment. However other possibilities are available, for example interaction in the STC and/or in the BMN to study pre-target fragmentation.

The `USDRAW` subroutine looks for inelastic interactions in different parts of the geometry (detectors, air, target, etc.), activating one or more fragmentation flags according to where the interaction took place. Finally, the subroutine `USREOU` checks the correspondence between the fragmentation flag and the trigger flag and the current event is printed if it satisfies the requested trigger, otherwise it is discarded.

When simulating, for example, a $200\,\mathrm{MeV/u}$ $^{16}\mathrm{O}$ impinging on a C_2H_4 target, the target trigger is accomplished in about 1.15% of the events (see Sec. 4.2). Hence, this allows to considerably reduce the final size of the output file.

However, in the future, simulations recording all the events will be produced to investigate other aspects. For example, the zone of each detector lying on the beam axis will be heavily exposed to radiation due to all the non-fragmenting beam particles, which will travel almost straightly across the whole apparatus. Possible consequences due to this effect will be studied via full MC simulations.

3.3.3 Output structure

The ASCII file produced by the FLUKA simulation can be converted into a ROOT ntuple by means of a dedicated software, `Txt2root`. The information stored in the ASCII file are transferred by this software into easily accessible ROOT `TTree` branches.

The array output for each event can be divided in blocks:

- *Particles (or tracks) block*. In this block the number of particles produced in that event is reported as well as some quantities for each particle, such as its type, mass,

Variable name	Meaning
TRpaid	index in the part common of the particle parent
TRcha	charge
TRbar	barionic number
TRreg	region where the particle is born
TRfid	FLUKA code for the particle
TRix, TRiy, TRiz	production position of the particle
TRfx, TRfy, TRfz	death position of the particle
TRipx, TRipy, TRipz	production memontum of the particle
TRfpx, TRfpy, TRfpz	death momentum of the particle
TRmass	mass
TRtime	production time

Tab. 3.1: Particle (or tracks) block.

Variable name	Meaning
VTXid	position of the particle responsible of the release in the particle block
VTXilay	layer number
VTXirow	row number
VTXicol	column number
VTXxin, VTXyin, VTXzin	position of the first energy release
VTXxout, VTXyout, VTXzout	position of the last energy release
VTXpxin, VTXpyin, VTXpzin	momentum at the last energy release
VTXpxout, VTXpyout, VTXpzout	momentum at the last energy release
VTXde	released energy
VTXtim	time at the first energy release

Tab. 3.2: Example of detector block: the vertex block.

Variable name	Meaning
CROSSid	position of the crossing particle in the particle block
CROSSnreg	no. of region in which the particle is entering
CROSSnregold	no. of region from which the particle is leaving
CROSSx, CROSSy, CROSSz	position of the boundary crossing
CROSSpx, CROSSpy, CROSSpz	momentum at the boundary crossing
CROSSm	mass of the crossing particle
CROSSch	charge of crossing particle
CROSSt	time of the boundary crossing

Tab. 3.3: Crossings block.

Trigger	e^- and γ thresholds	Registered events	Mean CPU time per primary [s]	ASCII output file size [Mb]	ROOT output file size [Mb]
Inelastic interaction in target	1 GeV	1126	1.140E-02	169	42
No trigger	1 GeV	1×10^5	1.256E-02	5221	1344
Inelastic interaction in target	100 keV	1126	1.015E-01	785	230

Tab. 3.4: CPU time and memory usage for runs with different trigger and e^- and γ production thresholds. In each run, 1×10^5 have been simulated. The used processor is an Intel(R) Core(TM) i7-8700K CPU @ 3.70GHz.

charge, production position and momentum, etc. In Tab. 3.1 an overview of the quantities stored in the particle block for each particle in each event is reported.

- *Detector blocks*. For each event there are several detector blocks, each one corresponding to one of the detectors in the FOOT setup. In these blocks the information about the single detectors output and about energy releases are saved. Blocks corresponding to different detectors differ slightly from one another because, as well as general quantities, they contain also information specific of each detector and usually related to the detector segmentation. So, for example, in case of the VTX detector, the layer number, the row and the column corresponding to the hit pixel are reported (Tab. 3.2). Every release described in these blocks can be linked to the particle that produced it through a specific pointer variable (for example `VTXid` in case of the VTX detector) which matches the energy release in the detector block and the responsible particle in the particle block. This allows the user to retrieve all "MC truth" information about that particle.

- *Crossings block*. The last block contains information about the particle that cross different regions of the setup, both active and inactive (Tab. 3.3). Also in this case the particle "MC truth" data related to a specific crossing can be retriever through a specific linking variable as in detector blocks.

3.4 Time and memory usage

To evaluate detector performances a minimum reasonable number of simulated primaries is about 1×10^7. Since it is impractical to make a single long simulation, the best solution is to produce k parallel and statistically independent runs. The number of runs k depends on the amount of available CPU cores, and the number of primaries/run depends on CPU speed as well as user flavor. It is advisable that run duration does not exceed a few hours, in order to avoid useless waste of time in case something goes wrong during the simulation. A practical way, is to replicate the input file in several copies, each one with a different random seed in the `RANDOMIZE` card, and run them in parallel. A simple in-house code, named `crea_input`, have been developed to accomplish this task.

In Tab. 3.4 the CPU time and the size of both the ASCII and the `root` output files are reported for different trigger conditions and energy cutoff for electromagnetic radiation. As it can be seen, low energy thresholds cause a slow-down of the simulation speed: the average time required for each event, *i.e.* to follow a single primary particle and its daughters, increases of one order of magnitude. The choice of applying a trigger requiring a nuclear interaction in the target region, instead, proves to be highly effective in reducing the output ASCII file of more than one order of magnitude.

CHAPTER 4

Analysis of performances

The FOOT experiment has been designed to study the collision of beams of interest for hadroterapic and radioprotection interest. At present, the main guidance for the development of the electronic setup are the MC simulations produced by means of the FLUKA code. Driven by the analysis of the produced MC samples, the experimental setup has undergone many improvements, aiming to enhance the fragments reconstruction performances.

In this section a preliminary analysis of the electronic setup performances is presented. In Sec. 4.1 an overview of the FOOT reconstruction software in reported. In Sec. 4.2 the procedures and algorithm used to produce "experimental like" data from the MC productions are explained. The strategies, as well as their physical and mathematical basis, adopted to perform the fragment ID are outlined in Sec. 4.3. Finally, the obtained cross sections are reported in Sec. 4.4.

4.1 The analysis software

The FOOT reconstruction software, named Software for Hadrontherapy Optimization Experiment (SHOE), is a ROOT based framework, based on a previous reconstruction software developed at the GSI laboratory within the FIRST collaboration. When the development phase will be concluded, SHOE will be able to perform the full reconstruction of the events obtained from both experimental data and FLUKA simulated samples, which are provided in different input formats: data are given in raw format by the DAQ system (digitized signals) while the simulation output files are in ROOT ntuple format (see Sec. 3.3.3). As initial step, SHOE reads, interprets and converts in a single software-object format both the data and the simulation events, so that the reconstruction chain is the same for both of them. The reconstruction process is structured in a two step procedure:

1. in the fist step, named *Level0*, experimental and simulated data are processed to produce *Hit*, *Cluster* and *Track* objects. These will be obtained either from experimental data by decoding the signals collected during the data acquisitions and by applying the detectors calibration constants, or from simulated events processed by specific algorithms which apply the required scaling factors, resolutions and efficiencies. In case of FLUKA simulated data, also the MC truth information is kept

in the event output in order to allow efficiency and resolution studies. At present, the *Hit*, *Cluster* and *Track* objects building is still under development and different pattern recognition approaches are currently investigated.

The track reconstruction in magnetic field is based on a Kalman filter algorithm. The Kalman filter is an effective technique used to estimate the state of a system by combining the output of sensors and affected by some kind of noise. It is commonly employed for track fitting, to retrieve particles position, momentum and trajectory. The state of an ion track at any given surface of one or more detectors can be described by a *state vector* with five parameters. The Kalman filter is based on the succession of alternating phases:

- the *prediction step*, in which the current state vector is extrapolated to the following detector surface or sensor, and the noise due to multiple scattering and the energy loss are taken into account;
- the *filter step*, in which the new state vector thus obtained is improved by using a weighted mean of the measurements.

In this way, the Kalman filter gives the mean value of the state estimate and the covariance matrix of its error. SHOE makes use of the Kalman filter implemented in the external GENFIT library (Rauch & Schlüter 2015). SHOE is fully interfaced with GENFIT and will provide both the primary particles reconstruction, performed using the BMN hits and needed for inverse kinematics reconstruction purposes, and the fragments track reconstruction, evaluated combining the VTX, ITR and MSD hits. Finally, by extrapolating the reconstructed track a matching with the SCN and CAL hits is performed.

2. in the second step, called *HighLevel*, the objects built from the different detectors will be combined to achieve the final global event reconstruction. The different fragments, as well as the primary beam particle, will be identified and their track will be reconstructed, providing the necessary input for the cross section evaluations. Since at present the implementation of the Level0 is still ongoing, this step is being developed independently from the first one: the "true" tracks selected from the MC truth are in fact fed directly to the analysis code, in order to perform the preliminary tests on fragment reconstruction performances.

A scheme of the SHOE structure is depicted in Fig. 4.1.

In this work, the preliminary version of the *HighLevel* analysis code has been developed. Its structure, based on ROOT framework an C++ classes, has been designed to be easily integrated in the SHOE chain after the *Level0*. In this code, no pattern recognition algorithm has been implemented, because this procedure will be integrated in the *Level0* to identify particle tracks. The simulated tracks, each one consisting of a series of "hits" for each detector, are therefore reconstructed on "MC truth" basis, since from MC it is possible to retrieve all the hits belonging to the same fragment. The tracks thus reconstructed are then converted to *Track* objects analogue to the ones that will be produced in the *Level0* with all the resolutions applied, and then the analysis chain and algorithms are applied to them.

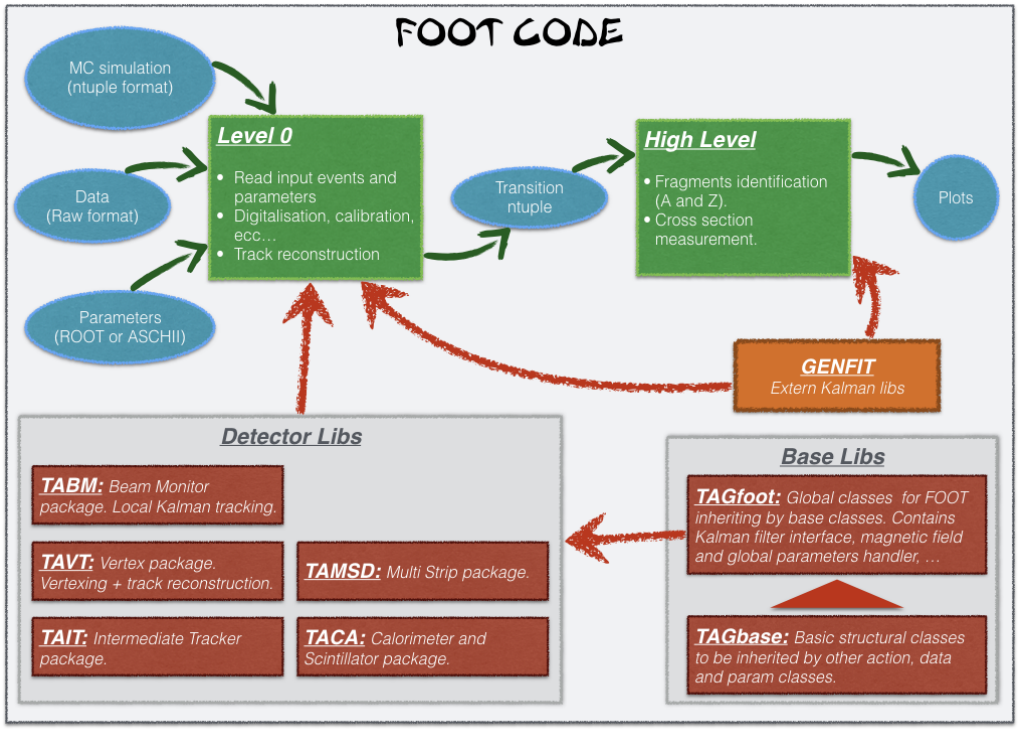

Fig. 4.1: SHOE code diagram.

To identify the fragment, both the charge Z and the mass A have to be determined. The identification can be done on the basis of the time of flight, momentum, kinetic energy and energy release measurements obtained from the FOOT detectors. Therefore, only the particles tracked down by means of the magnetic spectrometer and measured by both SCN and CAL have been included in this analysis.

4.2 Fragments analysis

In this work different simulations have been analyzed, each one characterized by a different combination of beam energy and target material (Tab. 4.1). The simulated setup is the one outlined in Chap. 2 and Chap. 3 (version 14). In the simulations with $700\,\mathrm{MeV/u}$ primary ion beams the setup has been modified as described in Sec. 2.4: both the SCN/CAL block and the magnetic spectrometer have been further shifted along the beam axis direction to gain a larger lever arm for the time of flight and momentum measurements.

The simulated target thickness is of $2\,\mathrm{mm}$ in all the simulations reported in Tab. 4.1, independently from the target material. As expected, the fragmentation rate in the target region is higher in carbon targets due to the higher density with respect to polyethylene ($2.26\,\mathrm{g/cm^3}$ and $0.94\,\mathrm{g/cm^3}$ respectively). However, in the real experiment different

Beam particle	Beam energy [MeV/u]	Target material	Geometry configuration	Fragmentation rate [%]
^{16}O	200	C	Standard	1.94
^{16}O	200	C_2H_4	Standard	1.15
^{16}O	700	C	Elongated	1.97
^{16}O	700	C_2H_4	Elongated	1.21

Table 4.1: Overview of the analyzed simulation files.

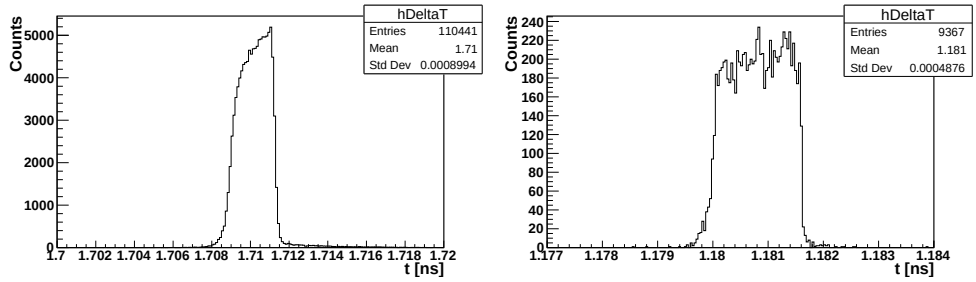

Fig. 4.2: t_{prim} distributions for ^{16}O beams at $200\,\mathrm{MeV/u}$ (left) and $700\,\mathrm{MeV/u}$ (right). The particular shape is due to the spread of the interaction point position in the $2\,\mathrm{mm}$ thick target.

thicknesses of target will be adopted, in order to preserve the same matter thickness ($\mathrm{g/cm^2}$).

As reported in Chap. 2, the FOOT detectors can provide measurements of particles time of flight, momentum, energy loss and kinetic energy. Of course the simulation provides the "true" values, which must be properly smeared to reproduce the experimental measurements. In the following, the procedures employed to calculate experimental-like values of time of flight, momentum, energy loss and kinetic energy are presented.

Time of flight (TOF). In FLUKA simulations, in each event the zero time is the time when the primary is injected in the simulated geometry. To reproduce the procedure that will be adopted with the experimental data, the time of flight is calculated by subtracting the start time measured by the STC, t_{STC}, to the stop time measured by the SCN, t_{SCN}. The resulting time, however, includes also the time it takes the primary to travel from the STC to the target, t_{prim}, that has to be subtracted as well. The t_{prim} distribution has been evaluated via MC simulation (as an example, the t_{prim} distributions for a ^{16}O primary beam at 200 and $700\,\mathrm{MeV/u}$ are shown in Fig. 4.2). Its spread is due to the stochastic nature of the interactions of the primary particles in the crossed media (plastic of the STC, air and the BMN gas) and to the interaction point within the $2\,\mathrm{mm}$ thick target. In this work, the t_{prim} mean value, $\bar{t}_{prim}$, is used to reconstruct the fragments time of flight. Therefore, the time of flight has been obtained as follows:

$$TOF = t_{SCN} - t_{STC} - \bar{t}_{prim} \tag{4.1}$$

The time of flight resolution has been obtained from the performance measured during the experimental test (see Fig. 2.12b in Sec. 2.4), where the coincidence time reso-

lution has been evaluated with two SCN bars. The time resolution scales with the inverse of the energy released in the SCN, which according to Eq. 1.5 increases with the charge of the particle. For C ions, a time resolution of 30-40 ps, almost independently of the released energy, has been estimated. Due to the lower energy loss in the SCN, the resolution for protons is a factor 3 higher: it ranges between 100 and 180 ps depending on the energy. The electronic setup main goal is to measure heavier fragments, for which, according to experimental findings, the time resolution would not reasonably present a strong dependence on the energy loss. Therefore, to reproduce this experimental trend, in this work the time measurement resolution, $\sigma(t_{SCN})$, has been empirically parametrised as a function of the particle charge:

$$\sigma(t_{SCN}) = a_1 + \frac{a_2}{Z} \tag{4.2}$$

where $a_1 = 40\,\mathrm{ps}$ and $a_2 = 60\,\mathrm{ps}$ are parameters determined to fit experimental results. On average, time of flight of fragments produced for example by a ^{16}O beam at $200\,\mathrm{MeV/u}$ is about 6 ns (Fig. 4.3), therefore the relative resolution is less than 1% for carbon ions and about 1.5% for protons.

The STC, instead, is still in a design phase and therefore no experimental data on its time measurement resolution are available yet. However, the aim is to achieve a time resolution comparable to the SCN one, in order to maintain a good time of flight resolution. Hence, in this work the same time resolution experimentally determined for the SCN has been also assumed for the STC.

The resolution on the t_{prim} estimation, $\sigma(t_{prim})$, has been obtained from the t_{prim} distribution and, according to Fig. 4.2, it resulted to be $<$ ps, well below the STC and SCN resolutions, so that in can be neglected. Therefore, the final resolution on the time of flight measurement is

$$\sigma(TOF) = \sqrt{\sigma^2(t_{SCN}) + \sigma^2(t_{STC})} = \sqrt{2}\,\sigma(t_{SCN}) \tag{4.3}$$

Consequently, for C ions the time of flight resolution is $\sigma(TOF) \simeq 70\,\mathrm{ps}$, while for H ions $\sigma(TOF) \simeq 140\,\mathrm{ps}$. The trend of time of flight resolution as a function of the particle charge is reported in Fig. 4.4

The particle velocity in c units, β, can be obtained from the time of flight as follows:

$$\beta = \frac{1}{c}\frac{L}{TOF} \tag{4.4}$$

where L is the total distance traveled by the particle from the production point to the entrance face in the SCN. Due to both MCS and the magnetic field effect, the particle trajectory is not a straight line. In particular, the magnetic field bends the particle trajectory according to its charge and momentum. In this study, L has been obtained by approximating the particle real trajectory to the sum of several consecutive segments, each one connecting the intersection points between two subsequent region boundaries and the particle trajectory. In the future, this approximation will be dismissed in favor of a more accurate estimation obtained by means of the Kalman filter, which at present tracks the particles from the VTX to the MSD, while the extrapolations to the target on one side

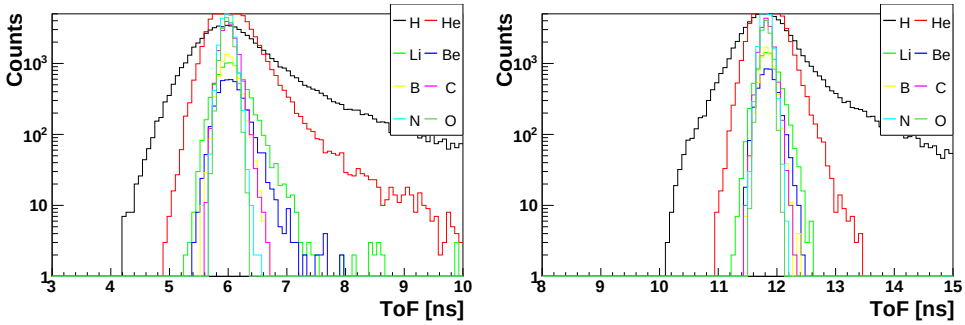

Fig. 4.3: Time of flight distributions for different ions produced by a ^{16}O beam at $200\,\mathrm{MeV/u}$ (left) and at $700\,\mathrm{MeV/u}$ (right) impinging on a $2\,\mathrm{mm}$ thick polyethylene target. The higher values of the time of flight at $700\,\mathrm{MeV/u}$ are due to increased distance between the target and the SCN, the latter being shifted upstream for high energy measurements as reported in Sec. 2.4.

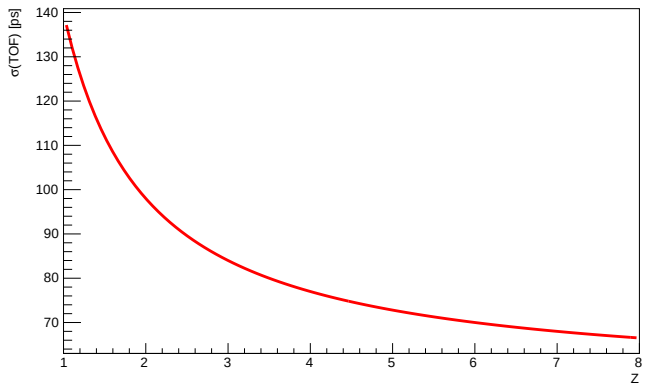

Fig. 4.4: Time of flight resolution applied to simulated data.

and the SCN on the other are not implemented yet. The β distributions are reported in Fig. 4.5 for lithium and carbon fragments produced by a ^{16}O beam at $200\,\mathrm{MeV/u}$ and at $700\,\mathrm{MeV/u}$. It can be noticed the a broader distribution for lithium with respect to proton, due to its wider production energy spectrum.

In this work, the resolution $\sigma(L)$ has been neglected, because it is expected to be negligible with respect to the other quantities. Therefore the β resolution is:

$$\begin{aligned}\sigma(\beta) &= \frac{\partial\,\beta}{\partial TOF}\,\sigma(TOF) = \\ &= -\frac{1}{c}\,\frac{L}{TOF^2}\,\sigma(TOF)\end{aligned} \tag{4.5}$$

Momentum (p). The particles momentum has been retrieved from the generation momentum, to which a proper resolution have been applied (Fig. 4.6). The momentum resolution is driven by few factors: the MCS scattering in the matter, the magnetic spectrom-

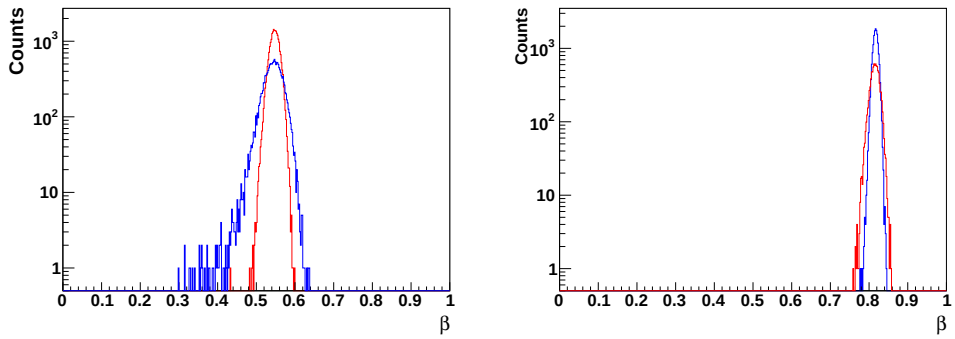

Fig. 4.5: β distributions of lithium (blue) and carbon (red) fragments produced by a ^{16}O beam at $200\,\mathrm{MeV/u}$ (left) and at $700\,\mathrm{MeV/u}$ (right) impinging on a $2\,\mathrm{mm}$ thick polyethylene target.

eter detectors resolution and the magnetic field intensity and spatial extension. Given a certain magnetic field, the MCS contribution decreases as the particle energy an mass increase. The resolution for a given magnetic field has been evaluated from the results retrieved by means of the Kalman filter application, on the basis of the spatial resolutions of the magnetic detectors spectrometers (few µm for M28 chips and few tens of µm for MSD). The Kalman filter studies proved that the achievable resolution improves with the primary particle energy, and therefore with the fragment momentum, whose mean values increase with the beam energy. This is in fact due to the reduction of MCS effects. Since the momentum of lighter fragments is lower than that of heavier fragments, the resolution for the first ones is slightly worse than that for the second ones. In Fig. 4.7 the momentum relative resolution evaluated with the simulated data and calculated from the generation momentum p_{gen} and the reconstructed momentum p_{reco} as

$$\frac{\sigma(p)}{p} = \frac{p_{gen} - p_{reco}}{p_{reco}} \tag{4.6}$$

is depicted. The figures show that a mean resolution of 4% and 3% can be assumed as a good preliminary approximation for all fragments and for beam energies of $200\,\mathrm{MeV/u}$ and $700\,\mathrm{MeV/u}$ respectively. An improved estimation of the momentum reconstruction will be achieved when the results of the Kalman filter will be directly available to the analysis code. In fact, instead of a mean value, the momentum resolution will be evaluated for each fragment according to its estimated momentum.

In this study, the fragment momenta have been determined by applying a gaussian smearing to the production momenta obtained from FLUKA simulations (Fig. 4.6).

Energy loss (ΔE). The released energy has been reconstructed as the sum of the energy deposited by the same particle in the MSD, ΔE_{MSD} (Fig. 4.8 top), and in the SCN, ΔE_{SCN} (Fig. 4.8 middle):

$$\Delta E = \Delta E_{MSD} + \Delta E_{SCN} \tag{4.7}$$

The ΔE_{SCN} resolution applied has been empirically parametrized as a function of

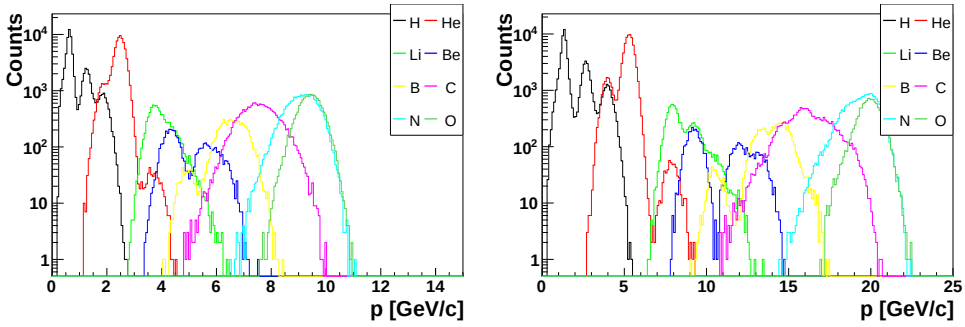

Fig. 4.6: Total momentum distributions for different ions produced by a ^{16}O beam at $200\,\mathrm{MeV/u}$ (left) and $700\,\mathrm{MeV/u}$ (right) impinging on a $2\,\mathrm{mm}$ thick polyethylene target.

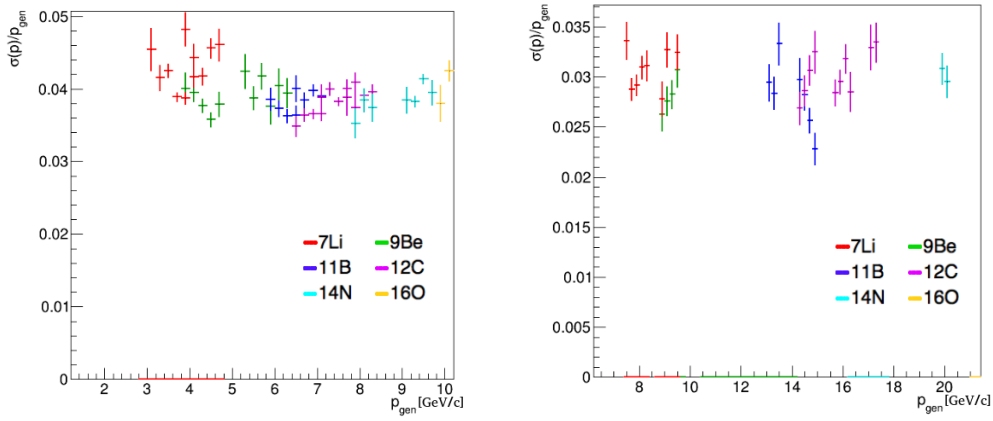

Fig. 4.7: Momentum relative resolution as a function of the generation momentum for some selected fragments produced by $200\,\mathrm{MeV/u}$ (a) and $700\,\mathrm{MeV/u}$ ^{16}O beam

the deposited energy according to the results obtained in experimental tests (Fig. 2.12)a:

$$\sigma(\Delta E_{SCN}) = b_1 + \frac{b_2}{\Delta E_{SCN}} \tag{4.8}$$

where $b_1 = 0.904\,\mathrm{MeV}$ and $b_2 = 18.6\,\mathrm{MeV}$ are parameters determined to fit experimental results. In addition, $\sigma(\Delta E_{SCN})$ has been limited in the range 3-10% according to the experimental findings.

According to the results obtained in an experimental test, the MSD electric noise can be neglected. Hence, the only element contributing to the MSD resolution is the stochastic nature of the energy loss process. Therefore, the final resolution on ΔE measurement coincides with the SCN resolution:

$$\sigma(\Delta E) = \sigma(\Delta E_{SCN}) \tag{4.9}$$

Kinetic energy (E_k). The kinetic energy has been estimated as the sum of the energy deposition in three detectors, *i.e.* MSD, SCN and CAL:

$$E_k = \Delta E_{MSD} + \Delta E_{SCN} + \Delta E_{CAL} = \Delta E + \Delta E_{CAL} \tag{4.10}$$

Since in this analysis only the particles travelling across all the FOOT apparatus up to the CAL have been considered, all the particles fragmenting before reaching the CAL have been discarded. The considered particles, however, can undergo fragmentation inside the CAL crystals. Therefore, to better reconstruct the kinetic energy, ΔE_{CAL} is retrieved not only from the released energy associated to the original fragment but from the sum of all the energy releases in the hit crystal (or crystals, if more than one), as it will be done in experimental data-taking, where crystals are individually read and the energy deposited by different particles is summed up (however more sophisticated crystals cluster algorithms to be used also for experimental data are currently under development). In this way also the energy deposited by charged fragments produced in re-fragmentation processes is, at least partly, considered. In inelastic interactions, however, also neutrons are produced and they may deposit the energy far from the original fragment track or even escape the detector, thus leading to a systematic underestimation of E_k. In Fig. 4.9 and Fig. 4.10 the distribution of the ratio between the reconstructed energy in the CAL and the true production energy of the particles are reported for a ^{16}O beam at $200\,\mathrm{MeV/u}$ and $700\,\mathrm{MeV/u}$ respectively. The tail is due to multiple factors: on one hand, the kinetic energy underestimation is caused by both the neutron production and the invisible energy characteristic of this kind of detector, on the other hand a more sophisticated crystal clustering algorithm could recover part of the non-collected energy. This is particularly remarkable at high primary beam energy (Fig. 4.10), where the tail includes most of the events. In addition the peaks are also shifted at values lower than 1 due to the energy released in other detectors and in air, which can not be experimentally measured. To overcome this problem, a proper experimental energy calibration will be performed for the CAL.

The resolutions associated to MSD and SCN measurements are the ones discussed for ΔE. The energy resolution of a hadronic calorimeter is

$$\frac{\sigma(E)}{E} = \frac{c_1}{\sqrt{E}} \oplus c_2 \tag{4.11}$$

where c_1 and c_2 are detector dependent constants. In particular, the constant term c_2 is related to physics processes (as for example the fluctuation of the invisible energy), electronic noise and detector related issues (intercalibration errors, longitudinal leakage, etc.). The FOOT CAL has been preliminary tested with H, He and C beams at different energies. The energy resolutions obtained are depicted in Fig. 2.13d: the figure shows that $\sigma(E_k)$ is linearly proportional to the particle energy with good approximation, meaning that the resolution is dominated by the constant term. A relative resolution $\sigma(\Delta E_{CAL}) = 1.5\%$ have been estimated and thus applied as a gaussian smearing to ΔE_{CAL} measurements.

The final resolution on E_k measurements is therefore:

$$\sigma(E_k) = \sqrt{\sigma^2(\Delta E_{SCN}) + \sigma^2(\Delta E_{CAL})} \tag{4.12}$$

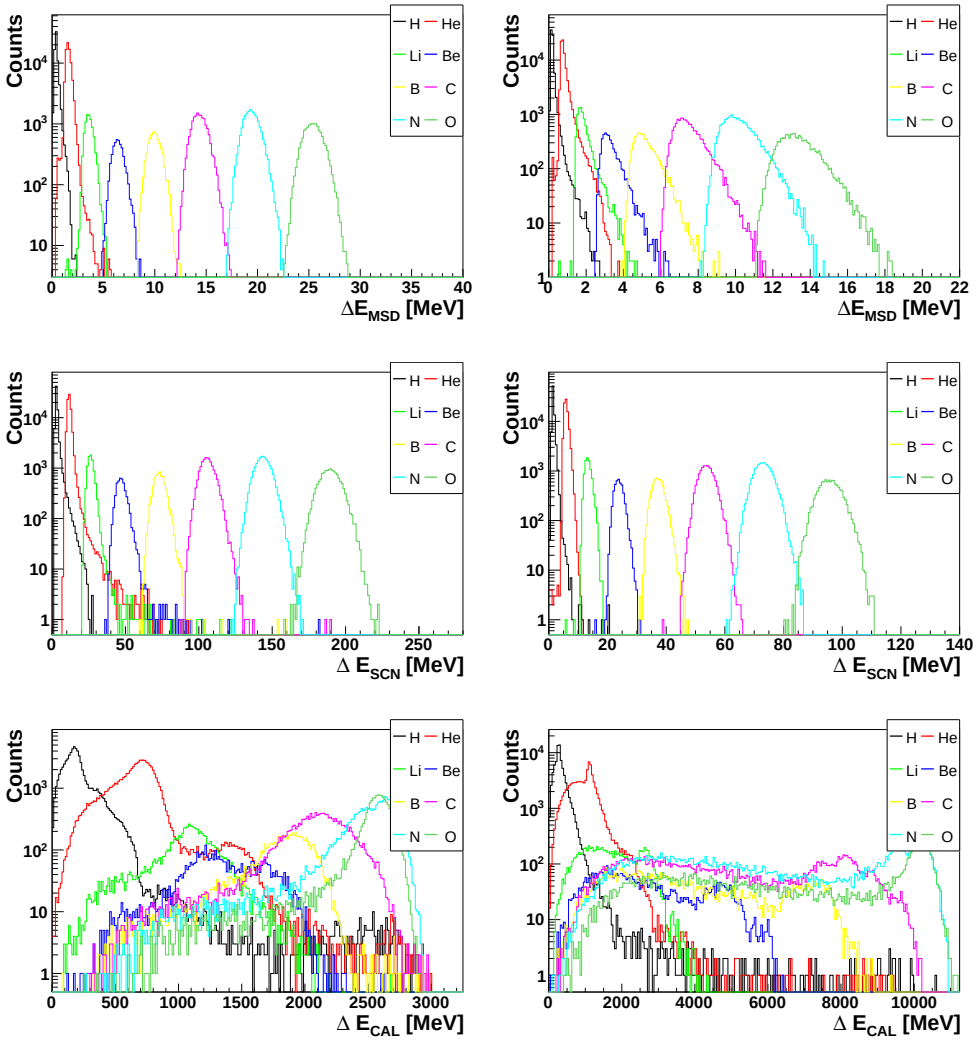

Fig. 4.8: ΔE_{MSD} (top), ΔE_{SCN} (middle) and ΔE_{CAL} (bottom) distributions for different ions produced by a ^{16}O beam at 200 MeV/u (left column) and at 700 MeV/u (right column) impinging on a 2 mm thick polyethylene target.

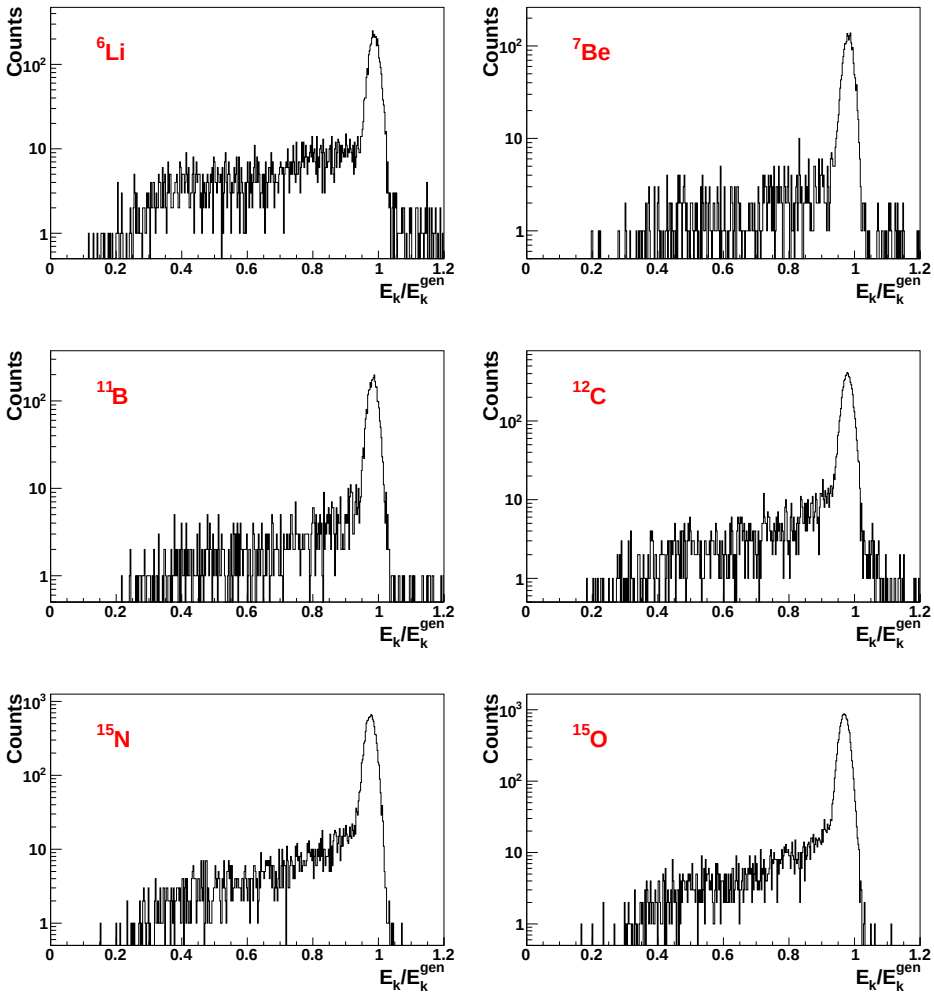

Fig. 4.9: Ratio between the reconstructed and generation kinetic energy for the most abundant isotopes ($Z > 2$) produced by a ^{16}O beam at $200\,\mathrm{MeV/u}$ impinging on a $2\,\mathrm{mm}$ thick polyethylene target.

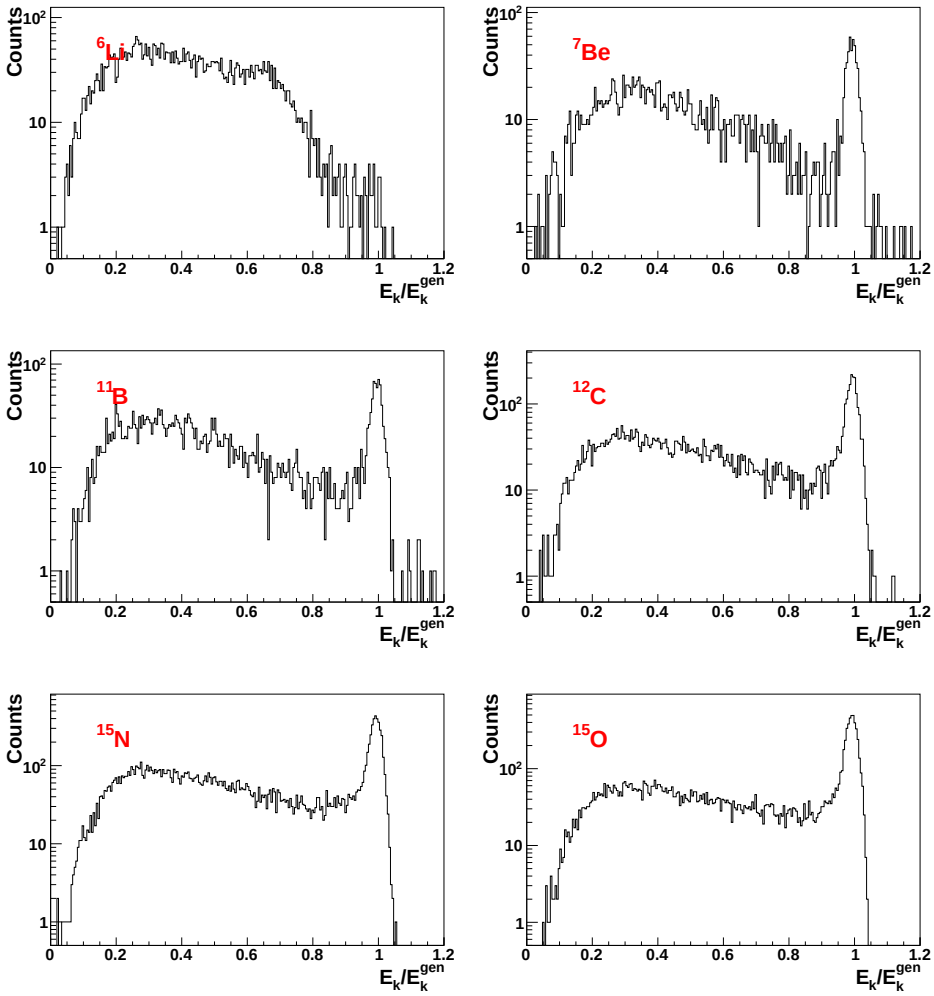

Fig. 4.10: Ratio between the reconstructed and generation kinetic energy for the most abundant isotopes ($Z > 2$) produced by a ^{16}O beam at $700\,\mathrm{MeV/u}$ impinging on a $2\,\mathrm{mm}$ thick polyethylene target. For low Z fragments the kinetic energy reconstruction is particularly affected.

Fragment	Z	$\sigma(Z)$ [%]
H	1.01±0.06	6.26
He	2.02±0.06	3.06
Li	3.03±0.07	2.46
Be	4.05±0.09	2.20
B	5.07±0.10	2.06
C	6.09±0.12	1.97
N	7.12±0.14	1.91
O	8.17±0.15	1.86

Fragment	Z	$\sigma(Z)$ [%]
H	0.98±0.08	7.78
He	1.99±0.09	4.54
Li	3.00±0.11	3.60
Be	4.01±0.12	2.90
B	5.01±0.13	2.61
C	6.02±0.14	2.39
N	7.03±0.15	2.20
O	8.04±0.17	2.05

Table 4.2: Reconstructed Z for fragments generated by a ^{16}O beam impinging on a C_2H_4 target at $200\,\mathrm{MeV/u}$ (left) and at $700\,\mathrm{MeV/u}$ (right) target.

4.3 Fragment identification

The FOOT electronic detector have been designed to identify the fragments produced in inelastic interactions. To this aim, both the atomic and mass number, Z and A must be correctly determined.

4.3.1 Charge identification

In FOOT, the charge identification is performed using both the ΔE and the time of flight measurements (Fig. 4.11). ΔE and time of flight are in fact related to the particle charge according to Eq. 1.5, here again reported (see Sec. 1.2.1 for the symbols meaning):

$$-\frac{\mathrm{d}E}{\mathrm{d}x} = 2\pi N_A\, r_e^2\, m_\mathrm{e}\, c^2\, \rho_m\, \frac{Z_m}{A_m}\, \frac{Z^2}{\beta^2} \left[\ln\left(\frac{2\, m_e, \gamma^2\, v^2\, W_{max}}{I^2}\right) - 2\beta^2 - \delta - 2\,\frac{C}{Z_m}\right] \quad (4.13)$$

In fact, the energy loss per unit path length, $\mathrm{d}E/\mathrm{d}x$, can be obtained as the ratio between ΔE and the total thickness of the three MSD planes and the two SCN layers, while β can be retrieved from the time of flight according to Eq. 4.4. By inverting the Bethe-Bloch equation, therefore, it is possible to retrieve the fragment charge. The charge identification results are depicted in Fig. 4.12.

In Tab. 4.2 the Z estimations with their errors (2-3%) obtained are reported for different beam energies. Similar results have been achieved for the other simulation samples reported in Tab. 4.1.

In the future, a further estimation of the fragments charge will be achieved by means of the evaluation of the clusters size in the pixel detectors, which is in fact related to the charge. To implement an identification algorithm based on cluster size a calibration test with M28 chips is required to establish the correlation between the pixel cluster size and the fragment charge.

4.3.2 Mass number identification

With respect to the Z determination, the evaluation of the mass number A is a challenging task. To this aim, the FOOT setup has been designed to provide redundancy in the

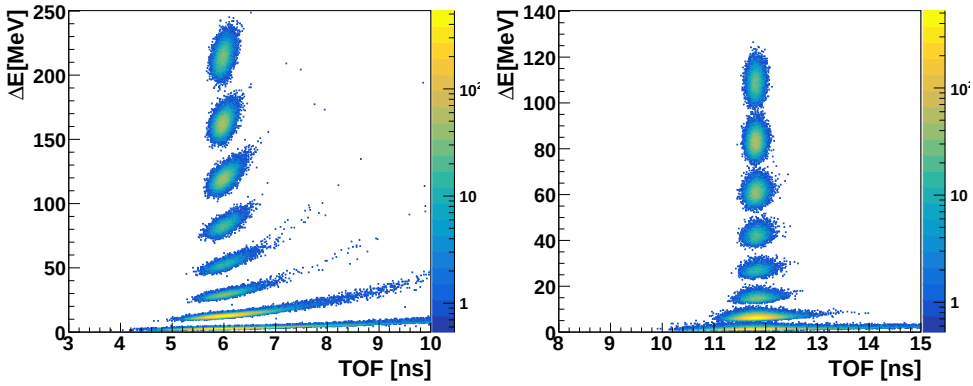

Fig. 4.11: ΔE vs TOF distributions of all the reconstructed fragments produced by a ^{16}O beam at $200\,\mathrm{MeV/u}$ (left) and at $700\,\mathrm{MeV/u}$ (right) impinging on a polyethylene target. The higher value of β at $700\,\mathrm{MeV/u}$ is due to increased distance between the target and the SCN, the latter being shifted upstream for high energy measurements as reported in Sec. 2.4.

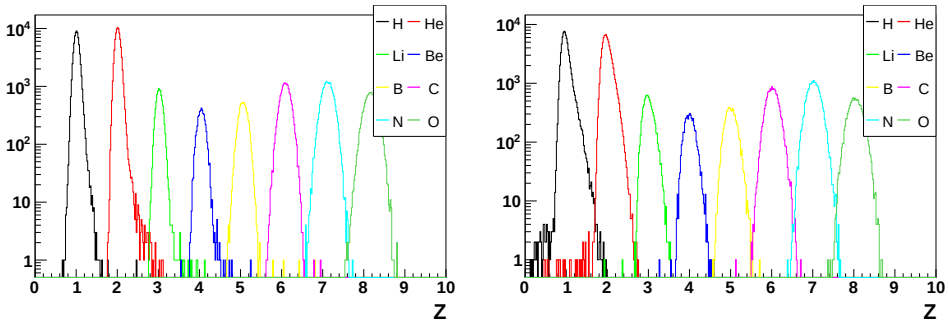

Fig. 4.12: Z distributions of the reconstructed fragments produced by a ^{16}O beam at $200\,\mathrm{MeV/u}$ (left) and at $700\,\mathrm{MeV/u}$ (right) impinging on a polyethylene target.

isotopic determination. In fact, to perform the fragments isotopic identification, the measurements of time of flight, momentum and kinetic energies can be combined in three different ways. Thus it is possible to obtain three different but correlated estimations of the mass number, from this point on called A_1, A_2 and A_3.

1. **Combination of momentum and time of flight measurements**
   The fragment mass m is related to the momentum an velocity according to the expression:

$$p = m\,\gamma\,\beta\,c \tag{4.14}$$

   where

$$\gamma = \frac{1}{\sqrt{1-\beta^2}} \tag{4.15}$$

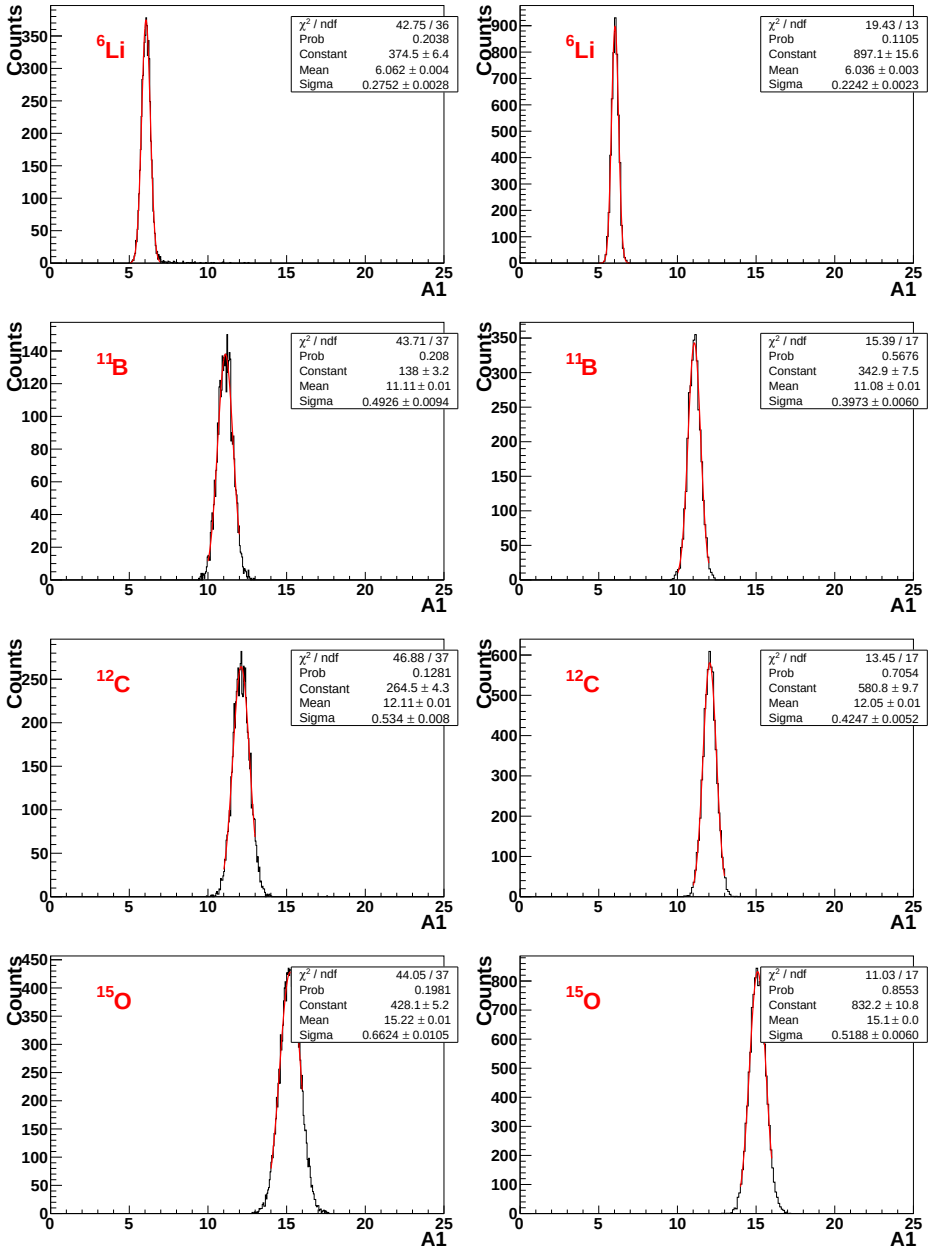

Fig. 4.13: A_1 distributions for the most abundant isotopes of fragments with $Z > 2$ produced by a ^{16}O beam at $200\,\mathrm{MeV/u}$ (left column) and at $700\,\mathrm{MeV/u}$ (right column) impinging on a polyethylene target.

Hence, the mass number can be calculated using p and TOF (or β, according to Eq. 4.4) as follows:

$$A_1 = \frac{m}{\mathrm{u}} = \frac{1}{\mathrm{u}} \frac{p}{\gamma \beta c} \tag{4.16}$$

where $\mathrm{u}=931.494\,\mathrm{MeV}/c^2$ is the atomic mass unit. Consequently its resolution is:

$$\begin{aligned} \sigma(A_1) &= \sqrt{\left(\frac{\partial A}{\partial p}\,\sigma(p)\right)^2 + \left(\frac{\partial A}{\partial \beta}\,\frac{\partial \beta}{\partial TOF}\,\sigma(TOF)\right)^2} = \\ &= \frac{1}{\mathrm{u}} \frac{p}{\beta c} \sqrt{\frac{1}{\gamma^2}\left(\frac{\sigma(p)}{p}\right)^2 + \frac{\gamma^2}{\beta^2}\,\frac{L^2}{c^2\,TOF^2}\,\sigma^2(TOF)} \end{aligned} \tag{4.17}$$

In Fig. 4.13 the distributions of the obtained A_1 values for some selected fragments are depicted. The width of the distributions is due to the resolutions applied to the momentum and to the β (through time of flight).

2. **Combination of time of flight and kinetic energy measurements**
   Starting from the expression for the kinetic energy, which is

$$E_k = (\gamma - 1)mc^2 \tag{4.18}$$

the mass number can be obtained as follows:

$$A_2 = \frac{m}{\mathrm{u}} = \frac{1}{\mathrm{u}} \frac{E_k}{(\gamma - 1)\ c^2} \tag{4.19}$$

$$\begin{aligned} \sigma(A_2) &= \sqrt{\left(\frac{\partial A_2}{\partial E_k}\,\sigma(E_k)\right)^2 + \left(\frac{\partial A_2}{\partial \beta}\,\frac{\partial \beta}{\partial TOF}\,\sigma(TOF)\right)^2} = \\ &= \frac{1}{\mathrm{u}}\,\frac{E_k}{c}\,\frac{\gamma}{\gamma - 1} \sqrt{\frac{1}{\gamma^2}\left(\frac{\sigma(E_k)}{E_k}\right)^2 + \frac{\beta^2\,\gamma^4}{(\gamma-1)^2}\,\frac{L^2}{c^2\,TOF^2}\,\sigma^2(TOF)} \end{aligned} \tag{4.20}$$

In Fig. 4.14 the distributions of the obtained A_2 values for some selected fragments produced by $200\,\mathrm{MeV/u}$ and $700\,\mathrm{MeV/u}$ oxygen beams are depicted. A tail, corresponding to A underestimations is visible in all the reported plot and is due, as previously discussed, to an underestimation of the fragment kinetic energy. The tail is especially pronounced in the case of a $700\,\mathrm{MeV/u}$ oxygen beam. As before, the distributions width is due to the resolutions applied to time of flight and kinetic energy measurements.

3. **Combination of momentum and kinetic energy measurements**
   The particle total energy is the sum of the kinetic and rest energies:

$$E = E_k + mc^2 \tag{4.21}$$

but it can be also described by the energy momentum relation:

$$E = \sqrt{p^2c^2 + m^2c^4} \tag{4.22}$$

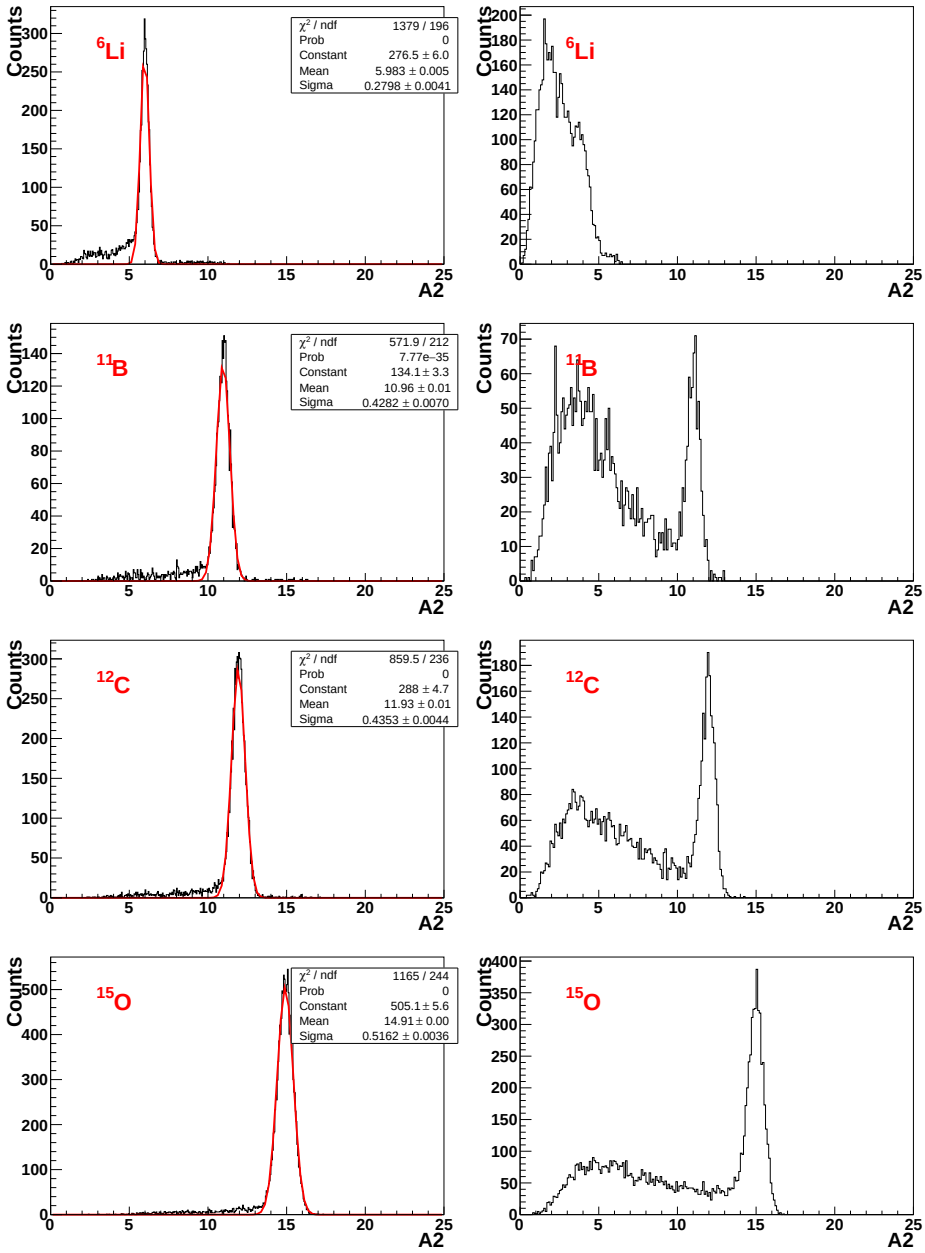

Fig. 4.14: A_2 distributions for the most abundant isotopes of fragments with $Z > 2$ produced by a ^{16}O beam at $200\,\mathrm{MeV/u}$ impinging on a polyethylene target.

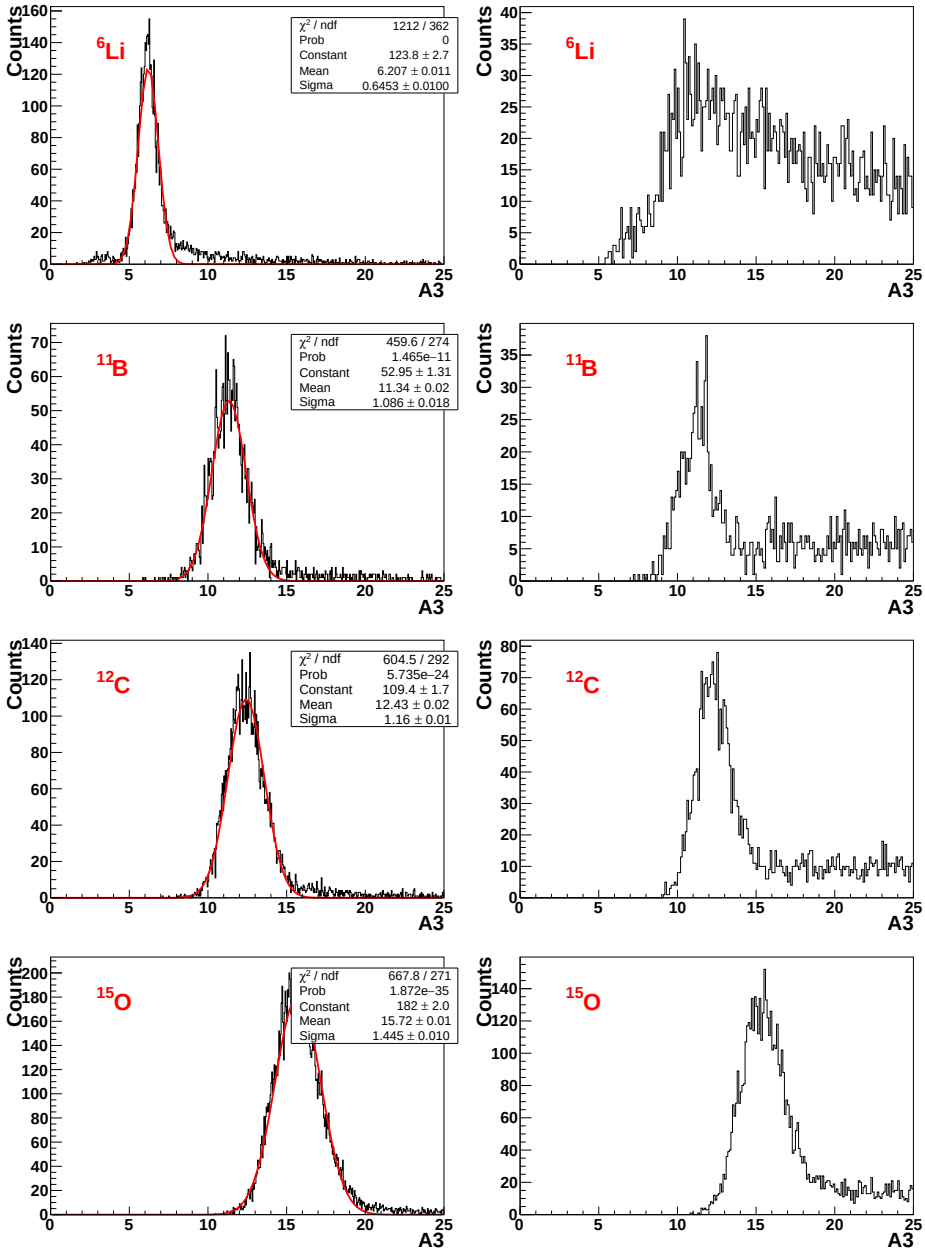

Fig. 4.15: A_3 distributions for the most abundant isotopes of fragments with $Z > 2$ produced by a ^{16}O beam at 200 MeV/u impinging on a polyethylene target.

By combining Eq. 4.21 and Eq. 4.22, the mass can be expressed as

$$m = \frac{p^2c^2 - E_k^2}{2\,c^2\,E_k} \tag{4.23}$$

and therefore the mass number is

$$A_3 = \frac{1}{\mathrm{u}}\frac{p^2c^2 - E_k^2}{2\;c^2\,E_k} \tag{4.24}$$

The resolution on the mass number determination is

$$\begin{aligned}\sigma(A_3) &= \sqrt{\left(\frac{\partial A}{\partial p}\,\sigma(p)\right)^2 + \left(\frac{\partial A}{\partial E_k}\,\sigma(E_k)\right)^2} = \\ &= \frac{1}{\mathrm{u}}\,\frac{1}{E_k}\sqrt{p^4\left(\frac{\sigma(p)}{p}\right)^2 + \frac{\left(p^2c^2 + E_k^2\right)^2}{4\,c^4}\left(\frac{\sigma(E_k)}{E_k}\right)^2}\end{aligned} \tag{4.25}$$

In Fig. 4.15 the distributions of the obtained A_3 values for some selected fragments are depicted. Also in this case tails due to underestimations of the kinetic energy are present and especially pronounced for higher beam energy. Again, the distribution width is related to the momentum and kinetic energy measurements resolutions.

A fit procedure can be finally applied to the three correlated mass number values obtained with the presented method. In this study, to retrieve the best determination of A two different approaches have been tested:

1. **Standard χ^2 minimization**
   This method is based on the minimization of the following function:

$$\chi^2 = \frac{\left(TOF - \overline{TOF}\right)^2}{\sigma^2(TOF)} + \frac{\left(p - \overline{p}\right)^2}{\sigma^2(p)} + \frac{\left(E_k - \overline{E_k}\right)^2}{\sigma^2(E_k)} + \boldsymbol{A}^{\intercal}\,\boldsymbol{B}\,\boldsymbol{A} \tag{4.26}$$

   where TOF, p, E_k, are the reconstructed quantities, $\sigma(TOF)$, $\sigma(p)$, $\sigma(E_k)$ are their uncertainties, $\overline{TOF}$, $\overline{p}$, $\overline{E_k}$ are three out of the four the fit output parameters. $\boldsymbol{A}$ is the vector

$$\begin{pmatrix} A_1 - \overline{A} & A_2 - \overline{A} & A_3 - \overline{A} \end{pmatrix} \tag{4.27}$$

   where A_1, A_2 and A_3 are the reconstructed A values and $\overline{A}$ the fourth output parameter, and $\boldsymbol{A}^{\intercal}$ is its transpose. The matrix $\boldsymbol{B}$ contains the evaluation of the uncertainties associated to A_1, A_2 and A_3, taking into account their correlation, In fact, the matrix $\boldsymbol{B}$ is related to the correlation matrix $\boldsymbol{C}$ as follows:

$$\boldsymbol{B} = (\boldsymbol{C}\,\boldsymbol{C}^{\intercal})^{-1} \tag{4.28}$$

   where the correlation matrix $\boldsymbol{C}$ is:

$$\boldsymbol{C} = \begin{pmatrix} \dfrac{\partial A_1}{\partial TOF}\sigma(TOF) & \dfrac{\partial A_1}{\partial p}\sigma(p) & 0 \\ \dfrac{\partial A_2}{\partial TOF}\sigma(TOF) & 0 & \dfrac{\partial A_2}{\partial E_k}\sigma(E_k) \\ 0 & \dfrac{\partial A_3}{\partial p}\sigma(p) & \dfrac{\partial A_3}{\partial E_k}\sigma(E_k) \end{pmatrix} \tag{4.29}$$

2. **Augmented Lagrangian Method (ALM)**

This method is an algorithm for constrained minimization, which replaces an original constrained problem by a succession of unconstrained sub-problems to find a solution. The ALM method minimizes a Lagrangian function $\mathcal{L}$ expressed by:

$$\mathcal{L}(\vec{x};\boldsymbol{\lambda},\mu) \equiv f(\vec{x}) - \sum_{a=1}^{m} \lambda_a c_a(\vec{x}) + \frac{1}{2\mu}\sum_{a=1}^{m} c_a^2(\vec{x}) \tag{4.30}$$

where $f(\vec{x})$ is the objective function, c_a are the constraints, $\boldsymbol{\lambda}$ is a m-dimension vector of Lagrange multipliers λ_a and μ is the penalty parameter. The last term of Eq. 4.30 is called *penalty term*, and is a function of the constraints weighted by a positive penalty parameter μ. This term disappears when the constraints are null, whereas it becomes large if $c_a \neq 0$ and $\mu \to 0$. Eq. 4.30 is performed iteratively: unconstrained minimization of $\mathcal{L}(\vec{x};\boldsymbol{\lambda},\mu)$ is solved and new $\boldsymbol{\lambda}$ and μ values are selected. This procedure is reiterated to reach the required levels of optimality. In the application of the ALM to the mass identification procedure in FOOT, μ has been set to 0.1, in order to strengthen the constraint. The first term of Eq. 4.30 in this case is:

$$f(\vec{x}) = \frac{\left(TOF - \overline{TOF}\right)^2}{\sigma^2(TOF)} + \frac{\left(p - \overline{p}\right)^2}{\sigma^2(p)} + \frac{\left(E_k - \overline{E_k}\right)^2}{\sigma^2(E_k)} \tag{4.31}$$

while the last two are:

$$\sum_{a=1}^{m} \lambda_a c_a(\vec{x}) + \frac{1}{2\mu}\sum_{a=1}^{m} c_a^2(\vec{x}) = \lambda_1\left(A_1 - \overline{A}\right) + \lambda_2\left(A_2 - \overline{A}\right) + \lambda_3\left(A_3 - \overline{A}\right) + \frac{1}{2\mu}\left(\left(A_1 - \overline{A}\right)^2 + \left(A_2 - \overline{A}\right)^2 + \left(A_3 - \overline{A}\right)^2\right)$$

The results obtained with both the standard χ^2 minimization and the ALM are reported for some selected fragments in Fig. 4.16 and 4.17 respectively. The two methods give similar results for what concerns both the mean value and the error. To improve the relative resolution on A determination, a χ^2 cut can be useful. In fact, as depicted in Fig. 4.18, a long tail at high χ^2 values is visible. The tail, as already explained, is populated by fragments whose kinetic energy has been underestimated. The application of a $\chi^2 < 5$ cut on both the standard χ^2 fit and the ALM fit allows to clean up the obtained distributions (Fig. 4.19). This is particularly useful to separate the different isotopes of the same element (Fig. 4.20 and 4.21), as it will be done in the real experiment where the "MC truth" is not available. As can be seen in Tabs. 4.3 and 4.4, the improvement on the A resolution achievable with a χ^2 cut is negligible, however the cut allows in fact to reject all the events belonging to the high χ^2 tails that would increment the measured yields of the incorrect A values. The achievable resolution ranges between 3% and 4%.

The case of $700\,\mathrm{MeV/u}$ is particularly challenging due to the frequent underestimation of the fragment kinetic energy. A possible solution currently under consideration is to determine the fragment mass number only from the A_1 estimation, which does not present any tail.

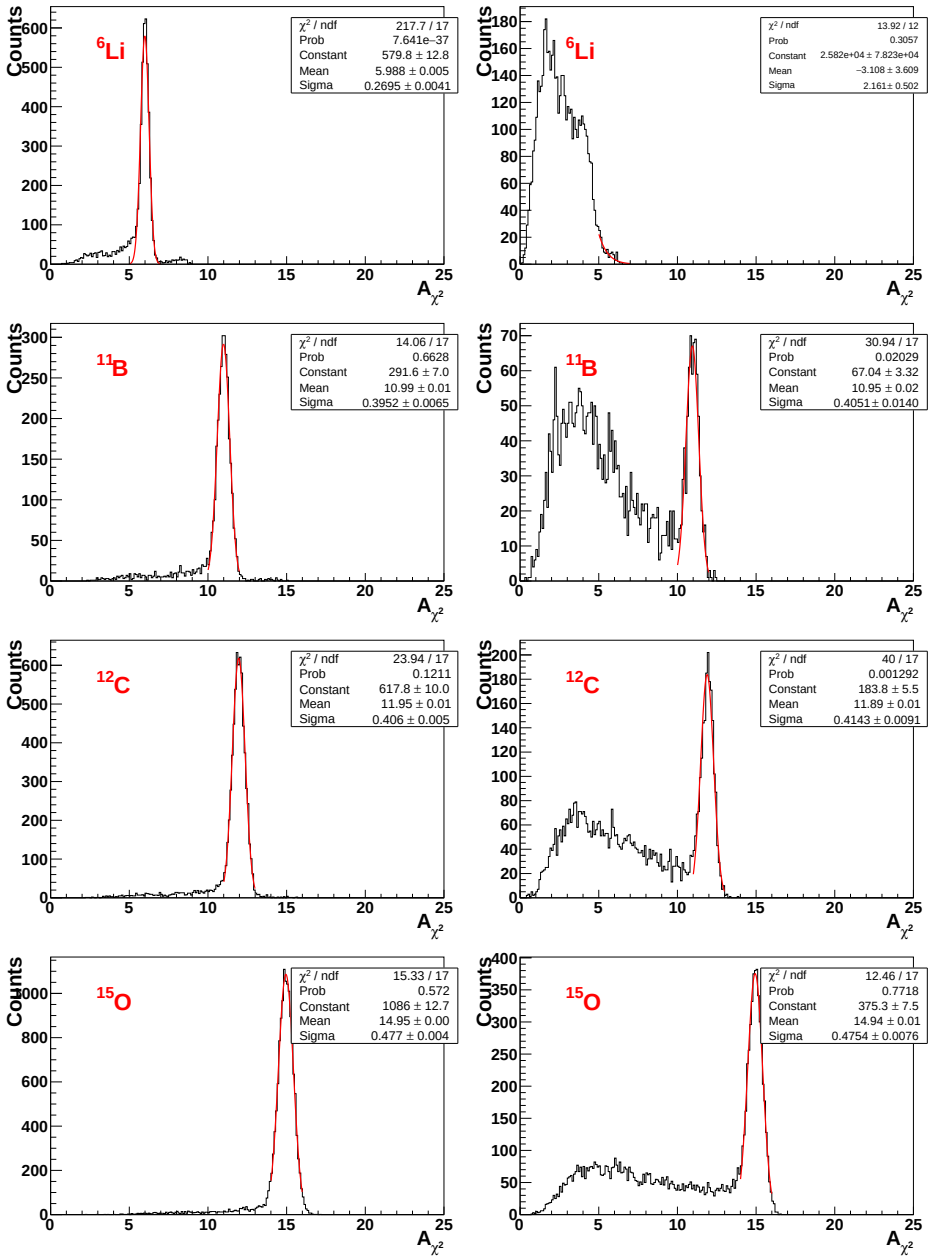

Fig. 4.16: A_{χ^2} distributions for the most abundant isotopes of fragments with $Z > 2$ produced by a ^{16}O beam at $200\,\mathrm{MeV/u}$ impinging on a polyethylene target.

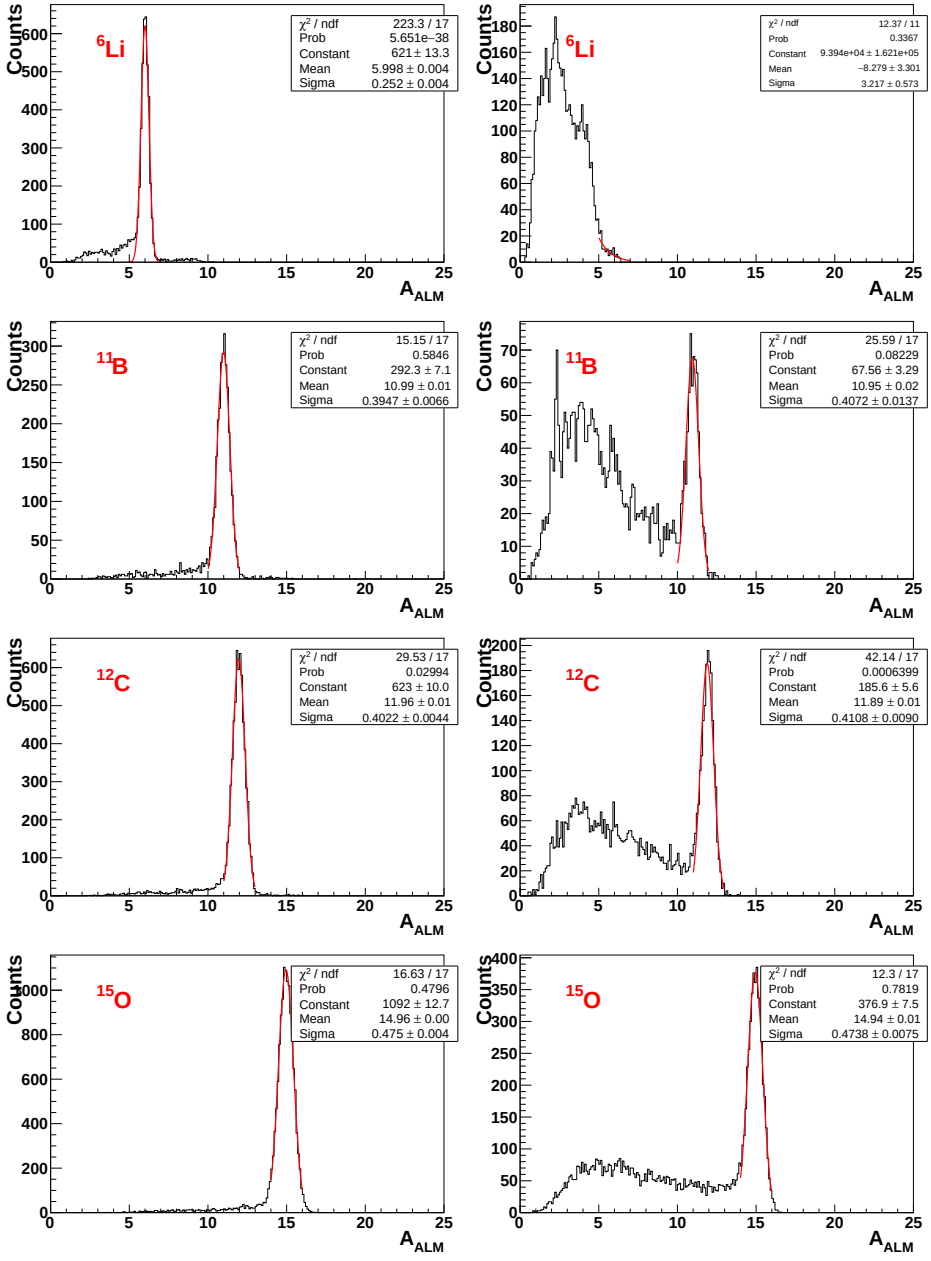

Fig. 4.17: A_{ALM} distributions for the most abundant isotopes of fragments with $Z > 2$ produced by a ^{16}O beam at $200\,\mathrm{MeV/u}$ impinging on a polyethylene target.

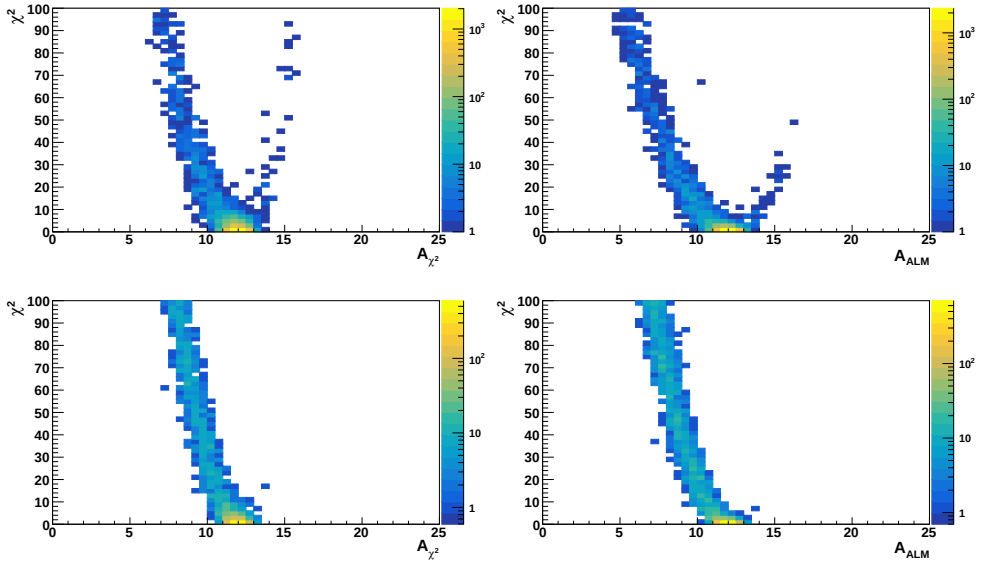

Fig. 4.18: χ^2 versus A_{χ^2} (left column) and versus A_{ALM} (right column) for ^{12}C fragments produced by $200\,\mathrm{MeV/u}$ (top row) and $700\,\mathrm{MeV/u}$ ^{16}O beam impinging on a polyethylene target. To discard the badly reconstructed fragments belonging to the tail, a χ^2 cut can be applied.

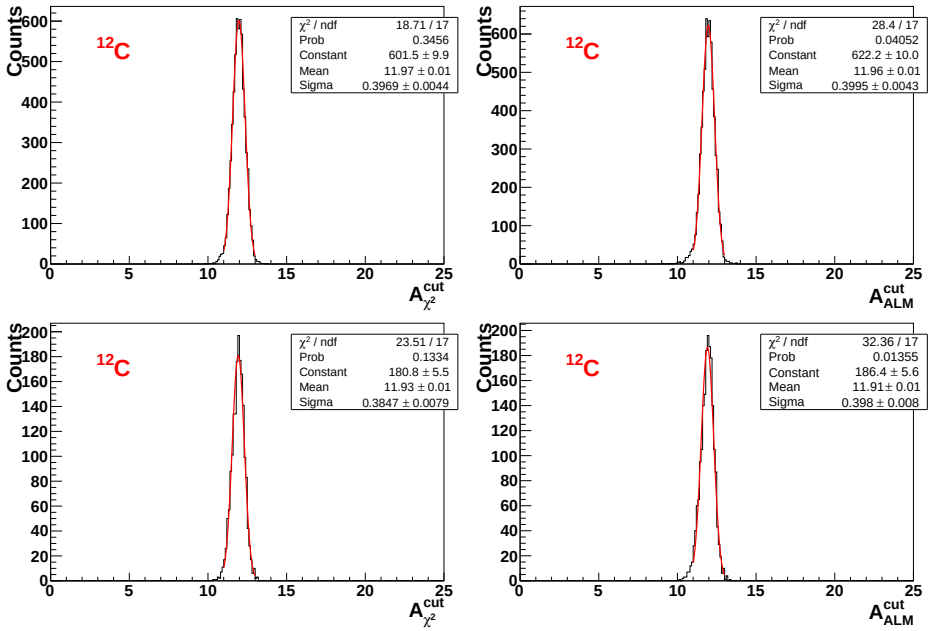

Fig. 4.19: $A^{cut}_{\chi^2}$ (left column) and A^{cut}_{ALM} (right column) for a ^{12}C fragments produced by $200\,\mathrm{MeV/u}$ (top row) and $700\,\mathrm{MeV/u}$ (bottom row) ^{16}O beam impinging on a polyethylene target.

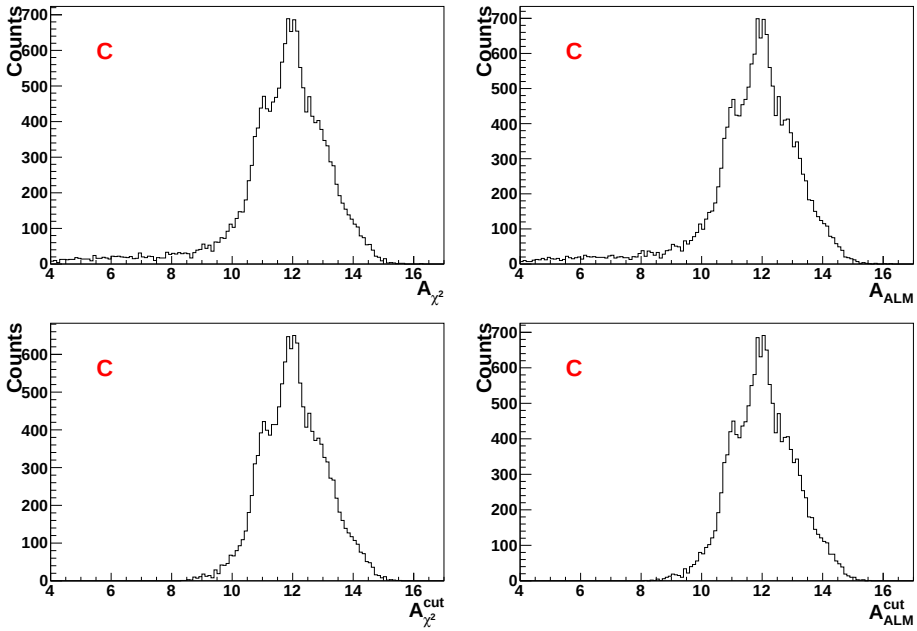

Fig. 4.20: In the top row, A_{χ^2} (left) and A_{ALM} (right) for all the carbon isotopes (^{9}C, ^{10}C, ^{11}C, ^{12}C, ^{13}C and ^{14}C) produced by 200 MeV/u ^{16}O beam impinging on a polyethylene target are depicted. In the bottom row, instead, $A^{cut}_{\chi^2}$ (left) and A^{cut}_{ALM} (right) are shown.

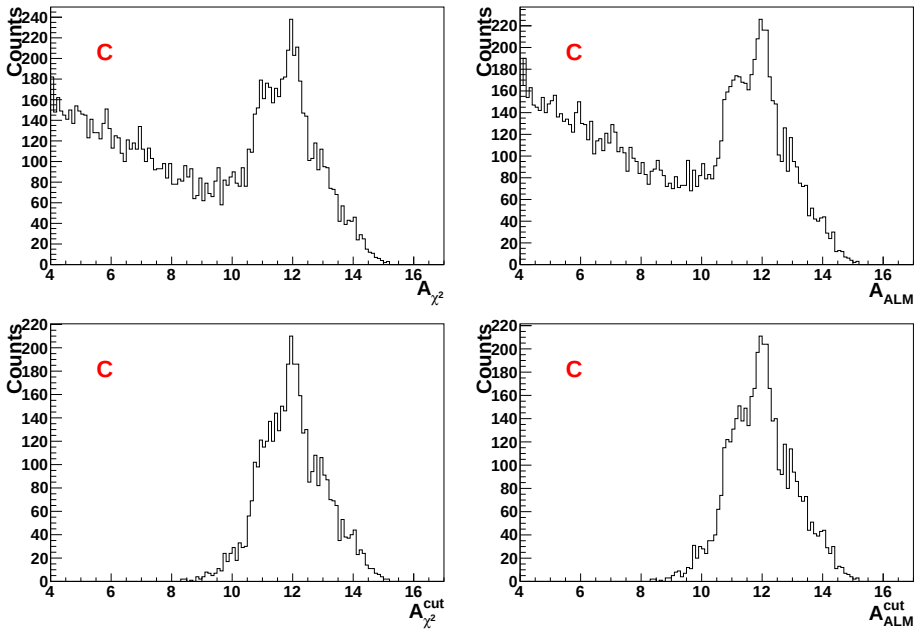

Fig. 4.21: In the top row, A_{χ^2} (left) and A_{ALM} (right) for all the carbon isotopes (^{9}C, ^{10}C, ^{11}C, ^{12}C, ^{13}C and ^{14}C) produced by 700 MeV/u ^{16}O beam impinging on a polyethylene target are depicted. In the bottom row, instead, $A^{cut}_{\chi^2}$ (left) and A^{cut}_{ALM} (right) are shown.

Frag.	A_{χ^2}	$\sigma(A_{\chi^2})$ [%]	A_{ALM}	$\sigma(A_{ALM})$ [%]	$A^{cut}_{\chi^2}$	$\sigma(A^{cut}_{\chi^2})$ [%]	A^{cut}_{ALM}	$\sigma(A^{cut}_{ALM})$ [%]
^{6}Li	5.99±0.26	4.4	6.00±0.24	4.1	6.01±0.24	4.7	6.01±0.23	3.9
^{7}Li	7.00±0.30	4.3	7.00±0.28	4.0	7.02±0.28	3.9	7.02±0.27	3.8
^{8}Li	8.05±0.34	4.2	8.04±0.35	4.3	8.04±0.32	4.0	8.05±0.33	4.2
^{7}Be	6.99±0.27	3.9	7.00±0.25	3.5	7.01±0.25	3.6	7.01±0.24	3.4
^{9}Be	9.00±0.33	3.7	9.00±0.32	3.6	9.01±0.32	3.5	9.00±0.32	3.6
^{10}Be	9.97±0.36	3.6	9.98±0.37	3.7	9.99±0.34	3.4	9.99±0.36	3.6
^{8}B	8.03±0.25	3.1	8.05±0.25	3.1	8.04±0.24	3.0	8.05±0.25	3.1
^{10}B	9.99±0.34	3.4	9.99±0.34	3.4	10.00±0.33	3.3	9.99±0.33	3.3
^{11}B	10.99±0.39	3.5	10.99±0.38	3.5	11.00±0.37	3.4	11.00±0.38	3.4
^{12}B	12.07±0.55	4.6	12.03±0.57	4.7	12.07±0.54	4.5	12.04±0.56	4.6
^{9}C	9.05±0.47	5.2	8.99±0.46	5.2	9.08±0.40	4.4	9.0±0.43	4.9
^{10}C	10.00±0.33	3.3	10.02±0.33	3.3	10.02±0.33	3.3	10.02±0.33	3.3
^{11}C	10.99±0.37	3.3	11.00±0.36	3.3	11.00±0.36	3.2	11.00±0.36	3.3
^{12}C	11.96±0.40	3.3	11.96±0.39	3.2	11.97±0.39	3.2	11.96±0.38	3.2
^{13}C	12.96±0.44	3.4	12.96±0.44	3.4	12.97±0.43	3.3	12.96±0.43	3.3
^{14}C	13.97±0.44	3.2	13.98±0.47	3.4	13.99±0.43	3.1	13.98±0.47	3.4
^{12}N	12.05±0.63	5.2	12.05±0.60	5.0	12.05±0.69	5.7	12.05±0.61	5.0
^{13}N	12.97±0.41	3.1	12.97±0.41	3.2	12.98±0.40	3.1	12.98±0.41	3.1
^{14}N	13.96±0.47	3.4	13.96±0.47	3.4	13.97±0.46	3.3	13.97±0.46	3.3
^{15}N	14.95±0.49	3.3	14.95±0.49	3.3	14.96±0.48	3.2	14.95±0.49	3.3
^{14}O	13.93±0.43	3.1	13.95±0.42	3.1	13.94±0.43	3.1	13.96±0.42	3.0
^{15}O	14.95±0.47	3.2	14.96±0.47	3.2	14.97±0.47	3.1	14.96±0.47	3.1

Table 4.3: A values and relative resolutions (in percentage) obtained from χ^2 fit and ALM (with and without $\chi^2 < 5$ cut).

Frag.	A_{χ^2}	$\sigma(A_{\chi^2})$ [%]	A_{ALM}	$\sigma(A_{ALM})$ [%]	$A^{cut}_{\chi^2}$	$\sigma(A^{cut}_{\chi^2})$ [%]	A^{cut}_{ALM}	$\sigma(A^{cut}_{ALM})$ [%]
^{7}Li	6.40±0.28	4.3	6.45±0.33	5.2	6.45±0.33	5.2	6.93±0.25	3.6
^{8}Li	8.03±0.30	3.7	8.03±0.30	3.7	8.03±0.30	3.7	8.03±0.30	3.7
^{7}Be	6.98±0.25	3.5	6.98±0.25	3.6	6.99±0.23	3.2	7.00±0.23	3.3
^{9}Be	8.67±0.50	5.7	8.71±0.50	5.7	8.85±0.39	4.4	8.89±0.34	3.8
^{8}B	7.95±0.29	3.7	8.04±0.32	4.0	8.01±0.24	3.0	8.04±0.29	3.6
^{10}B	9.98±0.35	3.5	9.98±0.35	3.5	10.01±0.31	3.1	10.00±0.32	3.2
^{11}B	10.95±0.41	3.7	10.95±0.41	3.7	11.00±0.38	3.4	10.98±0.39	3.6
^{12}B	11.98±0.59	5.0	11.93±0.58	4.9	11.99±0.61	5.1	11.92±0.59	4.9
^{9}C	9.09±0.27	3.0	9.15±0.16	1.8	9.07±0.33	3.6	9.15±0.16	1.8
^{10}C	9.99±0.31	3.1	9.99±0.32	3.2	9.99±0.31	3.1	10.00±0.32	3.2
^{11}C	10.96±0.37	3.4	10.96±0.36	3.3	10.99±0.35	3.1	10.98±0.35	3.2
^{12}C	11.89±0.41	3.5	11.89±0.41	3.5	11.93±0.38	3.2	11.91±0.40	3.3
^{13}C	12.90±0.45	3.5	12.90±0.45	3.5	12.95±0.41	3.1	12.92±0.43	3.4
^{14}C	13.92±0.49	3.5	13.91±0.50	3.6	13.96±0.47	3.3	13.94±0.47	3.4
^{12}N	12.07±0.48	4.0	12.08±0.43	3.6	12.09±0.44	3.7	12.08±0.43	3.6
^{13}N	12.94±0.46	3.5	12.96±0.44	3.4	12.98±0.43	3.3	12.97±0.43	3.3
^{14}N	13.94±0.45	3.2	13.94±0.45	3.2	13.97±0.42	3.0	13.95±0.44	3.1
^{15}N	14.92±0.49	3.3	14.93±0.49	3.3	14.96±0.46	3.1	14.94±0.48	3.2
^{14}O	14.03±0.41	3.0	14.01±0.37	2.6	14.03±0.40	2.8	14.02±0.37	2.6
^{15}O	14.94±0.48	3.2	14.94±0.47	3.2	14.97±0.46	3.1	14.96±0.46	3.1

Table 4.4: A values and relative resolutions (in percentage) obtained from χ^2 fit and ALM (with and without $\chi^2 < 5$ cut).

4.4 Cross sections measurements

In this section, the results of the MC data analysis previously presented are employed to illustrate the procedure required for the cross sections determination and a preliminary calculation in the case of projectile fragmentation.

The A and Z identification allows to reconstruct for each fragment the yield as a function of the emission angle, $Y(\theta)$, or of the production energy, $Y(E)$. Starting from these yields, it is possible to calculate the production differential cross sections as follows:

$$\frac{\mathrm{d}\sigma_f}{\mathrm{d}\theta} = \frac{Y_f(\theta)}{N_{prim}\, N_t\, \Omega_\theta\, \epsilon} \tag{4.32}$$

$$\frac{\mathrm{d}\sigma_f}{\mathrm{d}E} = \frac{Y_f(E)}{N_{prim}\, N_t\, \Omega_E\, \epsilon} \tag{4.33}$$

where f indicates the f^{th} fragment characterized by the reconstructed Z and A values, N_{prim} is the number of primary particles, N_t is the number of particles per unit surface in the target, Ω_θ and Ω_E are the angular and energy phase spaces respectively, and ϵ is the reconstruction efficiency. In the following, all the terms of Eqs. 4.32 and 4.33 are discussed:

- the number of particles per unit surface in the target, N_t, can be calculated according to the target dimensions and material:

$$N_t = \frac{\rho\, N_A\, z}{A} \tag{4.34}$$

  where N_A is the Avogadro's number and ρ, A and z are the target density, mass number and target thickness.

- the phase spaces are defined as

$$\Omega_\theta = 2\,\pi\, \left[cos(\theta^f_{min}) - cos(\theta^f_{max})\right] \tag{4.35}$$

$$\Omega_E = E^f_{max} - E^f_{min} \tag{4.36}$$

  where θ^f_{min}, θ^f_{max}, E^f_{min} and E^f_{max} are the angle and the energy lower and higher limits of the f^{th} bin of the corresponding yield distribution. In this work, constant angle bin width of $0.2°$ and energy bin width of $10\,\mathrm{MeV}$ have been adopted.

- in this analysis the number of primary particles, N_{prim}, is the number of primary particles generated in the simulation, while during the experiment will be provided by the STC.

- the yields are function of the production angle and energy. When the yield calculation is performed on real experimental data, the "true" production angle and energy distributions must be retrieved from the measured ones. Due detectors and tracking related effects, the measured energy or angle can differ from the true

one, thus falling in an incorrect bin of the measured spectrum. To access to the real production observables, the measured distributions must be corrected from the experimental effects (tracking and detectors effects) affecting them. This can be done by means of an *unfolding*, a complex procedure requiring the construction of a correction matrix, $\boldsymbol{A}$, which correlates the true and the measured angular and kinetic energy distributions. This is a linear problem described by the following equation:

$$\boldsymbol{Ax} = \boldsymbol{y} \tag{4.37}$$

where $\boldsymbol{x}$ are the true quantities and $\boldsymbol{y}$ the measured ones. This matrix can be built by means of a dedicated MC simulation. The measured observables are obtained considering all the experimental effects (detector and readout thresholds, detector resolutions, etc.) and, as well as the true observables, are retrieved by building a customized simulation output. The obtained matrix must then be inverted to be applied to the experimental measured quantities in order to obtain the true distribution:

$$\boldsymbol{x} = \boldsymbol{A}^{-1}\boldsymbol{y} \tag{4.38}$$

The matrix inversion is not a trivial task. For example, the inverse matrix may not even exist. This procedure requires the use of advanced and robust statistics methods (D'Agostini 1995). However, at present, the unfolding procedure can not be applied since a detailed description of the tracking and detectors efficiencies and thresholds is not yet available. In fact, FOOT is still in a design phase: some detectors must still be built and also the tracking algorithms are not yet fully developed, as previously described. Though, since in this study the analyzed data come from MC simulations, the true production distributions are easily accessible, and therefore in this analysis the reconstructed yields can be preliminary expressed as a function of the true production energy and angle. To evaluate the yields distributions the atomic number Z and the mass number A from the ALM fit have been used. Only fragments reaching the CAL which survived the χ^2 cut have been included (Fig. 4.22).

- ϵ is the overall efficiency of the measurement and reconstruction process used to correct the obtained cross sections. ϵ can be subdivided in different terms:

$$\epsilon = \epsilon_{track}\ \epsilon_{id}\ \epsilon_{det}\ \epsilon_{phys} \tag{4.39}$$

where

  - ϵ_{track} is the tracking efficiency, which is related to the reconstruction algorithm. As already explained, the tracking is still under development and the true MC tracks have been used to build the reconstructed tracks. Therefore ϵ_{track} has been set equal to 1.
  - ϵ_{det} is the detectors experimental efficiency. Since, as already discussed, they are not available yet, in the analyzed simulations no efficiency or threshold has been implemented, therefore all the detectors produce a "signal" when crossed by a fragment and $\epsilon_{det} = 1$.

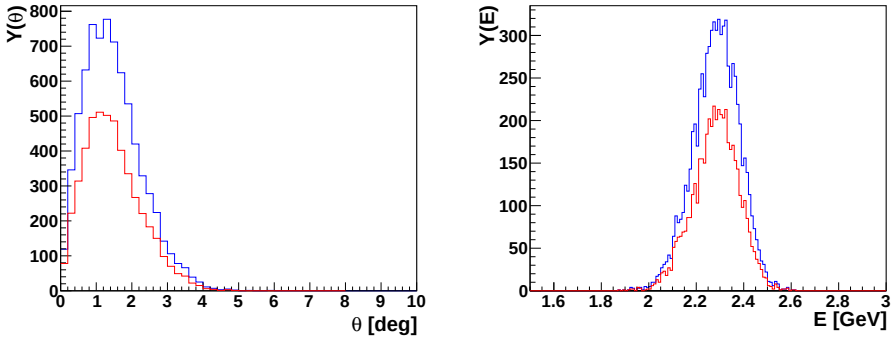

Fig. 4.22: True (blue) and reconstructed (red) yields for ^{12}C fragments produced by a 200 MeV/u ^{16}O beam impinging on a polyethylene target. Both the angular (left) and kinetic energy (right) yield distributions are shown.

– ϵ_{id} is the fragment identification efficiency, which represents the probability to correctly identify the fragment. A proper evaluation of this efficiency can be obtained from a full MC simulations including the experimental effects, by measuring the probabilities that a fragment of type a is correctly identified as a type a or mis-identified as a type b or c, etc. These probabilities form the mixing matrix $\boldsymbol{\epsilon_{mix}}$:

$$\boldsymbol{\epsilon_{mix}} = \begin{pmatrix} \epsilon^{aa} & \epsilon^{ab} & \epsilon^{ac} & \dots \\ \epsilon^{ba} & \epsilon^{bb} & \epsilon^{bc} & \\ \epsilon^{ca} & \epsilon^{cb} & \epsilon^{cc} & \\ \vdots & & & \ddots \end{pmatrix} \tag{4.40}$$

The diagonal elements of $\boldsymbol{\epsilon_{mix}}$ represent the probability of a correct fragment identification, while the other elements outside the diagonal correspond to the mis-identification (*cross feed*) probability and will be used to correct the cross section evaluation.

– ϵ_{phys} is a term related to physical aspects of the problem and takes into account the probability that a fragment is not reconstructed. The reasons are various and include fragments emitted at large angle out of the detector geometrical acceptance, fragments emitted within the apparatus angular acceptance but then deviated by the magnetic field, fragments that do not cross all the detectors because they have too low energy and fragments undergoing re-fragmentation before reaching the CAL.

A preliminary estimation $\epsilon = \epsilon_{id}\ \epsilon_{phys}$ has been estimated by evaluating the percentage of tracks with a given Z and A values that, for physical reasons, are not reconstructed. The efficiency has been therefore evaluated for each energy and angular interval (or bin of the corresponding yield distribution) as the ratio between the number k_i of correctly reconstructed (in terms of Z and A) fragments within

the i^{th} bin and the number n_i of fragments truly generated in the same bin. The efficiency is evaluated according to the binomial distribution, and its variance is:

$$\sigma^2(\epsilon_i) = \frac{\epsilon_i(1-\epsilon_i)}{n_i} \tag{4.41}$$

However, this formula fails when $k_i = 0$ or $k_i = n_i$. Considering the binomial probability density function, which is

$$P(\epsilon_i; k_i, n_i) = \frac{(n_i+1)!}{k_i!(n_i-k_i)!}\epsilon^{k_i}(1-\epsilon)^{n_i-k_i} \tag{4.42}$$

the variance can be expressed as

$$\begin{aligned}\sigma^2(\epsilon_i) &= \overline{\epsilon_i^2} - \overline{\epsilon_i}^2 = \\ &= \int_0^1 \epsilon_i^2 P(\epsilon_i; k_i, n_i)\,\mathrm{d}\epsilon_i - \overline{\epsilon_i}^2 = \\ &= \frac{(k_i+1)(k_i+2)}{(n_i+2)(n_i+3)} - \frac{(k_i+1)^2}{(n_i+2)^2}\end{aligned} \tag{4.43}$$

This formula solve the problem in the limit cases $k_i = 0$ or $k_i = n_i$.

Following these considerations, the angular and energy differential cross sections for different fragments produced by a $200\,\mathrm{MeV/u}$ $^{16}\mathrm{O}$ beam impinging on a polyethylene and a carbon target have been calculated. As an example, in Fig. 4.23 the true and measured $^{12}\mathrm{C}$ production cross sections are compared. Only statistical errors are reported. In Fig. 4.24, the measured production cross sections of $^{12}\mathrm{C}$ fragments in the cases of a polyethylene target and a carbon target are shown, as well as the cross sections on hydrogen retrieved according to Eqs. 2.2 and 2.3. Some of the calculated values are reported in Tabs. 4.5 and 4.6.

The same procedure can be adopted to calculate the inverse kinematics cross sections by using the fragments boosted energy.

The cross sections here reported have been obtained from a MC simulation of 1×10^7 primaries, which is approximately the minimum sample size that will be required in the real data acquisition for each projectile/target combination. The experimental cross section measurements, however, will be more likely dominated by systematic rather than statistical error. Systematic errors will include, among others, fragments kinetic energy underestimation (see Sec. 4.2), uncertainties on identification efficiency and cross feed probability, possible mis-alignment of the tracking detectors leading to incorrect momentum estimation. Dedicated studies will be carried out in the future to evaluate the contribution of each systematic error source.

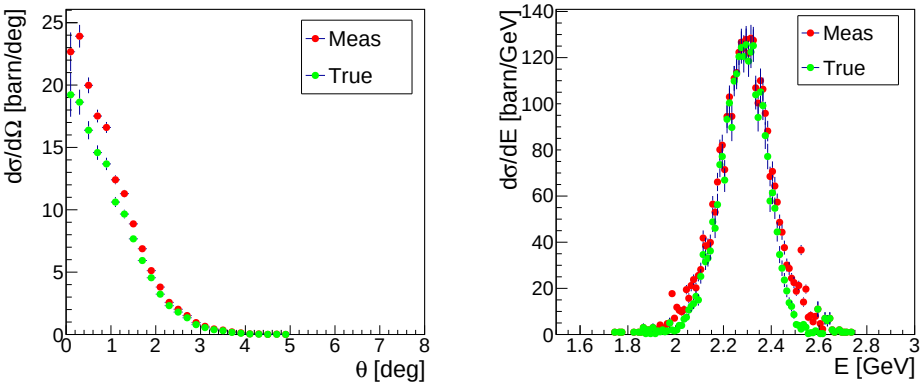

Fig. 4.23: Comparison between the true and reconstructed differential cross sections for ^{12}C fragments produced by a 200 MeV/u ^{16}O beam impinging on a polyethylene target. Both the angular (left) and energy (right) differential cross sections are displayed.

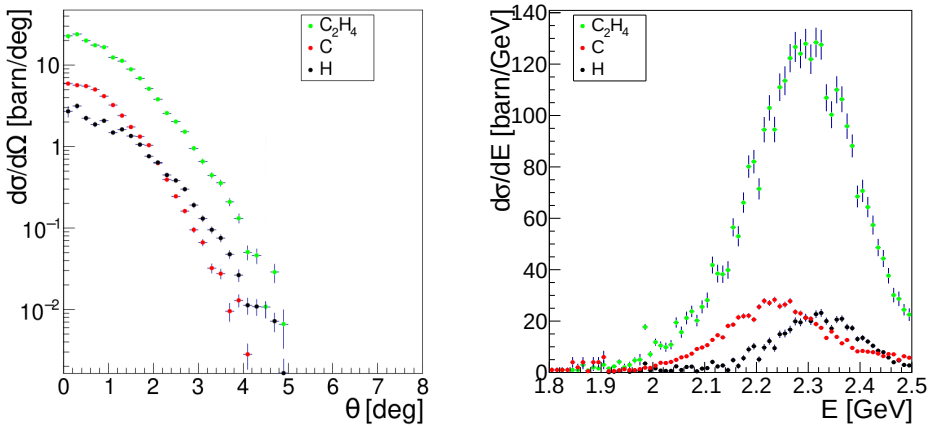

Fig. 4.24: Comparison between the measured differential cross sections for ^{12}C fragments produced by a 200 MeV/u ^{16}O beam impinging on polyethylene, carbon and hydrogen target as retrieved from Eqs. 2.2 and 2.2. Both the angular (left) and energy (right) differential cross sections are displayed.

	$d\sigma/d\theta$ [barn/deg]		
Angle [deg]	C_2H_4	C	H
0.1	5.92±0.33	22.68±1.55	2.71±0.42
0.3	5.66±0.19	23.91±0.91	3.15±0.25
0.5	5.52±0.15	19.98±0.63	2.23±0.17
0.7	5.02±0.12	17.52±0.51	1.87±0.14
0.9	4.16±0.09	16.60±0.44	2.07±0.12
1.1	3.23±0.08	12.41±0.36	1.49±0.10
1.3	2.40±0.06	11.29±0.30	1.62±0.08
1.5	1.74±0.05	8.87±0.26	1.35±0.07
1.7	1.32±0.04	6.88±0.21	1.06±0.05
1.9	1.04±0.03	5.12±0.17	0.76±0.04
2.1	0.63±0.02	3.80±0.14	0.64±0.04
2.3	0.39±0.02	2.57±0.11	0.45±0.03
2.5	0.25±0.01	2.02±0.09	0.38±0.02
2.7	0.16±0.01	1.52±0.08	0.30±0.02
2.9	0.10±0.01	0.95±0.06	0.19±0.02

Table 4.5: Differential cross sections as a function of the production angle θ for ^{12}C fragments produced by a $200\,MeV/u$ ^{16}O beam.

	$d\sigma/dE$ [barn/GeV]		
Energy [GeV]	C_2H_4	C	H
2.20	25.53±1.08	71.46±4.13	5.10±1.17
2.21	27.88±1.12	94.49±4.93	9.69±1.35
2.22	27.04±1.15	102.96±4.96	12.22±1.37
2.23	28.32±1.14	94.53±4.95	9.47±1.36
2.24	25.76±1.13	111.01±5.37	14.88±1.46
2.25	26.43±1.13	113.53±5.61	15.17±1.51
2.26	27.78±1.12	122.32±5.51	16.69±1.49
2.27	23.55±1.04	126.68±5.85	19.89±1.55
2.28	23.02±1.04	124.04±5.66	19.50±1.51
2.29	21.29±1.00	127.92±5.80	21.33±1.53
2.30	20.92±1.03	121.91±5.74	20.02±1.53
2.31	18.84±0.91	128.45±5.74	22.69±1.51
2.32	17.38±0.84	127.52±5.80	23.19±1.51
2.33	13.46±0.78	106.90±5.27	19.99±1.37
2.34	15.92±0.81	100.31±5.24	17.12±1.37
2.35	13.85±0.84	110.01±5.27	20.58±1.38
2.36	11.36±0.75	106.32±5.04	20.90±1.32

Table 4.6: Differential cross sections as a function of the production kinetic energy E for ^{12}C fragments produced by a $200\,MeV/u$ ^{16}O beam.

Conclusions

This thesis summarizes the work for the development of the full Monte Carlo simulation which is being used for the design and optimization of the FOOT experiment. FOOT is an experiment of applied nuclear physics, aiming to measure nuclear fragmentation cross sections which are relevant in particle therapy and space radioprotection. These measurements are fundamental to improve the nuclear interactions description and benchmark the nuclear models used to calculate the dose maps in treatment planning and in radiation shielding studies. To this purpose, two experimental setup have been developed, and this thesis focuses on the electronics apparatus, which aims to measure $Z \geq 3$ fragments, which are emitted at small angles with respect to the primary beam. By measuring momentum, time of flight, kinetic energy and energy loss in thin detectors, the FOOT apparatus will determine fragments charge and mass, as well as their energy and production angle.

The development phase of the FOOT electronic setup started three years ago, almost concomitantly with the beginning of this PhD work, and is still ongoing. During these years, the study and the optimization of the apparatus components have been guided by the simulations based on the use of the FLUKA Monte Carlo code, described in Chap.3. The choice of FLUKA, which is continuosly benchmarked and developed expecially in view of particle therapy application, guarantees the necessary level of reliability.

On the basis of this choice, this thesis describes in some detail the strategies employed to produce reliable and accurate simulations of the experiment. A dedicated software has been developed to automatize the simulation input and geometry construction, and an output characterized by an advanced customization level has been produced to satisfy the required accuracy and precision. This software has been also integrated in the FOOT reconstruction software, to ensure the implementation of identical geometry, materials and magnetic field in both simulations and reconstruction algorithms. Thanks to the work described here, a robust basis to the performances analysis and optimization for the entire collaboration has been provided. This has allowed to test different configuration of detectors and layout.

The simulated data produced by means of the codes described in this thesis are now used to investigate the capability of FOOT to identify and reconstruct the different nu-

clear fragments. This is reported in Chap.4. A preliminary analysis code has been developed to this purpose. This code will be integrated within the FOOT reconstruction software in order to perform the full reconstruction of the events obtained from both experimental and FLUKA simulated data. In this thesis, the reconstruction and the analysis of the produced FLUKA samples are described. The expected resolutions of the different detectors have been applied to Monte Carlo samples in order to recreate experimental-like data. The charge identification analysis demonstrates that the atomic number determination can be achieved with 2-3% resolution. The identification of the mass, instead, proves to be a more challenging task. However, the strength of the FOOT electronic setup lies on its redundancy. The measurement of fragments time of flight, momentum and kinetic energy allows in fact to retrieve the mass in three different ways, by coupling each time two of these measured quantities. Minimization fitting techniques, here described, provide a solid method for the best determination of the mass number, allowing to discriminate events whose measurement has been possibly spoiled for example by a kinetic energy underestimation, which is particularly relevant at high beam energies. The achieved mass number resolution is approximately of the order of 3-4%, which meets the resolutions required by radiobiologists. Here the procedure to determine the reconstructed angular and energy yields is also tested, describing the procedure to calculate the required differential cross sections. To this purpose a preliminary estimation of the reconstruction efficiency has been provided. In this preliminary study only statistical errors could be considered, since the evaluation of systematics will be possibile only after collecting additional information deriving from the experimental test of the different detectors and of the reconstruction software. At present the simulation setup here described is being used to achieve the final optimization of the FOOT design, in view of the construction which is planned for 2019.

Appendices

APPENDIX A

FLUKA input

In the following, an example of the FOOT input is reported. In this input file, a $200\,\mathrm{MeV/u}$ ^{16}O beam and a $2\,\mathrm{mm}$ thick C_2H_4 target are simulated

```
TITLE
FOOT setup
* ******************************************************************************
GLOBAL         9999.                                          1.
DEFAULTS                                                                 PRECISIO
PHYSICS           3.                                                     EVAPORAT
IONTRANS    HEAVYION
RADDECAY          2.                  1.
* ******************************************************************************
*                           GENERAL & PRIMARY                                    *
* ******************************************************************************
* -------1---------2---------3---------4---------5---------6---------7---------8
* command| what(1) | what(2) | what(3) | what(4) | what(5) | what(6) | SDUM    |
* -------1---------2---------3---------4---------5---------6---------7---------8
* @@@START GENERATED, DO NOT MODIFY:GENERAL@@@ ********************************
PHYSICS           1.                                                     COALESCE
BEAM       -0.200000       0.0       0.0 -0.480000 -0.480000        1.HEAVYION
HI-PROPE          8.       16.
BEAMPOS         0.0       0.0      -30.       0.0       0.0
*EMFCUT           -1.        1.               BLACK  @LASTREG         1.
*EMFCUT           -1.        1.        1.  BLCKHOLE  @LASTMAT         1.PROD-CUT
*DELTARAY          1.                      BLCKHOLE  @LASTMAT         1.
*PAIRBREM         -3.                      BLCKHOLE  @LASTMAT
* @@@END GENERATED:GENERAL@@@ **************************************************
* ******************************************************************************
*                           GEOMETRY                                             *
* ******************************************************************************
GEOBEGIN                             15.                                 COMBNAME
foot.geo
GEOEND
* ******************************************************************************
*                           MEDIA                                                *
* ******************************************************************************
* -------1---------2---------3---------4---------5---------6---------7---------8
* command| what(1) | what(2) | what(3) | what(4) | what(5) | what(6) | SDUM    |
* -------1---------2---------3---------4---------5---------6---------7---------8
* *** Aggiunte manuali
MATERIAL         0.0       0.0       0.0                                 BLCKHOLE
```

```
MATERIAL         0.0       0.0       0.0                              VACUUM
MATERIAL          1.   1.00794 8.3748E-5                              HYDROGEN
MATERIAL          2.  4.002602 1.6632E-4                              HELIUM
MATERIAL          4.  9.012182     1.848                              BERYLLIU
MATERIAL          6.   12.0107        2.                              CARBON
MATERIAL          7.   14.0067 0.0011653                              NITROGEN
MATERIAL          8.   15.9994 0.0013315                              OXYGEN
MATERIAL         12.   24.3050      1.74                              MAGNESIU
MATERIAL         13. 26.981538    2.6989                              ALUMINUM
MATERIAL         26.    55.845     7.874                              IRON
MATERIAL         29.    63.546      8.96                              COPPER
MATERIAL         47.  107.8682      10.5                              SILVER
MATERIAL         14.   28.0855      2.33                              SILICON
MATERIAL         79. 196.96655     19.32                              GOLD
MATERIAL         80.    200.59    13.546                              MERCURY
MATERIAL         82.     207.2     11.35                              LEAD
MATERIAL         73.  180.9479    16.654                              TANTALUM
MATERIAL         11. 22.989770     0.971                              SODIUM
MATERIAL         18.    39.948  0.001662                              ARGON
MATERIAL         20.    40.078      1.55                              CALCIUM
MATERIAL         50.   118.710      7.31                              TIN
MATERIAL         74.    183.84      19.3                              TUNGSTEN
MATERIAL         22.    47.867      4.54                              TITANIUM
MATERIAL         28.   58.6934     8.902                              NICKEL
* *** Samario-Cobalto permanent magnet
MATERIAL         62.                7.46                              SAMARIUM
MATERIAL         27.                 8.9                              COBALT
MATERIAL                             8.3                              SmCo
COMPOUND          2.  SAMARIUM       17.    COBALT                    SmCo
* *** Altro magnete permanente
MATERIAL         60.                6.9                               NEODYMIU
MATERIAL          5.               2.37                               BORON
MATERIAL         66.               8.55                               DYSPROSI
MATERIAL         41.               8.57                               NIOBIUM
MATERIAL                           7.6                                NdFeB
COMPOUND        -30.  NEODYMIU      -66.      IRON       -1.     BORONNdFeB
COMPOUND        -0.5  ALUMINUM       -1.  DYSPROSI       -1.   NIOBIUMNdFeB
*  Bismuto
MATERIAL         83.               9.747                               BISMUTH
* Germanio
MATERIAL         32.               5.323                               GERMANIU
* BGO
MATERIAL                           7.13                                BGO
COMPOUND          4.   BISMUTH        3.  GERMANIU       12.    OXYGENBGO
* Scintillator - EJ-232
*
MATERIAL                           1.023                               EJ-232
COMPOUND         10.  HYDROGEN        9.    CARBON                    EJ-232
*EMFRAY            4.   BLKBODY  @LASTREG
* Barium sulfate Ba_S_O4
MATERIAL         16.                2.07                               SULFUR
MATERIAL         56.                 3.5                               BARIUM
MATERIAL                             4.5                               BaSO4
COMPOUND   -0.274212    OXYGEN -0.137368    SULFUR  -0.58842    BARIUMBaSO4
* 221 Polyethylene, Marlex
```

```
* Density variation of polyethylene is 0.91 - 1.05 g/cm3. "Low" density is
*  0.920, "medium" is .93, and "high" is .95. Special polyethelene is made
* for nuclear shielding, and this has loaded densities up to 1.08.
* Chemical                    H    H
* Formula :                   |    |
*           |C H |       ---- C -- C ----
*           | 2 4|n           |    |
*                             H    H
MATERIAL                            0.94                                Polyethy
COMPOUND          4.  HYDROGEN        2.    CARBON                      Polyethy
* Grafite
MATERIAL          6.                2.26                                Graphite
LOW-MAT     Graphite        6.       -3.      296.                      CARBON
* 222 Mylar, Melinex
* Chemical Formula :  H-C = C-H            H   H
*                     /       \            |   |
*       ---- O - C - C         C - C - O - C - C -------
*                ||   \\     //    ||      |   |
*  C  H 0        O    H-C - C-H    O       H   H
*   10 8 4
MATERIAL                             1.4                                Mylar
COMPOUND          8.  HYDROGEN       10.    CARBON        4.    OXYGENMylar
* 104 Air dry (near sea level)
*
MATERIAL                        .00120484                                AIR
COMPOUND   -1.248E-4    CARBON -0.755267  NITROGEN -0.231781    OXYGENAIR
COMPOUND   -0.012827     ARGON                                       AIR
* Bakelite
MATERIAL                            1.45                                BAKELITE
COMPOUND          9.  HYDROGEN        9.    CARBON        1.    OXYGENBAKELITE
* 134 Carbon Dioxide
* Formula           O == C == O
MATERIAL                          0.001842                              CO2
COMPOUND          1.    CARBON        2.    OXYGEN                      CO2
MAT-PROP         0.2                           CO2
MATERIAL                        .001677136                              Ar-CO2
COMPOUND        -0.8    -ARGON      -0.2      -CO2                      Ar-CO2
MAT-PROP          1.                        Ar-CO2
MATERIAL         18.            0.001662                                ARGON
* Kapton polyimide film (C22_H10_N2_O5)n
*
MATERIAL                            1.42                                KAPTON
COMPOUND   -0.026362  HYDROGEN -0.691133    CARBON  -0.07327  NITROGENKAPTON
COMPOUND   -0.209235    OXYGEN                                          KAPTON
MAT-PROP         0.8                188.     ARGON
MATERIAL          9.           0.0015803                                FLUORINE
* TEDLAR
MATERIAL                             1.5                                TEDLAR
COMPOUND          3.  HYDROGEN        2.    CARBON        1.  FLUORINETEDLAR
* Epoxy (cast)
* Chemical          H-C - C-H     CH3  H-C - C-H        H   H   H
* Formula             //    \\     |     //    \\        |   |   |
*          ----- O - C        C -- C -- C        C - O - C - C - C ---
*  C  H  0            \     /      |     \     /         |   |   |
*   18 19 3          H-C = C-H     CH3  H-C = C-H        H   O   H
```

```
* If epoxy has silica filler, density will be in range of 1.6 - 2.0 g/cm3.
MATERIAL                             1.18                                 Epoxy
COMPOUND         19.  HYDROGEN       18.    CARBON        3.    OXYGENEpoxy
* *** Silicon carbide
MATERIAL                             3.22                                 SiC
COMPOUND         -1.   SILICON       -1.    CARBON                      SiC
MATERIAL                           0.1288                                 SiCFoam
COMPOUND         -4.       SiC      -96.       AIR                      SiCFoam
*
* ***************************************************************************
*                        MEDIA & MAGFIELD                                     *
* ***************************************************************************
* -------1---------2---------3---------4---------5---------6---------7---------8
* command| what(1) | what(2) | what(3) | what(4) | what(5) | what(6) | SDUM    |
* -------1---------2---------3---------4---------5---------6---------7---------8
* @@@START GENERATED, DO NOT MODIFY:MATERIAL&MAGFIELD@@@ ***********************
ASSIGNMA    BLCKHOLE     BLACK
ASSIGNMA         AIR       AIR
ASSIGNMA      EJ-232       STC
ASSIGNMA    ALUMINUM   BMN_SHI
ASSIGNMA       Mylar  BMN_MYL0
ASSIGNMA       Mylar  BMN_MYL1
ASSIGNMA      Ar-CO2  BMN_C000  BMN_C017        1.
ASSIGNMA      Ar-CO2  BMN_C100  BMN_C117        1.
ASSIGNMA      Ar-CO2   BMN_GAS
ASSIGNMA    ALUMINUM   BMN_FWI
ASSIGNMA    TUNGSTEN   BMN_SWI
ASSIGNMA    Polyethy    TARGET                            1.
ASSIGNMA     SILICON     VTXP0     VTXS3        1.        1.
ASSIGNMA    ALUMINUM     ITRP2    ITRP73        1.        1.
ASSIGNMA       Epoxy     ITRP0    ITRP75        1.        1.
ASSIGNMA      KAPTON     ITRP1    ITRP74        1.        1.
ASSIGNMA     SILICON    ITRP13   ITRS313        1.        1.
ASSIGNMA     SiCFoam     ITRP6    ITRP69        1.        1.
ASSIGNMA        SmCo   MAG_PM0
ASSIGNMA    ALUMINUM   MAG_CV0
ASSIGNMA        SmCo   MAG_PM1
ASSIGNMA    ALUMINUM   MAG_CV1
ASSIGNMA         AIR   MAG_AIR                           1.
ASSIGNMA     SILICON     MSDS0     MSDS2        1.        1.
ASSIGNMA         AIR       BOX
ASSIGNMA      EJ-232    SCN000    SCN121        1.
ASSIGNMA         BGO    CAL000    CAL359        1.
MGNFIELD    0.100000  0.000010                 0.0       0.0       0.0
* @@@END GENERATED:MATERIAL&MAGFIELD@@@ *************************************
*
* ***************************************************************************
* -------1---------2---------3---------4---------5---------6---------7---------8
* command| idbflg  | FragTrg |Eth(Mev) |unused   |unused   |unused | SDUM      |
* -------1---------2---------3---------4---------5---------6---------7---------8
USRICALL         0.0        6.       0.1       0.0       0.0       0.0
USERDUMP        100.       69.       0.0        1.                   Opt
USROCALL
RANDOMIZ          1.   593585.
* ***************************************************************************
```

```
*                          RUN                                                  *
* ***************************************************************************
START         10000.
STOP
```

APPENDIX B

Example of parGeo class

In the following, an extract of the SCN `parGeo` class is reported.

```
for(unsigned int k=0; k<m_nLayer; k++){
 for(unsigned int j=0; j<m_nBar; j++){

  //ROOT addNode
 if(GlobalPar::GetPar()->geoROOT()){
  if(!gGeoManager->GetVolume(m_barMatrix[k][j]->GetMaterialRegionName().c_str()))
   cout<<"ERROR >> FootBox::AddNodeToUniverse --> volume not defined: "
       <<m_barMatrix[k][j]->GetMaterialRegionName()<<endl;

   TVector3 globalCoord = m_barMatrix[k][j]->GetPosition();
   Local2Global(&globalCoord);
   TVector3 barRotation = m_barMatrix[k][j]->GetEuler();
   barRotation = barRotation*180.*pow(TMath::Pi(),-1);
   m_universe->AddNode(gGeoManager->GetVolume(
                   m_barMatrix[k][j]->GetMaterialRegionName().c_str()),
                  m_barMatrix[k][j]->GetNodeID(),
                  new TGeoCombiTrans(globalCoord.x(),
                                globalCoord.y(),
                                globalCoord.z(),
                                new TGeoRotation("null,",
                                            barRotation.X(),
                                            barRotation.Y(),
                                            barRotation.Z()
                                            )));

   if(GlobalPar::GetPar()->Debug()>0)
     cout<<"\t"<<m_barMatrix[k][j]->GetMaterialRegionName()
         <<" ", globalCoord.Print();
 }


 // bodies
 if(GlobalPar::GetPar()->geoFLUKA()){
     TVector3 minCoord = TVector3(m_barMatrix[k][j]->GetMinCoord().x(),
                           m_barMatrix[k][j]->GetMinCoord().y(),
                           m_barMatrix[k][j]->GetMinCoord().z());
  TVector3 maxCoord = TVector3(m_barMatrix[k][j]->GetMaxCoord().x(),
                         m_barMatrix[k][j]->GetMaxCoord().y(),
                         m_barMatrix[k][j]->GetMaxCoord().z());
  Local2Global(&minCoord);
```

```
    Local2Global(&maxCoord);

    stringstream ss;
    ss<<setiosflags(ios::fixed)<<setprecision(6);
    ss<<"RPP "<<m_barMatrix[k][j]->GetBodyName()<<" "
      <<minCoord.x()<<" "<<maxCoord.x()<<" "
      <<minCoord.y()<<" "<<maxCoord.y()<<" "
      <<minCoord.z()<<" "<<maxCoord.z()<<endl;

    m_bodyPrintOut[m_barMatrix[k][j]->GetMaterialName()].push_back(ss.str());
    m_bodyName[m_barMatrix[k][j]->GetMaterialName()].push_back(
                                    m_barMatrix[k][j]->GetBodyName());

    // regions
    stringstream ssr;
    ssr<<setw(13)<<setfill(' ')<<std::left<<m_barMatrix[k][j]->GetRegionName()
       <<"5 "<<m_barMatrix[k][j]->GetBodyName()<<endl;

    m_regionPrintOut[m_barMatrix[k][j]->GetMaterialName()].push_back(ssr.str());
    m_regionName[m_barMatrix[k][j]->GetMaterialName()].push_back(
                                m_barMatrix[k][j]->GetRegionName());
    if(genfit::FieldManager::getInstance()->getFieldVal(
                                TVector3(minCoord)).Mag()==0
        && genfit::FieldManager::getInstance()->getFieldVal(
                                TVector3(maxCoord)).Mag()==0)
      m_magneticRegion[ m_barMatrix[k][j]->GetRegionName() ] = 0;
    else
      m_magneticRegion[ m_barMatrix[k][j]->GetRegionName() ] = 1;

    }
  }
}
```

Bibliography

Abou-Haidar Z. et al. 2012. Performance of upstream interaction region detectors for the FIRST experiment at GSI. *J. Instrum.*, **7**(02), P02006.

Agodi C. et al. 2012. Charged particle's flux measurement from PMMA irradiated by 80 MeV/u carbon ion beam. *Phys. Med. Biol.*, **57**(18), 5667.

Aleksandrov A. et al. 2015. Measurement of large angle fragments induced by 400 MeV n^{-1} carbon ion beams. *Meas. Sci. Technol.*, **26**(9), 094001.

Andersen V. et al. 2004. The FLUKA code for space applications: recent developments. *Adv. Space Res.*, **34**(6), 1302–1310.

Bak J. et al. 1987. Large departures from Landau distributions for high-energy particles traversing thin Si and Ge targets. *Nucl. Phys. B*, **288**, 681–716.

Barendsen G. W. 1994. The relationships between RBE and LET for different types of lethal damage in mammalian cells: biophysical and molecular mechanisms. *Radiat. Res.*, **139**(3), 257–270.

Battistoni G. et al. 2016a. Nuclear physics and particle therapy. *Adv. Phys.: X*, **1**(4), 661–686.

Battistoni G. et al. 2016b. The FLUKA code: an accurate simulation tool for Particle Therapy. *Fron. Oncol.*, **6**, 116.

Battistoni G. et al. 2015. Overview of the FLUKA code. *Ann. Nucl. Energy*, **82**, 10–18.

Belli M. et al. 1998. RBE-LET relationships for cell inactivation and mutation induced by low energy protons in V79 cells: further results at the LNL facility. *Int. J. Radiat. Biol.*, **74**(4), 501.

Bertini H. W. 1963. Low-energy intranuclear cascade calculation. *Phys. Rev.*, **131**(4), 1801.

Blann M. 1983. Precompound analyses of spectra and yields following nuclear capture of stopped π^-. *Phys. Rev. C*, **28**(4), 1648.

Böhlen T. T. et al. 2014. The FLUKA code: developments and challenges for high energy and medical applications. *Nucl. Data Sheets*, **120**, 211–214.

Böhlen T. et al. 2010. Benchmarking nuclear models of FLUKA and GEANT4 for carbon ion therapy. *Phys. Med. Biol.*, **55**(19), 5833.

Boudard A. et al. 2013. New potentialities of the Liege intranuclear cascade model for reactions induced by nucleons and light charged particles. *Phys. Rev. C*, **87**(1), 014606.

Bradt H. L. & Peters B. 1950. The Heavy Nuclei of the Primary Cosmic Radiation. *Phys. Rev.*, **77**(Jan), 54–70.

Braunn B. et al. 2015. Assessment of nuclear-reaction codes for proton-induced reactions on light nuclei below 250 MeV. *Eur. Phys. J. Plus*, **130**(7), 153.

Capella A. et al. 1994. Dual parton model. *Physics Reports*, **236**(4-5), 225–329.

Cerutti F. et al. 2006. Low energy nucleus–nucleus reactions: the BME approach and its interface with FLUKA. *Pages 507–514 of: Proc. 11th Int. Conf. Nuclear Reaction Mechanisms*, vol. 126.

Cerutti F. et al. 2017. Nuclear model developments in FLUKA for present and future applications. *Page 12005 of: EPJ Web of Conferences*, vol. 146. EDP Sciences.

Choi J. & Kang J. O. 2012. Basics of particle therapy II: relative biological effectiveness. *Radiat. Oncol. J.*, **30**(1), 1.

D'Agostini G. 1995. A multidimensional unfolding method based on Bayes' theorem. *Nucl. Instrum. Meth. A*, **362**(2-3), 487–498.

De Lellis G. et al. 2007. Emulsion Cloud Chamber technique to measure the fragmentation of a high-energy carbon beam. *J. Instrum.*, **2**(06), P06004.

Dudouet J. et al. 2013. Double-differential fragmentation cross-sections measurements of 95 MeV/u ^{12}C beams on thin targets for hadrontherapy. *Phys. Rev. C*, **88**(2), 024606.

Durante M. & Cucinotta F. 2011. Physical basis of radiation protection in space travel. *Rev. Mod. Phys.*, **83**(4), 1245.

Durante M. & Paganetti H. 2016. Nuclear physics in particle therapy: a review. *Rep. Prog. Phys.*, **79**(9), 096702.

Enghardt W. et al. 2004. Charged hadron tumour therapy monitoring by means of PET. *Nucl. Instrum. Meth. A*, **525**(1-2), 284–288.

Fassò A. et al. 2007. New developments in FLUKA modelling of hadronic and EM interactions. *Pages 32–43 of: KEK Proceedings*, vol. 97. National Laboratory for High Energy Physics.

Ferrari A. et al. 1992. An improved multiple scattering model for charged particle transport. *Nucl. Instrum. Meth. B*, **71**(4), 412–426.

Ferrari A. et al. 2005. *FLUKA: a multi-particle transport code*. CERN-2005-10, INFN TC_05/11, SLAC-R-773.

Friedland W. et al. 1999. Simulation of DNA fragment distributions after irradiation with photons. *Radiat. Environ. Bioph.*, **38**(1), 39–47.

Furusawa Y. et al. 2000. Inactivation of aerobic and hypoxic cells from three different cell

lines by accelerated ^{3}He-, ^{12}C- and ^{20}Ne-ion beams. *Radiat. Res.*, **154**(5), 485–496.

Grassberger C. & Paganetti H. 2011. Elevated LET components in clinical proton beams. *Phys. Med. Biol.*, **56**(20), 6677.

Griffin J. J. 1966. Statistical model of intermediate structure. *Phys. Rev. Lett.*, **17**(9), 478.

Gunzert-Marx K. et al. 2008. Secondary beam fragments produced by 200 MeV u^{-1} ^{12}C ions in water and their dose contributions in carbon ion radiotherapy. *New J. Phys.*, **10**(7), 075003.

Hall E. J. & Hei T. K. 2003. Genomic instability and bystander effects induced by high-LET radiation. *Oncogene*, **22**(45), 7034.

Hall E. J. et al. 2006. *Radiobiology for the Radiologist*. Vol. 6. Lippincott Williams & Wilkins Philadelphia.

Hassler D. M. et al. 2013. Mars' surface radiation environment measured with the Mars Science Laboratory's Curiosity rover. *Science*, 1244797.

Highland V. L. 1975. Some practical remarks on multiple scattering. *Nucl. Instrum. Meth.*, **129**(2), 497–499.

ICRU. 2000. *Nuclear Data for Neutron and Proton Radiotherapy and for Radiation Protection (Report 63)*.

ICRU. 2007. *Prescribing, Recording, and Reporting Proton-Beam Therapy (Report 78)*.

Iljinov A. et al. 1991. Production of radionuclides at intermediate energies. *Landolt-Börnstein, New Series*, **Subvol. I/13**.

Indelicato D. et al. 2016. Consensus Report From the Stockholm Pediatric Proton Therapy Conference. *Int. J. Radiat. Oncol.*, **96**(2), 387–392.

Jäkel O. 2008. The relative biological effectiveness of proton and ion beams. *Z. Med. Phys.*, **18**(4), 276 – 285.

Kanai T. et al. 1999. Biophysical characteristics of HIMAC clinical irradiation system for heavy-ion radiation therapy. *Int. J. Radiat. Oncol.*, **44**(1), 201–210.

Karger C. P. 2006. Biological models in treatment planning. *Pages 221–235 of: New Technologies in Radiation Oncology*. Springer.

Kelic A. et al. 2009. ABLA07-towards a complete description of the decay channels of a nuclear system from spontaneous fission to multifragmentation. *arXiv preprint: 0906.4193*.

Koning A. J. et al. 2007. TALYS-1.0. *Pages 211–214 of: International Conference on Nuclear Data for Science and Technology*. EDP Sciences.

Kraan A. C. 2015. Range verification methods in particle therapy: underlying physics and Monte Carlo modeling. *Fron. Oncol.*, **5**, 150.

Kraft G. 2000. Tumor therapy with heavy charged particles. *Prog. Part. Nucl. Phys.*, **45**, S473–S544.

Krimmer J. et al. 2015. Collimated prompt gamma TOF measurements with multi-slit

multi-detector configurations. *J. Instrum.*, **10**(01), P01011.

Landau L. D. 1944. On the energy loss of fast particles by ionization. *J. Phys.*, **8**, 201–205.

Leo W. R. 2012. *Techniques for nuclear and particle physics experiments: a how-to approach*. Springer Science & Business Media.

Lomax M. et al. 2013. Biological consequences of radiation-induced DNA damage: relevance to radiotherapy. *Clinical oncology*, **25**(10), 578–585.

Lühr A. et al. 2012. The impact of modeling nuclear fragmentation on delivered dose and radiobiology in ion therapy. *Phys. Med. Biol.*, **57**(16), 5169.

Mairani A. 2007. *PhD thesis*.

Marafini M. et al. 2017. Secondary radiation measurements for particle therapy applications: nuclear fragmentation produced by ^{4}He ion beams in a PMMA target. *Phys. Med. Biol.*, **62**(4), 1291.

Marsaglia G. & Tsang W. W. 2004. The 64-bit universal RNG. *Stat. Probabil. Lett.*, **66**(2), 183–187.

Mattei I. et al. 2017. Secondary radiation measurements for particle therapy applications: prompt photons produced by ^{4}He, ^{12}C and ^{16}O ion beams in a PMMA target. *Phys. Med. Biol.*, **62**(4), 1438.

Molière G. 1948. Theorie der streuung schneller geladener teilchen ii mehrfach-und vielfachstreuung. *Z. Naturforsch. A*, **3**(2), 78–97.

Morrocchi M. et al. 2018. Development and characterization of a ΔE-TOF detector prototype for the FOOT experiment. *submitted to Phys. Med. Biol.*

Nikjoo H. et al. 1999. Quantitative modelling of DNA damage using Monte Carlo track structure method. *Radiat. Environ. Bioph.*, **38**(1), 31–38.

Paganetti H. 2014. Relative biological effectiveness (RBE) values for proton beam therapy. Variations as a function of biological endpoint, dose, and linear energy transfer. *Phys. Med. Biol.*, **59**(22), R419.

Parodi K. 2004. *PhD thesis*.

Piersanti L. et al. 2014. Measurement of charged particle yields from PMMA irradiated by a 220 MeV/u ^{12}C beam. *Phys. Med. Biol.*, **59**(7), 1857.

Pleskac R. et al. 2012. The FIRST experiment at GSI. *Nucl. Instrum. Meth. A*, **678**, 130–138.

Rauch J. & Schlüter T. 2015. GENFIT – a Generic Track-Fitting Toolkit. *Page 012042 of: J. Phys. Conf. Ser.*, vol. 608.

Roesler S. et al. 2001. The Monte Carlo event generator DPMJET-III. *Pages 1033–1038 of: Advanced Monte Carlo for Radiation Physics, Particle Transport Simulation and Applications*. Springer.

Rovituso M. et al. 2017. Fragmentation of 120 and 200 MeV/u^{-1} ^{4}He ions in water and PMMA targets. *Phys. Med. Biol.*, **62**(4), 1310.

Schardt D. et al. 2010. Heavy-ion tumor therapy: physical and radiobiological benefits.

Rev. Mod. Phys., **82**(1), 383.

Scholz M. & Kraft G. 1996. Track structure and the calculation of biological effects of heavy charged particles. *Adv. Space Res.*, **18**(1), 5 – 14.

Serber R. 1947. Nuclear reactions at high energies. *Phys. Rev.*, **72**(11), 1114.

Simos N. et al. 2018. Demagnetization of $Nd_2Fe_{14}B$, $Pr_2Fe_{14}B$, and Sm_2Co_{17} Permanent Magnets in Spallation Irradiation Fields. *IEEE T. Magn.*, **54**(BNL-205752-2018-JAAM).

Sorge H. 1995. Flavor production in Pb (160A GeV) on Pb collisions: Effect of color ropes and hadronic rescattering. *Phys. Rev. C*, **52**(6), 3291.

Sorge H. et al. 1989. Poincaré invariant hamiltonian dynamics: modelling multi-hadronic interactions in a phase space approach. *Ann. Phys.-New York*, **192**(2), 266–306.

Tang J. et al. 1997. Comparison of radiobiological effective depths in 65-MeV modulated proton beams. *Brit. J. Cancer*, **76**(2), 220.

Tommasino F. & Durante M. 2015. Proton radiobiology. *Cancers*, **7**(1), 353–381.

Toppi M. et al. 2015. Measurements of 12 C ion fragmentation on thin carbon target from the FIRST collaboration at GSI. *Page 012035 of: Journal of Physics: Conference Series*, vol. 590. IOP Publishing.

Toppi M. et al. 2016. Measurement of fragmentation cross sections of ^{12}C ions on a thin gold target with the FIRST apparatus. *Phys. Rev. C*, **93**(6), 064601.

Torre L. A. et al. 2015. Global cancer statistics, 2012. *CA-Cancer J. Clin.*, **65**(2), 87–108.

Traini G. et al. 2017. Design of a new tracking device for on-line beam range monitor in carbon therapy. *Phys. Medica*, **34**, 18–27.

Vavilov P. V. 1957. Ionization losses of high-energy heavy particles. *Sov. Phys. JETP*, **5**, 749–751.

Vlachoudis V. et al. 2009. FLAIR: a powerful but user friendly graphical interface for FLUKA. *In: International Conference on Mathematics, Computational Methods & Reactor Physics*.

List of Publications

Refereed publications

M. Morrocchi, E. Ciarrocchi, A. Alexandrov, B. Alpat, G. Ambrosi, S. Argirò, G. Battistoni, N. Belcari, M. Bertazzoni, S. Biondi, G. Bruni, N. Camarlinghi, P. Carra, P. Cerello, A. Clozza, S. Colombi, G. De Lellis, A. Del Guerra, M. De Simoni, A. Di Crescenzo, M. Donetti, Y. Dong, M. Durante Marcok, A. Embriaco, M. Emde, R. Faccini, V. Ferrero, F. Ferroni, E. Fiandrini, C. Finck, E. Fiorina, M. Fischetti, M. Francesconi, M. Franchini, L. Galli, M. Garbini, V. Gentile, G. Giraudo, R. Hetzel, S. Hild, M. Ionica, K. Kanxheri, A.C. Kraan Aafke, V. Lante A. Lauria, C. La Tessa, E. Lopez Torres, M. Marafini, I. Mattei, A. Mengarelli, R. Mirabelli, M.C. Montesi, M.C. Morone, S. Muraro, L. Narici, A. Pastore, N. Pastrone, V. Patera, F. Pennazio, P. Placidi, M. Pullia, L. Ramello, R. Ridolfi, V. Rosso, M. Rovituso, C. Sanelli, A. Sarti, G. Sartorelli, O. Sato, S. Savazzi, A. Schiavi, C. Schuy, E. Scifoni, A. Sciubba, M. Selvi, L. Servoli, G. Silvestre, M. Sitta, R. Spighi, E. Spiriti, G. Sportelli, A. Stahl, S. Tomassini, F. Tommasino, G. Traini, T. Valeri, S.M. Valle, M. Vanstalle, M. Villa, U. Weber, A. Zoccoli and M.G. Bisogni Maria 2018. "Development and characterization of a ΔE-TOF detector prototype for the FOOT experiment". Accepted in *Nuclear Instruments and Methods in Physics Research Section A*.

I. Mattei, G. Battistoni, F. Collini, E. De Lucia, M. Durante, S. Fiore, C. La Tessa, C. Mancini-Terracciano, M. Marafini, R. Mirabelli, S. Muraro, R. Paramatti, L. Piersanti, A. Rucinski, A. Russomando, A. Sarti, C. Schuy, A. Sciubba, E. Solfaroli Camillocci, M. Toppi, G. Traini, S.M. Valle, M. Vanstalle and V. Patera 2017. "Addendum: Measurement of charged particle yields from PMMA irradiated by a 220 MeV/u ^{12}C beam". *Physics in Medicine & Biology*, **62**(21), 8483. https://doi.org/10.1088/1361-6560/aa8b35

Publications under review

A. Rucinski, G. Traini, A. Baratto Roldan, G. Battistoni, M. De Simoni, Y. Dong, M. Fischetti, P.M Frallicciardi, E. Gioscio, C. Mancini-Terracciano, M. Marafini, I. Mattei, R. Mirabelli, S. Muraro, A. Sarti, A. Schiavi A. Sciubba, E. Solfaroli Camillocci, S.M. Valle

and V. Patera 2018. "Secondary radiation measurements for particle therapy applications: Charged secondaries produced by ^{16}O ion beams in a PMMA target at large angles". Submitted to *Physics in Medicine & Biology*.

V. Giacometti, G. Battistoni, M. De Simoni, Y. Dong, M. Fischetti, E. Gioscio, I. Mattei, R. Mirabelli, V. Patera, A. Sarti, A. Sciubba, G. Traini, S. M. Valle and M. Marafini. "Characterisation of the MONDO detector response to neutrons by means of a FLUKA Monte Carlo simulation". Submitted to *Radiation Measurements*.

Publications in preparation

FOOT collaboration, General paper about the FOOT experiment.

Publications in conference proceedings

G. Traini, I. Mattei, G. Battistoni, M. De Simoni, Y. Dong, A. Embriaco, M. Fischetti, E. Gioscio, C. Mancini-Terracciano, M. Marafini, R. Mirabelli, S. Muraro, A. Sarti, A. Sciubba, E. Solfaroli Camillocci, M. Toppi, G. Traini, S.M. Valle and V. Patera 2018. "Charged particles and neutron trackers: applications to Particle Therapy". Accepted in *NIMA Proceedings*.

I. Mattei, G. Battistoni, M. De Simoni, Y. Dong, A. Embriaco, M. Fischetti, G. Giacometti, E. Gioscio, M. Magi, C. Mancini-Terracciano, M. Marafini, R. Mirabelli, S. Muraro, A. Sarti, A. Sciubba, E. Solfaroli Camillocci, M. Toppi, G. Traini, S.M. Valle and V. Patera 2018. "Scintillating fiber devices for Particle Therapy applications". *IEEE Transactions on Nuclear Science*, **65**(8), 2054-2060. Proceeding for the 14th Int. Conference on Scintillatig Materials and their Applications. https://10.1109/TNS.2018.2843179

G. Battistoni, A. Alexandrov, S. Argiro, N. Belcari, S. Biondi, M.G. Bisogni, G. Bruni, S. Brambilla, N. Camarlinghi, P. Cerello, E. Ciarrocchi, A. Clozza, G. De Lellis, A. Di Crescenzo, M. Durante, R. Faccini, V. Ferrero, F. Ferroni, C. Finck, M. Francesconi, M. Franchini, L. Galli, M. Garbini, G. Giraudo, E. Iarocci, K. Kanxheri, A. Lauria, C. La Tessa, M. Marafini, I. Mattei, R. Mirabelli, M.C. Montesi, M.C. Morone, M. Morrocchi, S. Muraro, L. Narici, R. Paramatti, A. Pastore, N. Pastrone, V. Patera, C. Peroni, M. Pullia, L. Ramello, V. Rosso, M. Rovituso, C. Sanelli, A. Sarti, G. Sartorelli, O. Sato, A. Schiavi, C. Schuy, E. Scifoni, A. Sciubba, M. Selvi, L. Servoli, M. Sitta, R. Spighi, E. Spiriti, G. Sportelli, M. Testa, V. Tioukov, F. Tommasino, G. Traini, S.M. Valle, M. Vanstalle, M. Villa, U. Weber and A. Zoccoli 2017. "The FOOT (Fragmentation Of Target) Experiment". Proceeding for the 55th International Winter Meeting on Nuclear Physics, Bormio, Italy. https://doi.org/10.22323/1.302.0023

S.M. Valle, G. Battistoni, V. Patera, D. Pinci, A. Sarti, A. Sciubba, E. Spiriti and M. Marafini 2016. "The MONDO project: A secondary neutron tracker detector for particle therapy". *Nuclear Instruments and Methods in Physics Research Section A*, **845**, 556-559. https:

//doi.org/10.1016/j.nima.2016.05.001

V. Patera, S. Argiro, D. Barbosa, G. Battistoni, N. Belcari, G. Bruni, M.G. Bisogni, S. Brambilla, N. Camarlinghi, P. Cerello, E. Ciarrocchi, A. Clozza, G. De Lellis, A. Di Crescenzo, M. Durante, R. Faccini, V. Ferrero, F. Ferroni, M. Fioralelli, M. Franchini, M. Garbini, G. Giraudo, S. Hild, A. Iacomino, J. Lotti, C. La Tessa, A. Lauria, I. Mattei, M. Marafini, M. Morrocchi, S. Muraro, L. Narici, R. Paramatti, N. Pastrone, C. Peroni, L. Ramello, V. Rosso, M. Rovituso, C. Sanelli, M. Salvatore, A. Sarti, G. Sartorelli, O. Sato, A. Schiavi, E. Scifoni, A. Sciubba, M. Selvi, L. Servoli, M. Sitta, R. Spighi, P. Spinnato, E. Spiriti, G. Sportelli, M. Testa, V. Tioukov, F. Tommasino, G. Traini, A. Zoccoli, S.M. Valle and M.S. Villa 2016. "The Foot (Fragmentation Of Target) Experiment". PoS(INPC2016)128. Proceeding for the 26th International Nuclear Physics Conference, Adelaide, Australia. https://doi.org/10.22323/1.281.0128

Technical reports

FOOT collaboration, FOOT CDR (Conceptual Design Report). https://doi.org/10.13140/RG.2.2.28904.78080

Acknowledgments

Vorrei ringraziare tutte le persone che, chi più, chi meno, in qualche modo mi hanno lasciato qualcosa in questi tre anni di dottorato e che sono sparse per mezza Italia. Ringraziarvi tutti sarà come fare un viaggio, anzi, come prendere il solito treno Italo da Milano Rogoredo a Roma Termini.

Quindi, andando in ordine di fermata, comincio ovviamente da Milano. Per prima cosa, ringrazio il Professor Giuseppe Battistoni (*"Aridaje co' sto professore"*), il mio supervisor. I motivi per cui ringraziarlo sono molti, e lui sicuramente li sa tutti, quindi ne cito uno solo, che è la prima cosa che ho imparato su di lui quando ancora non lo conoscevo: lui risponde, sempre, in tempo zero. Mail, messaggi, telefonate, in qualunque modo tu chieda il suo aiuto lui c'è. A vedere il numero di impegni da cui è sommerso, questa cosa ha del miracoloso. La prima volta che gli ho scritto una mail per avere informazioni sul dottorato a Milano, ero una neolaureata pavese che ha pigiato con ansia il tasto invia, temendo che non avrebbe mai ricevuto una risposta da quel professore importante e impegnato che non sapeva nemmeno chi fossi. Ebbene, la sua risposta è arrivata in 3 minuti netti. Giuro.

Poi voglio ringraziare loro, i miei compagni d'arme. Ilaria, la mia piccola e tostissima boss, che mi ha sempre spronata e che crede in me più di quanto faccia io. Alessia, che come me ha abbandonato le sicure sponde pavesi del Ticino per avventurarsi nella giungla urbana del capoluogo lombardo. Yun, che non si arrabbia mai e ha sempre una scorta di dolciumi sufficiente alla sopravvivenza in caso di catastrofe nucleare. E Silvia, che ci manca tanto in ufficio e che sono sicura non si offenderà se la metto tra i milanesi.

Dopo un'oretta di viaggio il treno arriva finalmente a Bologna. Qui voglio ringraziare in particolare Roberto, che mi ha sempre accolta come se fossi una delle sue tesiste. Ha condiviso con me il suo lavoro, mi ha aiutata molto e si è pure letto tutta la mia tesi. Grazie! Ma oltre a lui ci sono anche i ragazzi: Matteo, che mi ha sempre dato una mano con pazienza, Alberto, a cui spero di non aver fatto odiare FLUKA (non troppo almeno), e Silvia, che ha dovuto sopportare me e Alessia per tre giorni.

L'ultima fermata infine è Roma. Qui ringrazio Vincenzo, che mi ha accolta in FOOT con gentilezza ed entusiasmo. Grazie ovviamente a Michela, che è fantastica e per prima mi ha lanciata nel mondo delle conferenze, e ad Alessio, che mi ha insegnato moltissimo

ed è una fonte inesauribile di risposte e soluzioni. Ma ci sono anche gli altri, in particolare i ragazzi con cui ho condiviso alcune trasferte: Giacomo, con cui ho passato una settimana a Strasburgo tra disavventure aeree e ferroviarie al limite dell'incredibile, Marta, insieme a cui per una settimana ho cercato di far funzionare un maledetto kit CAEN parlando degli ultimi preparativi per i nostri matrimoni, e Riccardo, che ho trascinato per 5 giorni in giro per Praga.

A Bari Italo non arriva ma vorrei ringraziare anche Alessandra, che ho conosciuto per le simulazioni delle emulsioni e che sento sempre con piacere.

Questa sembra la fine del viaggio, ma non lo è, perché dopo ogni viaggio si ritorna a casa, e lì le persone da ringraziare sono tante, e voglio ringraziarle qui in un ordine un po' random.

Grazie ad Alice, che vedo poco ma c'è sempre, e ormai ha spiccato il volo (letteralmente) per atterrare a Bruxelles.

Grazie a Debora e Katia, le due splendide donne che da 5 anni mi fanno dormire sonni tranquilli perchè so che il mio Ninù è nelle mani migliori.

Grazie a *La Compagnia del Vino*: la Fede, la mia Fede, che mi dice tutto, dai suoi segreti alle sgridate che mi merito, e il Paolo, che prima o poi si rifiuterà di uscire con noi visto che ogni volta deve sorbirsi punzecchiamenti e domande scomode.

Grazie a *Le Donne & Gli Uomini Duri*. Con loro ho condiviso il capodanno più pazzo e memorabile della mia vita al Camping Cervino: un mix esplosivo e inaspettato di risate, litigate, cadute rovinose, vagabondaggi notturni, sventati tentativi di piromania e canzoni dei Pooh uscite a caso giocando a Taboo. *Gli Uomini* però non me ne vorranno se ringrazio in particolare *Le Mie Donne*: siamo così diverse (un'educatrice, un'assistente di volo, una biotecnologa e un fisico), ma siamo così uguali (quattro *equitanti inside*) da risultare quattro amiche ben assortite.

Grazie alla famiglia Rigamonti. Quando si dice "amici di famiglia" io penso a loro.

Grazie alla famiglia Semenza-Savini, che è diventata un pezzo della mia famiglia. In particolare grazie a Paolo e Chiara, il fratello e la sorella che non ho mai avuto, e a Lella, la cui presenza e assenza ci accompagnano ogni giorno.

Grazie a mio zio Carlo, Mariangela e Chiara, che vedo poco ma sento sempre vicini.

Grazie al nonno Angelo e la nonna Nella, che sono sempre orgogliosi di me.

Grazie al Giacomino, interista fino al midollo, mazziere capo del bar in piazza (dai, non fare il musone e riprenditi il tuo incarico!) e nonno dal *barbarì* tremante.

Grazie ai miei bestiolini, Cleis, Nemeo e Nyx. Al mio piccolo Ingo, che ha reso casa Savini-Valle un posto più caldo (forse anche grazie al pelo che sparge in abbondanza). Al mio Chenel, che, come ho già scritto altrove, era il mio sogno e lo sarà sempre.

Grazie mamma e papà. Per loro le parole non bastano: quello che sono e che ho lo devo a loro. Grazie!

E infine grazie a te Gio. Ti lascio sempre per ultimo, ma solo perchè sai che in realtà sei il primo. Grazie di tutte le piccole cose che tu sai, grazie di essere la mia casa, grazie di essere sempre all'altro capo della mia corda per farmi sicura in tutti i giorni in cui mi sembra di dover scalare le montagne. Mi dici sempre di non aver paura, che il panorama da lassù è bellissimo. E sì, con te da lassù il panorama è ogni volta da mozzare il fiato.